APPLICATION OF REMOTE SENSING AND GOOGLE EARTH ENGINE FOR AGRICULTURAL MAPPING IN SOUTH ASIA

by

Zhiqi Yu
A Dissertation
Submitted to the
Graduate Faculty
of
George Mason University
in Partial Fulfillment of
The Requirements for the Degree
of
Doctor of Philosophy
Earth Systems and Geoinformation Sciences

Committee:

_______________________ Dr. Liping Di, Committee Chair

_______________________ Dr. Ruixin Yang, Committee Member

_______ John J. Qu _______ Dr. John Qu, Committee Member

_______________________ Dr. Daniel Tong, Committee Member

_______ Dieter Pfoser _______ Dr. Dieter Pfoser, Department Chairperson

_______ Donna M. Fox _______ Dr. Donna M. Fox, Associate Dean, Office of Student Affairs & Special Programs,

_______________________ Dr. Fernando R. Miralles-Wilhelm, Dean, College of Science

Date: _________4/21/2022_____________ Spring Semester 2022
George Mason University
Fairfax, VA

Application of Remote Sensing and Google Earth Engine for Agricultural Mapping in South Asia

A Dissertation submitted in partial fulfillment of the requirements for the degree of Doctor of Philosophy at George Mason University

by

Zhiqi Yu
Master of Arts
The Ohio State University, 2017
Bachelor of Engineering
Wuhan University, 2015

Director: Liping Di, Professor
Department of Geography and Geoinformation Science

Spring Semester 2022
George Mason University
Fairfax, VA

DEDICATION

This dissertation is dedicated to my parents, Yongkuan Yu and Guihe Wang, and my loving fiancé Dr. Yuechun Wang.

ACKNOWLEDGEMENTS

I would like to express my sincere gratitude to my Ph.D. advisor, Prof. Liping Di, for his guidance on my academic endeavor. I would not be able to stand where I am without the continuous support and his experience and knowledge in this field. I would like to also thank my Ph.D. committee members, Prof. John Qu, Prof. Ruixin Yang, and Prof. Daniel Tong. Their valuable suggestions and comments helped me think deeper into my dissertation topic and think broader about science in general.

Throughout my Ph.D., I had the privilege to work on two NASA funded projects, namely the NASA Land Use and Land Cover Project (Grant # NNX17AH95G, PI: Prof. Liping Di) and the NASA SERVIR project (Grant # 80NSSC20K0161, PI: Prof. Liping Di) under the guidance of my Ph.D. advisor. My research works in these projects helped shape the foundation of this dissertations.

Next, I would like to thank my colleagues at the Center for Spatial Information Science and Systems (CSISS), namely Dr. Md. Shahinoor Rahman, Dr. Junmei Tang, Dr. Chen Zhang, Dr. Li Lin, Dr. Ziheng Sun, Haoteng Zhao, and Alamin Molla for all the assistance and support in my research and projects.

Lastly, I would like to thank all the professors at Geography and Geoinformation Science department and all my fellow Ph.D. students/friends for accompanying me through my Ph.D. journey.

TABLE OF CONTENTS

LIST OF TABLES

LIST OF FIGURES

LIST OF EQUATIONS

LIST OF ABBREVIATIONS

Application Programming Interface	API
Automated Water Extraction Index	AWEI
Bangladesh Bureau of Statistics	BBS
Classification and Regression Tree	CART
Cropland Data Layer	CDL
Decision Tree	DT
End-of-season	EOS
Enhanced Vegetation Index	EVI
Food and Agriculture Organization	FAO
Google Earth Engine	GEE
International Centre for Integrated Mountain Development	ICIMOD
Land Surface Water Index	LSWI
Land use land cover	LULC
Logistic Regression	LR
Machine Learning	ML
Military Grid Reference System	MGRS
Moderate Resolution Imaging Spectroradiometer	MODIS
Modified Normalized Difference Water Index	MNDWI
Near-infrared	NIR
Neural Network	NN
Normalized Difference Vegetation Index	NDVI
Normalized Difference Water Index	NDWI
Object-based features	OBF
Radar Vegetation Index	RVI
Random Forest	RF
Shortwave-infrared	SWIR
Single-page web application	SPA
South Asia	SA
Start-of-season	SOS
Support Vector Machine	SVM
Sustainable Development Goals	SDG
Synthetic Aperture Radar	SAR
Vegetation Index	VI
Water Index	WI

ABSTRACT

APPLICATION OF REMOTE SENSING AND GOOGLE EARTH ENGINE FOR AGRICULTURAL MAPPING IN SOUTH ASIA

Zhiqi Yu, Ph.D.

George Mason University, 2022

Dissertation Director: Dr. Liping Di

Agricultural land use is one of the dominant land use types in South Asia (SA). A majority of SA population depends on agriculture for their livelihood. The agricultural activities and food production in SA are tightly related to the poverty level in many SA countries and has broader impact on global food security, climate change, economics, etc. To feed the growing population in SA with most of the land suitable for agriculture already cultivated, crop intensification and transitions from traditional agriculture to non-crop, cash crops, and fishery are expected. These land use and land cover changes have profound impact on the regional and global food security and economics. Thus, timely producing agricultural land use data products with remote sensing technique are very important to achieve sustainable agriculture and monitoring such agriculture land use changes. However, the application of remote sensing in SA faces many challenges, e.g., persistent high cloud covers during monsoon seasons, very limited availability of ground

truth samples, and excessively small and irregularly shaped agriculture fields, etc. Thus, this dissertation study aims to design algorithms and tools to help monitoring agriculture land use changes in SA using remote sensing images and provide insight on addressing such challenges. As Google Earth Engine (GEE) is becoming increasingly popular in the remote sensing community, this dissertation also explores utilizing GEE's potential for operational agriculture mapping and designing complex data processing workflows. To achieve the overall goal, this dissertation presents research for three objectives. Specifically, this dissertation first presents a novel workflow for inland fishpond mapping using spectral and spatial information derived from remote sensing images. This workflow was implemented on GEE and was tested in a case study in Singra Upazila in Bangladesh. The results showed that the method successfully detects fishponds with an F1 score of 0.64. Next, a GEE-based workflow that combines MODIS Terra and Aqua data and uses Harmonic Regression to reconstruct time-series Normalized Difference Vegetation Index (NDVI) for crop intensity mapping was presented. The method was used for crop intensity mapping in Bangladesh 2010 and showed a national average crop intensity of 1.66. Lastly, a GEE-based web application named RiceMapEngine was developed to provide a one-stop experience of rice mapping to higher-level officials and decision makers. This application was demonstrated in rice mapping for Chitwan district in Nepal. The result showed that this application can successfully help produce early-season and post-season rice maps using GEE with very easy-to-use interfaces.

1. INTRODUCTION

1.1. Research Background

The United Nation introduced 17 sustainable development goals (SDGs) in September 2015 to guide the work of the organization and the entire globe in the following 15 years (United Nations, 2018). These SDGs cover a wide range of topics including poverty, food security, health, education, climate change, economy, social inequality, etc. Agriculture, which includes farming of both plants and animals when defined broadly, plays a major role in the SDGs. Over the course of human history, agricultural activity has significantly modified the land surface, and agriculture lands takes up nearly 40% of the global land area nowadays (Foley et al., 2005). The ever-growing population on the planet poses great challenges to the food security (Weiss et al., 2020). According to a report in 2020 by Food and Agriculture Organization (FAO), there are about 720 to 811 million people that are exposed to severe food insecurity in 2020, and the COVID-19 pandemic started from 2019 may have added approximately 100 million people to the number (FAO et al., 2021). An estimate shows that the world's agricultural production must increase by 70 %–110 % from 2010 to 2050 to meet the projected demands caused by increasing populations and changing diets (FAO, 2009). As a result, the needs for increased agriculture yield, more arable cropland, cropland intensification, and food diversification are keys to solve food insecurity. In addition to food security, agricultural activities are also intertwined with the ecological change and climate change. Agricultural activities produce various greenhouse gases from fertilizers, animal ruminants, and paddy rice cultivation, which contribute to the global warming (OECD, 2016). Agriculture crop intensification may cause soil degradation, and the overuse of fertilizers may also introduce water pollution and air pollution (Ni et al., 2021a; J. Yu & Wu, 2018). In fact, the growing need of food with limited croplands often contradicts with the need for environment protection and sustainability (J. Yu & Wu, 2018). Thus, understanding agriculture in terms of its spatial distribution and yield, and its complex relationships with environment, energy usage, air quality and climate change is the key to successfully reach SDGs.

The SA region as shown in Figure 1 consists of Afghanistan, India, Pakistan, Bangladesh, Sri Lanka, Nepal, Bhutan and Maldives. The entire region covers about 5.2 million square kilometers (km^2) and is home to about 1.891 billion people, which accounts for 1⁄4 of the whole population on the planet. In addition to being one of the most populous regions in the world, the SA region is also one of the poorest regions in the world. According to the World Bank’s 2011 report, about 24.6% of the SA population lives under the international poverty line, and SA accounts for 29% of total population living in extreme poverty worldwide (World Bank, 2018). A majority of the population are engaged in agriculture activities. Moreover, a large portion of the terrain are inhospitable such that most of the population lives on less than half of the entire region, which significantly intensified the population density and the consumption of natural resources. There are 6 main climate systems in the SA region. Areas that are close to the ocean are mostly in the tropical climate zone. The northern India, lowland area of Nepal, and northern part of Bangladesh are in humid subtropical zone. The inland area that includes northwestern India and Pakistan are in semiarid and desert zones. The east of SA region, which includes Bangladesh and around the northeastern, eastern, and southern fringe of India, are under the influence of seasonal monsoon. The high humidity brought by the monsoon rains and the hot temperature during summer provide a great condition for rice. As shown in Figure 1, the Ganges River Basin is home to soil with ample moisture. With large areas of alluvial soils and a high proportion of the land under intensive rice cultivation, these areas can provide food for a significantly large and dense population. The main farming system in this region, especially in the entire Bangladesh, West Bengal of India, and Terai belt region of Nepal, is rice farming. The rice growing seasons can range from one season in some lowland area to three seasons with the help of irrigations in the dry season (Biradar & Xiao, 2011; Gray et al., 2014). Due to the rapid urban expansion and population increase, the land availability per capita is decreasing, and thus a trend of farming intensification is expected. Moreover, as the profit of growing rice decreases, there is also a trend of farming diversification. For example, many farmers start to modify farmlands into fishponds as a replacement to cultivate fish for better profits (Hashem et al., 2014). The crop type and crop system changes in the last decade have huge impact on the overall health and economics of the SA region.

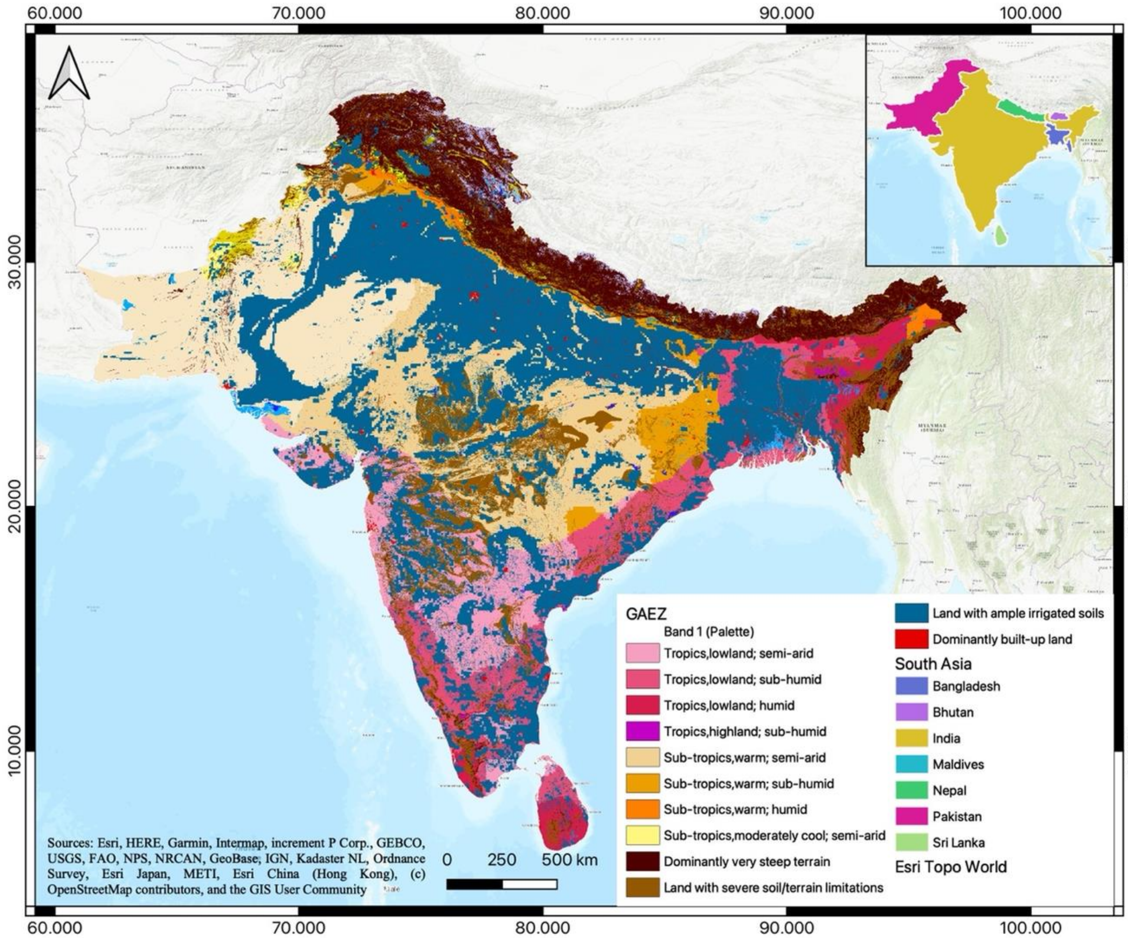

Figure 1. Agro-ecological zones of SA. Data source: Global Agro-Ecological Zones (GAEZ v4).

Remote sensing technology has been evolving in the recent decades such that the observations for the earth are made with higher spatial resolution and higher revisit frequency. It has become an essential tool to non-destructively provide recurrent observations from local to the global scale for surveying and monitoring purpose (Weiss et al., 2020). Remote sensing is especially suitable for agriculture monitoring. As crop grows, biomass increases, and the land cover and canopy structure and density changes rapidly. Remote sensing technology can be used to detect such changes using either optical sensors or radar sensors. Optical sensors usually provide multi-spectral information which can be used to derive indicators that are associated with biomass and vegetation health. Radar sensors on the other hand, provide information on the surface roughness and moisture content. The backscatter intensity and the cross-polarization can be used to characterize crop canopy structure changes and soil moisture changes, which are indirectly linked with biomass changes as crop grows. While passive optical remote sensing is extremely popular in studying vegetations due to their well-understood relationship to vegetation greenness, their usefulness decreases significantly when there is persistent cloud cover over an area. For regions like Bangladesh where monsoon season brings persistent cloud cover and high precipitation, passive optical remote sensing sensors suffer from severe missing data problem, which affects their ability to monitor vegetation health and predict crop yield during this period. Radar sensors typically work at frequency ranges that are not affected by the cloud and aerosols, which makes them desirable in applications that suffers from severe cloud cover problem. However, the relationship between the radar sensor recordings and vegetation physiology is less understood compared with multi-spectral sensor records. The distinct and yet complementary advantages and disadvantages of passive optical sensors and radar sensors make it beneficial to use them together for vegetation monitoring, especially for the SA region.

Traditionally, remote sensing data processing takes non-trivial work because of the sheer volume of data that need to be downloaded to and processed on local workstations. However, the advent of Google Earth Engine (GEE) (Gorelick et al., 2017), and the recent development from Microsoft, the Planetary Computer (PC) has made remote sensing data processing much easier thanks to the cloud computing infrastructure provided by Google and Microsoft. GEE provides researchers Application Programming Interfaces (APIs) to process and visualize remote sensing datasets by writing JavaScript code in the online code editor, which is shown in Figure 2. The online coding interface provides a highly integrated environment for data searching, API searching, asset management, coding area, print console and visualizations in the form of maps, charts, and text. The almost instant feedbacks that one can get from running data processing scripts using GEE help with spotting errors and mistakes early, and the immediate results can be quickly visualized and analyzed to progressively build complex processing pipelines. As a result, more and more research works are using GEE, and it has become so popular that it is shifting the paradigm for remote sensing research. In addition to help expediting remote sensing research, GEE and PC also offer powerful platforms to build web applications using their client APIs, which opens capabilities of building web applications that can conduct real-time remote sensing image processing. Such capabilities can bridge the gap between researchers or decision makers who don’t have programming or remote sensing expertise, and the critical information that remote sensing conveys.

With the climate change, rapid urbanization, industrialization, market globalization, and the fast growth of population ongoing in SA region, the agriculture in SA is experiencing a series of changes. These changes include cropping intensification, transition from agriculture to more-profitable fishery, potential shrinkage of agriculture lands, etc. It is important to utilize remote sensing technique and advanced cloud computing platforms to provide timely and accurate updates of these changes to stakeholders and decision makers. These data products will help enhance the understanding of the status-quo of the agricultural land use in SA region and help SA countries achieve 2030 UN SDGs eventually. In this dissertation, we mainly focus on the mapping tasks for monitoring transitions from agriculture to aquaculture, crop intensification, and monitoring paddy rice extents.

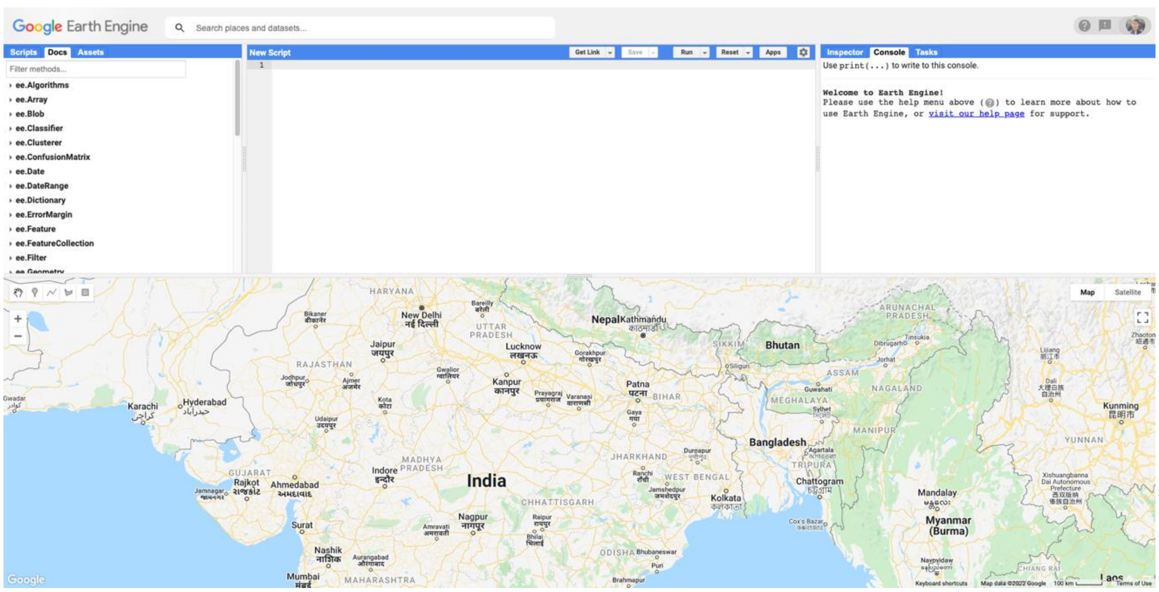

Figure 2. GEE online coding interface.

1.2. Problem Statements

The first mapping task is for monitoring changes from cropland to non-crop land use. Large conversion from cropland to non-crop, cash crop, and aquaculture use has been going on in South Asia countries. For example, high demands for fishes on the international market and high economic return of raising fish drive the significant conversion of agriculture to fishponds in Bangladesh, which make the food security and farmers' income more vulnerable to international market fluctuations. Therefore, knowing the extent and the spatial distribution of the transitions is essential to mitigate such risks. Although there are a few research works that investigated mapping coastal fishponds in Bangladesh and India, inland fishpond mapping is rarely explored. The inland fishponds are much smaller, and the shapes are more irregular comparing with coastal fishponds. Moreover, the inland water bodies like rivers, lakes, and floods pose challenges to the mapping of inland fishponds. Thus, it is worthwhile to investigate this topic using remote sensing technique and address unique challenges of mapping inland fishponds.

The second mapping task is for monitoring year-to-year crop intensity in SA region. With most of the lands that are suitable for rain-fed agriculture cultivated, crop intensification is expected to feed the growing population in SA region. However, crop intensification can introduce environmental issues such as soil degradation and water pollutions, which would impact the food security and climate change in the long term. Mapping cropping intensity using remote sensing data has long been investigated. Previous research has used various methods to reconstruct NDVI time-series and detect cropping seasons by phenology or using heuristics. While several data products were produced at global and continental scale, there are rarely studies that focus on SA, which is heavily affected by the persistent cloud cover during monsoon seasons. Thus, this dissertation will investigate crop intensity mapping using remote sensing data with significant missing data problem caused by cloud covers and compare the remote sensing-derived crop intensities with statistical results.

The last mapping task is for monitoring the change of paddy rice areas. As the most dominant crop type grown in many of the SA regions, rice is tightly coupled with the food security and the economics of the region. Knowing not only the area, but also the spatial distribution of paddy rice fields will help better predict food productions, which in turn will help decision makers better coordinate resources to ensure food security. Paddy rice mapping has been widely studied. Due to the unique transplanting phase, empirical methods can be used to detect paddy rice fields by identifying waters in the fields. Such methods often need ground truth data to calibrate and validate. However, ground truth samples for rice are hard to differentiate from other crop types on true color high resolution images because they all look similar, and the cloud may block views. Thus, it is important to have tools that can collect and validate paddy rice ground truth samples by examine the phenology of the sample. Although GEE has been used in many paddy rice mapping research works, there exists gaps between GEE's computing power with decision makers because GEE requires knowledge in programming. There are rarely tools that can translate the computing power of GEE through easy-to-use user interfaces. Thus, it is extremely worthwhile to investigate the potential of GEE for building easy-to-use rice mapping tools for ground truth sample validation and fast paddy rice area monitoring.

1.3. Research Objectives

With the problems and knowledge gaps being stated in the last section, this dissertation aims to achieve the following objectives.

Objective 1: Develop a novel GEE-based workflow to map inland fishponds.

These research questions should be answered: How can inland fishponds be differentiated with other water bodies like rivers, lakes, and floods? How does the size of fishponds affect the mapping results? What spatial resolution of remote sensing images is needed to map fishponds?

Objective 2: Investigate crop intensity mapping using remote sensing data and GEE.

These research questions should be answered: How does monsoon cloud cover affect the mapping result? How to deal with missing data problem caused by cloud cover? How does the mapping result compare with non-spatial statistical results?

Objective 3: Design a GEE-based software for ground truth sample validation and fast paddy rice mapping.

These research questions should be answered: How to efficiently use GEE in the software? How to validate ground truth samples using their phenology? How to use the software to produce paddy rice maps with or without ground truth samples? A case study needs to be conducted to showcase how to use the software and the accuracies of the rice maps need to be assessed.

1.4. Dissertation Outline

This dissertation contains 6 chapters, and they are arranged as follows:

Chapter 1 gives a brief introduction to the background of this dissertation, the knowledge gaps, and the research objectives.

Chapter 2 presents a detailed literature review on the physical principles of remote sensing for agriculture and the application of various ML models and GEE for agriculture mapping.

Chapter 3 presents the background, methodology, and findings of the research to achieve the first research objective. A novel workflow that maps inland fishponds using both spectral and spatial information derived from remote sensing data is presented. A case study in the Singra Upazila in Bangladesh is conducted to assess the performance of the proposed method.

Chapter 4 presents the research to achieve the second research objective. A GEE-based workflow was designed to produce crop intensity maps using MODIS surface reflectance data. The workflow uses Harmonic Regression to reconstruct NDVI curves and uses an empirical threshold to detect crop growing seasons. The method was used to produce the crop intensity map for Bangladesh in 2010, and the results were compared with statistical data from Bangladesh Bureau of Statistics (BBS).

Chapter 5 presents a GEE-based application to achieve the last research objective. The application was named RiceMapEngine, and it was designed for ground truth sample validation and paddy rice mapping. The background, software design, and main functionalities are discussed in this chapter. A case study of rice mapping operation in

Chitwan district of Nepal, 2021 is carried out and the accuracies of produced rice maps are discussed.

Chapter 6 summarizes the major results and findings for each of the research objectives, and the limitations of the proposed methods are discussed.

2. LITERATURE REVIEW

2.1. Physical principles of remote sensing applications in agriculture

Remote sensing is widely applied in agriculture applications, e.g., crop type mapping (HAO et al., 2020; Kenduiywo et al., 2018; Manjunath et al., 2015; Schultz et al., 2015; Sun et al., 2019; Villa et al., 2015; S. Wang et al., 2019; H. Zhang et al., 2020a, 2020b), crop pattern/system mapping (Gray et al., 2014; Guan et al., 2016; Jain et al., 2013; L. Li et al., 2014; L. Liu et al., 2020a; Manjunath et al., 2015). Multispectral images have a long history of being used to map vegetations. The physical principles of vegetations identification with multispectral images, and vegetation indices that were designed to identify vegetations are discussed in the next question below. SAR images are less popular in mapping vegetations because it lacks critical spectral information. Nevertheless, a recent trend of using SAR along with multispectral images for crop classification can be observed (LIU et al., 2019). SAR images are sensitive to the geometric, and dielectric characteristics of vegetations, and because SAR emits long wavelength signals, it often can penetrate the canopy of vegetations, and even carry information about soil when the vegetation cover is not high (LIU et al., 2019). The backscatter response of vegetation depends on the canopy structure, surface roughness, soil conditions, and sensor configurations (signal frequency, polarization, incident angle, etc.) (Moreira et al., 2013). Vegetations reflects radar signals in a volume scattering model. In the volume scattering model, the scatterers are the objects that are of the same order of the signal wavelength. The original polarized signal typically bounces between random scatterers in the volume and depolarizes. Thus, backscatters from volume scattering typically have high depolarization, and the response strength increases with the number of scatterers. Bare surfaces have weak depolarizing effect, and vegetation canopies are highly depolarizing. The cross-polarized signals (HV) increase with biomass. These characteristic lays foundation for many SAR-derived vegetation indices, e.g., radar vegetation index (RVI) (Mandal et al., 2020). Depending on different crop types, the backscatters show different patterns. For example, at C band, the backscatters in the wheat field are dominated by the ground scattering, attenuated by the vegetation layer. Thus, the backscatter increases as soil moisture increases (dielectric constant increase), and the backscatter decreases as biomass increases. The HH/VV ratio over the growing season corresponds well to the wheat biomass. Rice on the other hand, has a different mechanism. The backscatters in the rice field are dominated by the double bounces between vegetation and water. Thus, the HH and VV response increases as biomass increases. Similar to wheat, the HH/VV ratio corresponds well to the rice biomass.

Specific crop type classification often references the crop calendar information. As vegetation indices correspond well to vegetation biomass, and vegetation healthiness, time-series of vegetation indices are often used in the growing seasons of a specific crop growing season to see if the time-series match the biomass changes in the planting, growing, peak, and harvesting phases.

2.1.1. Vegetation Indices

Vegetation indices (VI) are indices derived using spectral bands to characterize vegetations based on their biophysical features. Specifically, healthy vegetation absorbs blue- and red-light during photosynthesis and produce chlorophyll which reflects near-infrared (NIR) waves which results in low reflectance in red band and high reflectance in the NIR band. Thus, VI often use the differences between reflectance of blue/red and NIR to enhance vegetations. A VI is effective if it is highly correlated with the biophysical parameters of vegetations and is less sensitive to noises coming from atmosphere and background soil.

Basic vegetation indices are indices designed without considering noises from soil and atmosphere. Jordan (1969) derived Ratio Vegetation Index (RVI) which is just a ratio between red band and NIR band. Later Rouse et al. (1973) derived Normalized Difference Vegetation Index (NDVI) that is based on reflectance difference between red band and NIR band, and the difference is normalized by the sum of the red and NIR band such that the NDVI value is ranged from -1 to 1. Despite being sensitive to background soil brightness and atmosphere, NDVI is the most widely used VI nowadays (Wójtowicz et al., 2016).

While basic VIs such as NDVI is concise and sufficiently effective, there are many efforts devoted to reducing impact of soil background and atmosphere on the vegetation identification. To reduce the atmosphere interference, Zhang et al. (1996) introduced IAVI. This index is based on the knowledge that red band is affected more by atmosphere than NIR band, and they used blue band to adjust red band values. Table 1 shows the equation of IAVI. Soil-Adjusted Vegetation Index (SAVI) proposed by Huete (1988) is an example of limiting impact of soil on remotely sensed vegetation data. Specifically, Huete (1988) identified that the impact from soil mainly come from the NIR signal that is scattered by vegetation canopy and then reflected by soil back to the sensor, and the impact is at peak when vegetation cover is around 50% when there is enough canopy to scatter and not too much to prevent soil reflected signals traveling back to the sensor. Table 1 shows the equations of SAVI. The constant L in the equation is inversely proportional to the vegetation cover, and according to Huete (1988), a fixed value 0.5 should already make SAVI a better VI than NDVI. Based on SAVI, Richardson and Wiegand (1977) introduced Modified Secondary SAVI (MSAVI2) which replaces L in the SAVI with a function. In a later work by Liu and Huete (1995), they found that the interaction between soil and atmosphere result in reducing one can increase the other. Thus, they introduced Enhanced Vegetation Index (EVI) to simultaneously correct soil and atmosphere effects. As the equation in Table 1 shows, the coefficients C_1 and C_2 corrects atmospheric effects to the red band using blue band, and the L corrects soil effect. Due to the overall simplicity and effectiveness, NDVI and EVI are included as standard data products in the MODIS datasets for global vegetation monitoring.

Aside from the above VIs that uses original spectral band to compute, another popular way to map vegetation is the Tasseled cap (TC) transformation (Kauth, 1976). Unlike VIs, TC transforms original image space into a new space where the first three components of the transformation are considered to represent brightness, greenness, and wetness. Thus, the second component is usually used to map vegetations.

Table 1. Vegetation indices, their equations, and references.

Name	Equation	Reference
RVI	$\frac{R}{NIR}$	(Jordan, 1969)
NDVI	$\frac{NIR - R}{NIR + R}$	(Rouse et al., 1973)
IAVI	$\frac{NIR - (R - \gamma(B - R))}{NIR + (R - \gamma(B - R))}$ where $\gamma = 0.65\sim1.12$	(R. H. Zhang et al., 1996)
SAVI	$\frac{(NIR - R)(1 + L)}{NIR + R + L}$ $where\ L = 0\sim1, typically\ 0.5$	(Huete, 1988)
MSAVI2	$0.5 * [(2NIR + 1) - \sqrt{(2NIR + 1)^2 - 8(NIR - R)}]$	(Richardson & Wiegand, 1977)
EVI	$2.5 * \frac{NIR - R}{NIR + C_1R - C_2B + L}$ $where\ C_1 = 6, C_2 = 7.5, L = 1$	(H. Q. Liu & Huete, 1995)

2.1.2. Water Indices

Water indices (WI) are used to detect vegetation water content and open water features. Open water feature reflects almost all energy in the visible spectrum, and it almost absorbs all signals within the NIR and short-infrared (SWIR) spectrum. Vegetation water content, however, is usually only characterized by the high absorption in the SWIR band. Because of this difference, WIs that are used to detect open water features typically uses the reflectance difference between optical spectrum and

NIR/SWIR spectrum, and WIs that are used to detect vegetation water content uses the reflectance between NIR and SWIR band (Ji et al., 2009; Ludwig et al., 2019; McFeeters, 1996; Y. Zhou et al., 2017). Gao (1996) derived a normalized difference water index ($NDWI_{Gao}$) to enhance vegetation liquid water from satellite observations. It uses NIR reflectance subtracted by SWIR reflectance because the more water in the vegetation, the more SWIR signal will be absorbed, and thus this index positively corresponds to vegetation water content. The same equation is also named as Normalized Difference Moisture Index (NDMI). For open water features, McFeeters (1996) also derived a normalized difference water index (NDWI) to delineate open water features from satellite observations. It uses the difference between the reflectance in green and NIR band because water reflects some energy in green spectrum and almost absorbs all energy in NIR spectrum, thus water features have positive NDWI values. Xu (2006) pointed that built-up area can be falsely identified with NDWI because built-up structures also reflect more green signal than NIR signal. Thus, he introduced the Modified Normalized Difference Water Index (MNDWI) that uses SWIR band instead of NIR band. As a combination of NDWI and MNDWI, Guo et al. (2017) introduced the weighted NDWI (WNDWI). Instead of using either NIR band (NDWI) or SWIR band (MNDWI), it uses a weighted average of the two bands such that noises like turbid water and vegetation in the shadow can be suppressed. Feyisa et al. (2014) derived Automated Water Extraction Index (AWEI) that aims to reduce noise coming from shadow. The AWEI consists of two formulas, $AWEI_{sh}$ for areas that are contaminated by shadows, and $AWEI_{nsh}$ for areas that are not (Z. Wang et al., 2018). Feyisa et al. (2014) reported that AWEI has much more stable optimal thresholds than MNDWI.

Table 2. Water Indices, their equations, and references.

Name	Equation	Reference
$NDWI_{Gao}$ / NDMI	$\frac{NIR - MIR}{NIR + MIR}$	(Gao, 1996)
NDWI	$\frac{G - NIR}{G + NIR}$	(McFeeters, 1996)
MNDWI	$\frac{G - MIR}{G + MIR}$	(Xu, 2006)
WNDWI	$\frac{G - \alpha NIR - (1-\alpha)SWIR1}{G + \alpha NIR + (1-\alpha)SWIR1}$ $where\ \alpha = 0 \sim 1$	(Guo et al., 2017)
AWEI	$AWEI_{nsh} = 4 * (G - SWIR1) - (0.25 * NIR + 2.75 * SWIR2)$ $AWEI_{sh} = R + 2.5 * G - 1.5 * (NIR + SWIR1) - 0.25 * SWIR2$	(Feyisa et al., 2014)

2.2. Machine learning applications in agricultural mapping

Machine learning (ML) is a subfield of Artificial Intelligence (AI) that aims to train computer systems to recognize patterns from data. The field has gone through an explosive advancement in the recent several decades such that its applications have expanded tremendously to various fields, and remote sensing is one of these fields. ML is widely applied in many remote sensing applications, especially land use and land cover (LULC) mapping. In LULC mapping, satellite/aerial images are converted into classification maps in which pixels are labelled as their LULC types, and ML is playing an important role in this process. Advanced ML models such as support vector machine (SVM), decision tree (DT), neural network (NN) have been used in numerous research for LULC mapping and has achieved high accuracies comparing with traditional classification methods (Cai et al., 2018; Mira et al., 2019; Thenkabail et al., 2005; Z. Yu, Di, et al., 2018). ML is now widely accepted in remote sensing field as a standard tool for operational satellite image classification. For example, the National Land Cover Database (NLCD) classification for the contiguous U.S. uses decision tree as the classification model (Maxwell et al., 2018). As the spatial, temporal, and spectral resolution increases with the most recent satellite images, and more freely available optical and radar images available nowadays, applying ML to remote sensing applications have received unprecedented attention. The large volume of high spatial and temporal resolution images allows for more specific LULC mapping missions, such as crop type mapping and crop system mapping. The entire LULC mapping process is very complex. It involves critical steps like image selection, image pre-processing, feature extraction and selection, model selection, model training and validation, and post-classification processing. This review will look into agriculture mapping-related research that uses ML methods and summarize the ML methods they have used, and their findings about advantages and disadvantages of their selected models and what are factors that influence model performances.

2.2.1. Supervised learning

Supervised classification is the most widely used ML practice for crop mapping. Supervised classification relies on ground truth samples (Maxwell et al., 2018; S. Wang et al., 2019). In remote sensing, ground truth samples are typically collected by conducing field surveys or manually digitizing sample points or polygons on georeferenced high-resolution images, such as Google Earth Pro (S. Wang et al., 2019). The ground truth samples are then used to sample from remote sensing images to be classified to get sensor readings and/or other derived features at these sample locations. The whole sample set is then divided into training and validation set/testing set. A ML model is then trained by an optimization algorithm on the training dataset to get the optimal parameter sets for the ML model. Lastly, the trained model performance is evaluated using the untouched validation set by comparing predicted label and true label of each sample. There are many ML models that fits in the supervised learning category, they can be roughly classified into parametric models and non-parametric models (Faridatul & Wu, 2018). Parametric models are ML models with fixed number of parameters. This category includes maximum likelihood estimations (MLE), logistic regressions (LR), NN, etc. Non-parametric models are models that do not assume a fixed size parameter model, i.e., the number of parameters will change as input size changes. Common non-parametric models include tree-based models such as k-nearest neighbors (kNN), DT, Random Forest (RF), and SVM with Radial Basis Function (RBF) kernel. We will look at each of these models in detail.

kNN is one of the simplest non-parametric models in ML field. The model simply memorizes all the training data and predict new samples by selecting the k samples within the training dataset that are closest to the new sample and do a majority vote among all k samples to get the prediction (Xiao et al., 2021). This model is a “lazy” model in that it does not take time in the training phase, instead, it takes most resources during prediction because the distances from training samples to the new sample need to be calculated every time a prediction is conducted (Maxwell et al., 2018). kNN model is known to suffer from outliers and high dimensionalities. Thus, it is not very well suited in remote sensing image classifications because remote sensing image classifications generally involve many dimensions. Xiao et al. (2021) explored using a subspace-KNN model to classify Sentinel-1 SAR data for 10 LULC classes (6 crop-related classes and 4 other LULC classes). Mira et al. (2019) also used kNN in their research on classifying crop types using multi-temporal Sentinel-2 images. Specifically, they compared performances of standard kNN algorithm, DT, and RF when classifying 18 crop types in a 10km-by-10km area using 9 spectral bands from Sentinel-2 and 7 derived indices as features. Their results showed that RF performed the best which agrees with many other research work (Mira et al., 2019). More interestingly, their result showed that kNN performance dropped 2% when spectral indices are added into the feature set, resulting in a 480-dimension dataset. This can be attribute to the disadvantage of kNN model not very suitable for high-dimension data. Chakhar et al. (2020) did a comprehensive comparison of 22 models that are variations of 5 groups of ML models including kNN, discriminant analysis, SVM, DT, and ensembled trees. For kNN specifically, they included 6 variations of kNN, i.e., different combinations of distance metric and k values. The distance metrics they included are Euclidean distance, cosine similarities, cubic distance and distant weights, and k values they tested are 1, 10, and 100. However, the reasoning behind choosing such parameters is not given. Their results showed that the kNN model with Euclidean distance metric and k=1 performed best among all 6 models. The overall best performance is achieved by a subspace-kNN model (Chakhar et al., 2020). With more and more advanced models are introduced and researched, kNN has becoming less popular. Nonetheless, kNN is still one of the best models if training dataset is not too large and the dataset is well-balanced. It is not recommended to use kNN if data dimensionalities are large (Maxwell et al., 2018). In the reviewed research, the choice of k value seems arbitrary. Smaller k tends to have complex decision boundaries, which means high variance, and overly large k leads to high bias. Thus, choosing a good k value is pivotal for successfully applying kNN. Ensemble of kNN, such as subspace-kNN is generally reported to perform very well (Chakhar et al., 2020; Xiao et al., 2021). We will discuss ensemble of kNN in the ensemble section.

SVM is a non-parametric binary classification model that aims to not only make good classification, but also maximize the confidence of classification by maximize the distance between decision boundaries to the sample points (Maxwell et al., 2018). The samples that are closest to the decision boundary are called support vectors. The support vectors help SVM solvers to find the Optimal Separation Hyperplane (OSH) that not only minimizes training error, but also maximizing the distances from support vectors to the OSH (S. Chen et al., 2020; Virnodkar et al., 2020). SVM can choose different kernels. Most commonly chosen kernels include linear kernel, and RBF (Sheykhmousa et al., 2020). SVM with linear kernel is typically used on linearly separable data. When data is not linearly separable, RBF kernel is recommended. RBF kernel is used to transform data into higher dimensions in which data can be linearly separable (Sheykhmousa et al., 2020). Most research reported that using RBF kernel is preferred over linear kernel for remote sensing image classification (Feng et al., 2019; She et al., 2020; Virnodkar et al., 2020). SVM generally works well with small sample size (S. Chen et al., 2020; She et al., 2020). As SVM is a binary classifier by design, it is mostly used in two-class classification (Cui et al., 2020; She et al., 2020). Although it can be extended to classify multiple classes using one-vs-all or one-vs-one schemes, other multi-class classifiers by design are more preferable. Another drawback of SVM is reported by Sheykhmousa et al. (2020) that SVM is sensitive to overfitting. She et al. (2020) compared SVM, RF and NN for classification of maize and soybean using Multi-temporal Sentinel-2 images. Their result showed that the performance of SVM is the worst of the three, and RF performed best (She et al., 2020). Mazarire et al. (2020) compared SVM and RF on classifying nice crop types and their result showed that SVM achieved better performance than RF (95% vs. 85% OA). Zeyada et al. (2016) explored using SVM to classify rice, maize, grape, and cotton using RADARSAT-2 SAR data. They tested using polarimetric decomposition parameters as features and using 4 components from PCA transformation as features for classification and compared performance with DT and NN. Their results showed that SVM achieved best balance of training and testing error and SVM with polarimetric decomposition parameters performed slightly better than SVM with PCA-derived components (Zeyada et al., 2016). SVM is one of the most used ML models in remote sensing. Its performance is generally similar to more advanced models such as RF and NN with proper parameter settings. Because of its good performance, many recent research works still use SVM in their research (S. Chen et al., 2020; Jia et al., 2018), or to compare with other models (She et al., 2020; Taona Mazarire et al., 2020), or to be used as a baseline model to validate new methods.

DT is a tree-based non-parametric model. It builds a tree by repeatedly splitting data into subsets such that data that do not belong to the same class are not in the same node (Friedl & Brodley, 1997). Classification and Regression Tree (CART) introduced by Breiman (1984) is one of the most popular DTs. Training of a DT is basically selecting the best feature and splitting value at each node of the tree. The information gain or Gini impurity is usually used as metrics to determine how to best split a node. DT is well-known for its tendency to overfit because data can be split indefinitely until no leave nodes are impure (Friedl & Brodley, 1997). Thus, DT often employ pruning methods to combat with overfitting. These methods include setting maximum height of the tree, or minimum number of nodes in each leave node, etc. Many research works also build DT by manually setting split rules based on domain knowledge (Jiang et al., 2020; Tian et al., 2019). If a DT is built using information gain or Gini impurity, feature importance can be inferred by looking up how much each feature contribute to the node splitting. The feature importance can then be used to do feature selection. Research that used DT in their research often reported feature importance (Valcarce-Diñeiro et al., 2019). Another important advantage of DT is that it is a very interpretable model (Friedl & Brodley, 1997; Z. Yu et al., 2020). However, many research works reported that DT cannot perform as well as other methods such as SVM and RF (Chakhar et al., 2020, 2021; Mira et al., 2019; Zeyada et al., 2016). Indeed, as ensemble of DTs, e.g., RF, Adaboost, Gradient Boosting, etc. becoming popular, DT is less used along in recent research.

Ensemble methods are becoming more and more popular in the ML field. Instead of using single learners as is with kNN, SVM, and DT as discussed before, ensemble learning combines multiple learners such that the combined learner is better than any learners used alone (Sonobe et al., 2018). Common ensemble methods include Bootstrap Aggregating (Bagging) and boosting.

Bagging is an ensemble learning method that trains each model in the ensemble using a randomly drawn subset of the training set in order to promote model variance. Note that the subset is drawn with replacement, which means a sample can appear multiple times within a subset, and it can appear in multiple subsets. The models within the ensemble are equally weighted, which means each model contribute equally to the final prediction. RF is one of the most famous ML models that uses bagging ensemble strategy (Breiman, 2001; Pal, 2005). RF is built with many DTs. Each DT is trained with a bagged subset of training data, and during the training of each DT, only a randomly chosen subset of feature space is used to split a node. This additional layer of randomness makes RF different from other bagged trees. Because each tree is built with less data and less features, individual trees are less accurate but less correlated, which makes the ensemble more reliable (Maxwell et al., 2018). RF introduced many advantages over traditional DT. First of all, RF is robust against overfitting. As long as the number of trees in the RF is sufficiently large, even without pruning of individual trees, i.e., individual trees overfit, the overall ensemble is not overfitting (Breiman, 2001; Pal, 2005). Training RF is fast even with large number of trees because each tree is independent, which makes the training parallelizable. Similar to DT, RF can also infer feature importance. Other advantages include not sensitive to noise, and not sensitive to high dimensionality (Sheykhmousa et al., 2020). There are numerous research works in remote sensing that uses RF to classify crops. To name a few, Orynbaikyzy et al. (2020) used RF in their effort to classify crop types by fusing optical and SAR data at feature and decision level. Rahman et al. (2019) explored classifying early-season crop types in U.S. using automatically extracted trusted pixels as ground truth samples. They compared RF against other 5 models that found RF performed the best. Singha et al. (2019) used RF to produce 10m resolution paddy rice map for the entire Bangladesh using Sentinel-1 VH bands. RF is one of the most successfully applied ML models in remote sensing due to its simplicity, high accuracy and little data pre-processing required.

Boosting is another form of ensemble. Instead of building a bag of uncorrelated learners, boosting builds a series of 'weak learners' one by one. A weak learner is a learner that performs slightly better than randomly guessing. Though each learner is not performing well, but as long as the performance of each one is slightly better than random guessing, the final model can be proven to converge to a strong learner. When using boosting, each learner is built trying to correct errors of the previous one (Sheykhmousa et al., 2020). The overall prediction is made by a weighted vote of all weak learners. The weights are distributed to weak learners based on their accuracy. Adaptive Boosting (Adaboost) is one of the most used tree-based boosting methods (Z. Zhou et al., 2015). Boosting is not as popular as RF in remote sensing field. Zhou et al.

(2015) used Adaboost to classify sugarcanes using time-series Chinese HJ-1 CCD images and their result showed their accuracy can reach to 93.6%. Li et al. (2015) applied the Adaboost strategy using SVM as weak learners to extract crop area. The advantage of boosting is that it can achieve very high accuracy (Han et al., 2014). It is also less likely to overfit if sufficient number of weak learners are used. However, many research works reported that boosting is more susceptible to overfitting (Sheykhmousa et al., 2020), which is contradicting to theory. Another disadvantage of boosting is that the learners need to be trained in sequence and there is no room for parallelism, which makes the training slow.

Other than bagging and boosting, which are most popular ensemble methods, especially for ensemble of DTs, there are other ways to combine models for prediction. Traditional ensemble methods assume the same base learners, e.g., DT is used for RF. There are other general ensemble methods that can be used to integrate different models. Subspace ensemble is an approach that trains base learners with randomly selected subsets of features. Note the subset feature space is bootstrapped such that same feature may present in the same subset multiple times. Xiao et al. (2021) used kNN as the base learner for a subspace ensemble method in an attempt for classification of 10 crop types in China. Their subspace kNN trains a set of kNN models with bootstrapped subsets of all features, and the trained kNN models jointly produce the final prediction with a majority vote. Their result showed the subspace-kNN performed better than RF classifier, and the overall accuracy reached 98% (Xiao et al., 2021). Chakhar et al. (2021) and Chakhar et al. (2020) also used subspace kNN in their comparisons with 21 other models and found that subspace kNN performed best using Sentinel-2 images for crop classification and it gets outperformed by SVM when using Sentinel-1 images. Ghazaryan et al. (2018) employed a decision-level fusion of classification results by SVM and RF using the subspace ensemble method. They trained a SVM and RF for each subset of features and combined all such SVM and RF models for final prediction. Super Learner (SL), also called stacking. It is an ensemble method that combines multiple models by assigning them weights such that cross-validated empirical risk is smaller (Sonobe et al., 2018). Sonobe et al. (2018) successfully applied SL in an attempt to combine RF and SVM for crop classification. Their result showed marginal improvement of combining RF and SVM over RF and SVM alone by 0.2%.

Neural networks (NN), also called multi-layer perceptron (MLP), are gaining attention in recent years. NN is comprised of layers of interconnecting perceptron as a simulation to human brain (Abburu & Babu Golla, 2015). Each perceptron is no more than a linear combination of input features and a non-linear activation function. Though neural network methods have been introduced very early on, recently years see major development in this method through back propagation optimization method (Cai et al., 2018). NN does not assume any structure, i.e., the structure of the NN is itself a hyperparameter. Some research claim that NN with only one hidden layer is considered shallow, and more hidden layers can be classified as deep NN (DNN) (Hänsch et al., 2018). An increasing trend of applying NN in remote sensing field can be observed. Cai et al. (2018) used a DNN with 3 hidden layers in classifying major crops in the U.S. using CDL as ground truth. Their results showed that DNN outperformed SVM and RF. They also reported that 3 hidden layers does not differ much from 7 hidden layers though 7 hidden layers is more stable. Shelestov et al. (2017) compared all ML models provided on GEE including NN for crop type mapping. Their result showed that NN outperforms other models including SVM, CART, and RF. Zhang et al. (2021) used a NN in classification of major crops in U.S. using trusted pixels extracted from CDL. Though the details of configuration of their NN is not given. The NN is known to be a model that can approximate any function, which makes it a ‘universal’ model for any scenario. However, there are some major issues of using NN in remote sensing applications, especially crop mapping. As ground truth samples used in crop type mapping is generally acquired by field trips or manual digitization, the sample size is generally small. However, NN generally have large number of parameters, which means a large number of training samples are needed for NN to converge. Because of this, we see that some of the research that successfully applied NN uses some automatic sample generation process, such as sampling from existing data sources (Cai et al., 2018; C. Zhang et al., 2021).

2.2.2. Unsupervised learning

Unsupervised learning is a less popular choice compared with supervised learning. Unsupervised learning aims to identify patterns in the data. Clustering is the most common approach in unsupervised learning. Clustering-based algorithms group pixels into clusters without any prior of class information (Lu & Weng, 2007).

K-means is one of the most widely used clustering methods. It starts by randomly choosing k centroids, and an iterative process is conducted until converge. Specifically, points are assigned to their closest centroid, and the new centroids are derived using sample points that are assigned to each centroid, points are then assigned to new centroids, and new centroids are generated. Brinkhoff et al. (2020) performed k-means to cluster training samples, and they analysed clusters and filtered unwanted training samples for target classes. The filtered training set was used to classify 9 perennial crops.

Gaussian Mixture Model (GMM) is a generalization of k-means. It is a probabilistic model that aims to find k unknown Gaussian distribution that maximizes the joint probability of all sample points. Instead of hard assigning sample points to centroids (Gaussian mean in GMM), each sample is given a probability of belonging to each Gaussian (S. Wang et al., 2019). Wang et al. (2019) explored using transferred RF model and unsupervised learning for crop type classification in US mid-west. Both k-means and GMM are explored in this study, and they found that GMM performs well in one state, but performed bad in other states, and k-means performed consistently bad.

Ma et al. (2020) explored using an unsupervised classification method based on Principal Components Isometric Binning (PCIB) method to classify rice and maize. Despite that the results of their proposed method are slightly worse than using supervised classification with the RF model, the advantage of not requiring ground truth labels is potentially more suitable for large scale crop type mapping.

2.3. Multi-sensor image fusion

Combining multiple remote sensing data sources for land use land cover mapping has been studied for a long time. Although data from a single source has the advantage of being consistent in the data format, spatial resolution, and calibration, it is often inadequate for certain applications because the spatial resolution is too coarse, or the revisiting time is too long. For example, the Moderate Resolution Imaging Spectroradiometer (MODIS) can provide up to 1-2 days revisiting time, which is very suitable for global scale mapping and monitoring. However, its spatial resolution is only at most 250m, which can be too coarse for field-level mapping, especially for certain regions where field sizes are very small. Combining multiple remote sensing data sources is promising because a broader information content for the target object can be utilized, and the merits from each data source may be combined (Orynbaikyzy et al., 2019). In Pohl and Van Genderen (1998), the image fusion is to integrate different sources of remote sensing data to provide more information than that can be provided by each source alone. Fusing optical remote sensing data (MODIS, Landsat, Sentinel-2, etc.) and Synthetic Aperture Radar (SAR) data (RADARSAT, Sentinel-1, etc.) is especially useful because optical and SAR sensors offer very distinct aspects of the target object. Specifically, SAR is an active microwave radar sensor that emits polarized radio waves to the ground and record the backscattered energy from the targets. The backscattered signal carries information about properties of the surface, such as roughness, geometry, moisture, etc. (Moreira et al., 2013) SAR generally emits radio signal whose wavelength is much larger than the particles and water vapors in the atmosphere, which allow the signal to penetrate cloud without interference. This particular trait makes SAR a desirable data source because optical data typically suffer from cloud covers (Kulkarni & Rege, 2020). On the other hand, optical sensors often provide rich multispectral measurement in the visual, near infrared (VNIR), and shortwave infrared (SWIR) spectrum range. Different objects absorb/reflect different portions of energy in the VNIR spectrum range such that they have unique spectral signature, which is why multispectral images are crucial for identifying the sensed objects. Optical images and SAR images complement each other because multispectral images bring spectral information to SAR and SAR provide consistent observations regardless of the weather conditions.

The image fusion can be done at three different levels, i.e., pixel-level, feature-level, and decision level (Pohl & van Genderen, 1998). Pixel-level fusion is the lowest level that the image fusion can be applied. It aims to produce a new image dataset from multiple source datasets such that the new image dataset encompasses all information from the source datasets. The source datasets need to be co-registered and resampled to the same projection and same spatial resolution. Feature-level fusion is the fusion at object-level, i.e., an image segmentation step is first applied to identify objects, or pixels blobs, and then features for the objects are derived using different data sources for further analysis. Lastly, decision-level fusion is to conduct information retrieval from each data source individually, and then fuse the information together to resolve potential disagreement and reinforce the understanding of the observed objects (Pohl & van Genderen, 1998). The following discussion will focus on scientific approaches of combining optical and SAR image data.

Pixel-level fusion between optical and radar images require the input images to be co-registered and resampled to the same map projection (Pohl & van Genderen, 1998). The SAR data also needs to tackle with speckle noise. Pixel-level fusion approaches of optical and SAR data can be grouped into several classes: component substitution, multi-scale decomposition, hybrid, and model-based methods (Kulkarni & Rege, 2020). The simplest form of pixel-level fusion is band stacking, i.e., combining optical time-series and radar time-series together such that each pixel has both spectral bands and SAR image bands (Blaes et al., 2005; Haack et al., 2000; Orynbaikyzy et al., 2019). Component substitution typically transform optical images into a new space, and the SAR image is used to replace a component which usually does not contain much spectral information. Most commonly used methods include Principal Component Analysis (PCA), Intensity-Hue-Saturation (HIS) transform, Gram-Schmidt (GS) orthogonalization, and Brovey Transform (BT). PCA is one of the most popular methods within this category (Herold & Haack, 2002; Orynbaikyzy et al., 2019). PCA is a method that transforms original image space into a new space in which components are orthogonal to each other (Z. Wang et al., 2005). If ranked by the corresponding eigen values, the first a few components preserve most of the information in the original image space. For optical-SAR image fusion, the multi-spectral image is transformed using PCA. The first component from the PCA result is then replaced by the SAR image, and the inverse PCA procedure is conducted to get the fused image (Kulkarni & Rege, 2020). Another component substitution technique is the IHS transform. It takes an RGB image and transform into the IHS color space where the color information is preserved in Hue and Saturation band, and the Intensity band can be substituted by another grey-level image (Kulkarni & Rege, 2020). It is a popular method in pan-sharpening where the intensity band can be substituted by the panchromatic band (El-Deen Taha & Elbeih, 2010). However, this method only works on RGB images, thus, it is not very suitable for agriculture applications in which NIR, and SWIR bands are very important. GS method is similar to PCA. It is originally used as a pan-sharpening method (Maurer, n.d.). Unlike PCA, GS uses an arbitrary band as the first component, and other bands are computed to be orthogonal to the chosen band (Kulkarni & Rege, 2020). In optical-SAR image fusion, the SAR image is used as the first component and multispectral bands are computed to be orthogonal to the SAR image and then an inverse transform is conducted to get the fusion image (Yang et al., 2016). BT is a similar method to IHS. Its purpose is to normalize the RGB bands and to multiply the result by any other desired data to add the intensity or brightness component to the image (Z. Wang et al., 2005). Because it only uses 3 bands as input, its potential is limited for multispectral images. Multiscale decomposition methods are another group of pixel-level image fusion techniques. In these methods, the source images are first decomposed into sub-images at different scale using a multiresolution method, and then fusion is applied to sub-images at all scale, which then are converted back to get the fused images (Kulkarni & Rege, 2020). For optical-SAR image fusion specifically, the non-subsampled wavelet transform is a good choice because it is shift invariant, which means images from different sensors without co-registration can benefit from this characteristic (Kulkarni & Rege, 2020). The choice of multiscale decomposition method and the fusion method are decisive parameters to successfully apply multiscale decomposition to image fusion. Hybrid methods are methods that combine the component substitution and multiscale decomposition methods. For example, the IHS transform is applied to multispectral image and the intensity band along with SAR images are used as input to a multiscale decomposition method. The fused image is then used to substitute the original intensity band, and the inverse IHS transform is applied to get the final fused image (Kulkarni & Rege, 2020). Model-based methods mainly includes variational models and sparse-representation models. Zhang et al. (2010) extended the original variational model which was applied in pan-sharpening field to the optical-SAR image fusion. The variational model is an optimization problem that aims to find transform parameters that minimizes an energy function (Kulkarni & Rege, 2020; W. Zhang & Yu, 2010).

Image fusion at feature level works with objects or features. Specifically, each sensor derives a set of features for the targeting object, and the derived features jointly grouped into different clusters. Then the features within the same group are fused together for further analysis (Zeng et al., 2006). The fusion techniques at feature-level are mostly drawn from fields like artificial intelligence, statistics, information theory, etc. The simplest form of feature-level fusion is to stack multispectral bands from multispectral images and backscatter bands from SAR images together for further analysis (Rajah et al., 2018). Further, sensor-specific features can be derived individually and used together for further analysis. Denize et al. (2019) derived multiple indices including NDVI, NDWI, NDSI from Sentinel-2 images, and derived multiple parameters from Sentinel-1 Single-look-complex (SLC) images and a VH/VV ratio. These parameters are used together as input to classification models in the later procedures.

Decision level fusion is the fusion at the final step. It typically involves conducting mapping individually using input images and produce the final result with outputs from all input sources (Ghassemian, 2016). The fusion at decision level is to resolve conflicts between input sources and reinforce consensus among all sources. A common method of fusion at decision level is voting. The voting can be unweighted, meaning that each input is treated equally, and they contribute equally to the final output. It can also be weighted to control the influence of each input source (Ghassemian, 2016). Another slightly different strategy is rank based. Instead of voting for a final fixed result, the final result can be a probability vector of all possible labels.

2.4. GEE application in agriculture mapping

Traditionally, remote sensing data processing takes non-trivial work because of the sheer volume of data that need to be downloaded and processed at local workstation. However, the advent of GEE (Gorelick et al., 2017), and the recent development from Microsoft, the Planetary Computer has made remote sensing data processing much easier thanks to the underlying cloud computing infrastructure. GEE provides researchers Application Programming Interfaces (APIs) to process and visualize remote sensing datasets by writing JavaScript code in the online code editor. The large catalog of remote sensing-related datasets available and the built-in data filtering APIs make it very convenient to select images that are relevant to the time frame and study area of interest (Amani et al., 2020). Aside from expediting research process, GEE is also beneficial to open research because researchers can share the scripts that generated the research results, which can be easily used by other researchers to reproduce the research. As a result, we can observe an exponentially increasing trend of GEE publication numbers since the introduction of GEE (Amani et al., 2020). GEE can also be used to build web applications. The advantage of building web application is that it can engage users who do not have JavaScript experience with easy-to-use GUIs. GEE JavaScript APIs include built-in UI components such that researchers can build simple web applications right in the online code editor and host the applications with Google App Engine. O-LCMapping introduced by Xing et al. (2021) is one of such examples. O-LCMapping provides users with GUIs to select ground truth data on the map, specify satellite sensors, image date ranges, band combinations, machine learning (ML) models, and model parameters, and then use user-defined parameters in a supervised or unsupervised land cover classification workflow (Xing et al., 2021). AgKit4EE is a suite of useful functions for Cropland Data Layer (CDL) (C. Zhang et al., 2020). Zhang et al. (2020) used it and developed web applications to visualize CDL data based on user-defined configurations. Another type of web application that can be implemented using GEE is free-form web applications that only uses GEE-provided computing power rather than the UI components. This type of web applications is much more flexible but require substantially more work to design, implement, and deploy. Climate Engine is a sophisticated software that provides users with plenty of options to visualize and download climate and remote sensing data for natural resource monitoring purposes (Huntington et al., 2017). Yalew et al. (2016) presented a GEE-based web framework for agricultural land suitability assessment named AgriSuit. The framework uses GEE in the backend for data processing and computing and implements a web-client to collect user inputs and visualize processing results (Yalew et al., 2016). REMAP is a web application for land cover classification similar to the O-LCMapping except that it uses GEE Python APIs instead of JavaScript APIs (Murray et al., 2018).

3. INLAND FISHPOND MAPPING IN BANGLADESH

3.1. Background

Fishery in Bangladesh has been increasing rapidly in the last few decades as a major source of food and economic growth (Hashem et al., 2014). According to the International Food Policy Research Institute (IFPRI), the fish farming market has grown 25 times in all aspects of the aquaculture industry in the last three decades. Shahin et al. (2015) also reported that the total fish production increased from 4.99 Lac MT (100,000 metric tons) in 1998-1999 to 14.47 Lac MT in 2012-2013. Though rice is still the major food source for Bangladesh, the booming aquaculture is bringing diversity to the dietary structure of people in Bangladesh and gradually improving people's health conditions (Thilsted, 2012). However, the growing aquaculture puts pressure on already limited croplands. In recent years, a great portion of croplands has gradually transformed to other land use types, such as fishponds, brickyards, and residential area in Bangladesh (Hashem et al., 2014). With Earth Observation (EO) data, especially newly published Sentinel-2 MSI 10m resolution images, mapping and monitoring individual fishponds become feasible.

There are many research works focus on mapping aquaculture ponds in coastal area (Ottinger et al., 2017; Prasad et al., 2019; Virdis, 2014). However, inland fishponds differ from coastal aquaculture ponds in that inland fishponds are typically owned by individual families, which means they can have arbitrary shape and size and they are not necessarily well-aligned as many coastal aquaculture ponds do. Some key features of fishponds in Bangladesh are that:

1) they are usually filled with water all year round,
2) they are small, and
3) like many other man-made objects, they have regular boundaries and simple shapes such as rectangles.

To address 1), multi-temporal and multi-spectral remote sensing images should be used. High-resolution images are the most suitable data to address 2). Specifically, based on the research conducted by Belton and Azad (2012), the average size of homestead fishponds in Bangladesh is between 0.08 to 0.1 ha, the median value can be even less due to the skewness towards a few large fishponds, which can go up to over 100 ha each. Fishponds with such small size are challenging to detect on medium-resolution (2 – 30m) remote sensing images, and it is almost not feasible to do with low-resolution (> 30m) images. However, high-resolution images such as SPOT (Satellite Pour l'Observation de la Terre) and IKONOS are usually not available free of charges. Sentinel-2 MSI L1C data has become increasingly popular for land use and land cover (LULC) mapping in recent years mainly because of its finer spatial resolution (10m) and temporal resolution (10 days before Sentinel-2B launches and 5 days after) (Du et al., 2016; Ludwig et al., 2019b; X. Yang et al., 2018). The significant improvement of both spatial resolution and temporal resolution offered great potentials of improving existing applications and enabling new missions such as object detections (X. Yang et al., 2018). Therefore, this research uses Sentinel-2 MSI L1C data for fishpond mapping.

Water indexes (WI) such as Normalized Difference Water Index (NDWI) (McFeeters, 1996b), Modified Normalized Difference Water Index (MNDWI) (Xu, 2006a), and Automated Water Extraction Index (AWEI) (Feyisa et al., 2014a) have been developed to enhance water features on multi-spectral images. Most of the WIs utilize low reflectance of water in near-infrared (NIR) and shortwave-infrared (SWIR) spectrum (Ji et al., 2009b; Ludwig et al., 2019b; McFeeters, 1996b; Y. Zhou et al., 2017a). NDWI takes the difference between the green band and the NIR band, which produce positive values for water and negative values for other LULC types (McFeeters, 1996b). To address false positives from built-up using NDWI, Xu (2006a) introduced MNDWI, which is calculated with green and SWIR bands. Previous research reported that MNDWI generally has a more stable threshold than NDWI (C. Huang et al., 2018; Ji et al., 2009b; H. Jiang et al., 2014). Aside from the NDWI and MNDWI that use 2 bands to compute, AWEI uses 5 bands to compute, and it aims to reduce false positives coming from shadow pixels (Feyisa et al., 2014a). The AWEI consists of two formulas, $AWEI_{sh}$ for areas that are contaminated by shadows, and $AWEI_{nsh}$ for areas that are not (Z. Wang et al., 2018a). Feyisa et al. (2014a) reported that AWEI has much more stable optimal thresholds than MNDWI.

While water classification on multispectral remote sensing images has been extensively studied, most of the research focuses on identifying general water bodies at national or even global scale (Fisher et al., 2016; Pekel et al., 2016), or selected water bodies in small study sites rather than identifying subclasses of water bodies. Therefore, how to discern fishponds from other water features is a major challenge in this study, and feature 3) of fishponds is utilized to address the problem.

Object-based features (OBF), also referred to as geometrical features in Yu et al. (2006), shape metric in Jiao et al. (2012), have been used in previous research as ancillary features in object-based image analysis. In a research work conducted by van der Werff and van der Meer (2008), shape measures were extracted from Landsat image objects and were used to help classify spectrally identical objects, e.g., rivers and different shapes of lakes. Jiao et al. (2012) used 10 shape metrics to classify 8 LULC classes including rivers and ponds on SPOT-5 images. Their results showed that such metrics can well characterize all LULC classes quantitatively. For water features specifically, they characterized rivers as elongated, concave, and complex, while ponds were round, rectangular, convex, and simple (Jiao et al., 2012). Both research works reported that OBFs significantly improved classification accuracy especially when objects are spectrally similar. However, previous research typically works with high-resolution images or objects that are large compared to the pixel sizes, it is unclear how such OBFs will help with classifying small objects on relatively coarse resolution images.

Therefore, we introduce an automatic workflow that incorporates spectral-based filtering with multi-temporal Sentinel-2 images and spatial-based filtering with OBFs for fishpond classification. The workflow was implemented on GEE (Gorelick et al., 2017). A case study in Singra Upazila in Bangladesh is conducted to test the performance of the workflow.

3.2. Study Area and Dataset

The study area of the case study we chose is the Singra Upazila (24° 30′ N 89° 08′ E) in Bangladesh as shown in Figure 3. It is a sub-district of Natore district in Northern Bangladesh that consists of 13 unions. More than three-hundred thousand people live in around 530 km^2 areas with a density of 607 persons per km^2. Around 80% of people in this area are engaged with agriculture, more specifically rice crop farming. Since this area is located within one of the largest flood plains of the country, most of the agricultural fields are flooded in the rainy season every year. A recent trend of land use change from crop fields to fishponds has been found in this area because of the larger profit of fish culturing than growing rice.

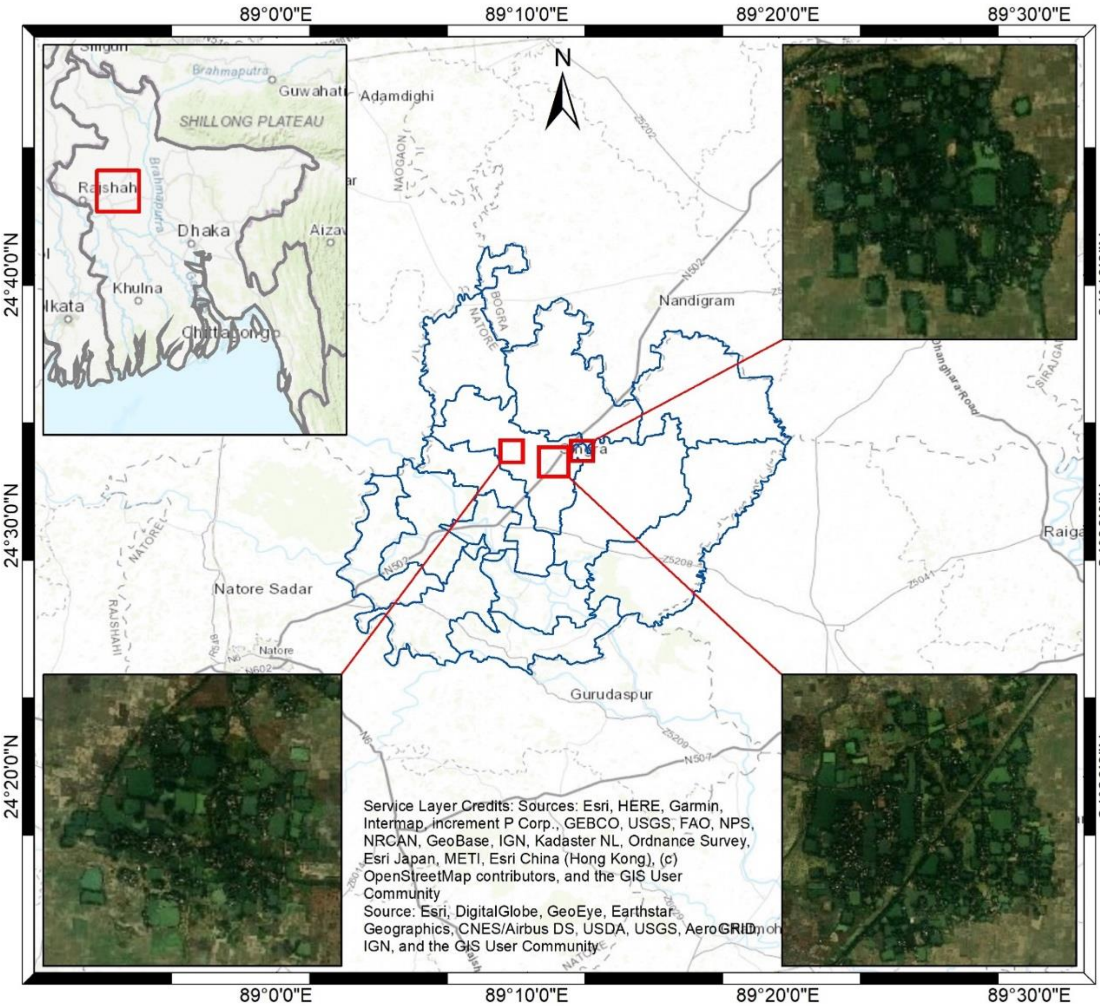

Figure 3. Study area: Singra Upazila.
(Upper left: location of the study area in Bangladesh. Upper right, lower left, and lower right: example fishponds within the study area.)

The dataset used in this study is the Sentinel-2 MSI Level-1C product hosted on GEE. It was preprocessed by radiometric and geometric corrections. As a result, the Sentinel-2 Level-1C is a Top-of-Atmosphere (TOA) reflectance dataset that consists of 100 km by 100 km image tiles projected in UTM/WGS84. The Multi-spectral instrument

(MSI) sensors onboard Sentinel-2 satellites collect images with 13 spectral bands in the visible/near-infrared (VNIR) and SWIR spectrums, and the spatial resolutions of the spectral bands vary from 10m to 60m. The bands that were used in this study are listed in Table 3. The MGRS (Military Grid Reference System) tile number of images used in this study is 45RYH.

Table 3. The Sentinel-2 Level-1C bands used in this study.

Sentinel-2 Band #	Band Name in WI formula	Wavelength (μm)	Spatial Resolution (m)
Band 3	Green	0.537 – 0.582	10
Band 8	NIR	0.767 – 0.908	10
Band 11	SWIR1	1.539 – 1.681	20
Band 12	SWIR2	2.072 – 2.312	20

3.3. Method

The methodology we used can be divided into two parts, (1) spectral filtering and (2) spatial filtering. The spectral filtering phase conducts image segmentation on multi-temporal Sentinel-2 images to detect all-year flooded water features. The spatial filtering phase further classifies water features into fishpond class and non-fishpond class based on OBFs. A diagram of the workflow is shown in Figure 4. Details are discussed in the following subsections.

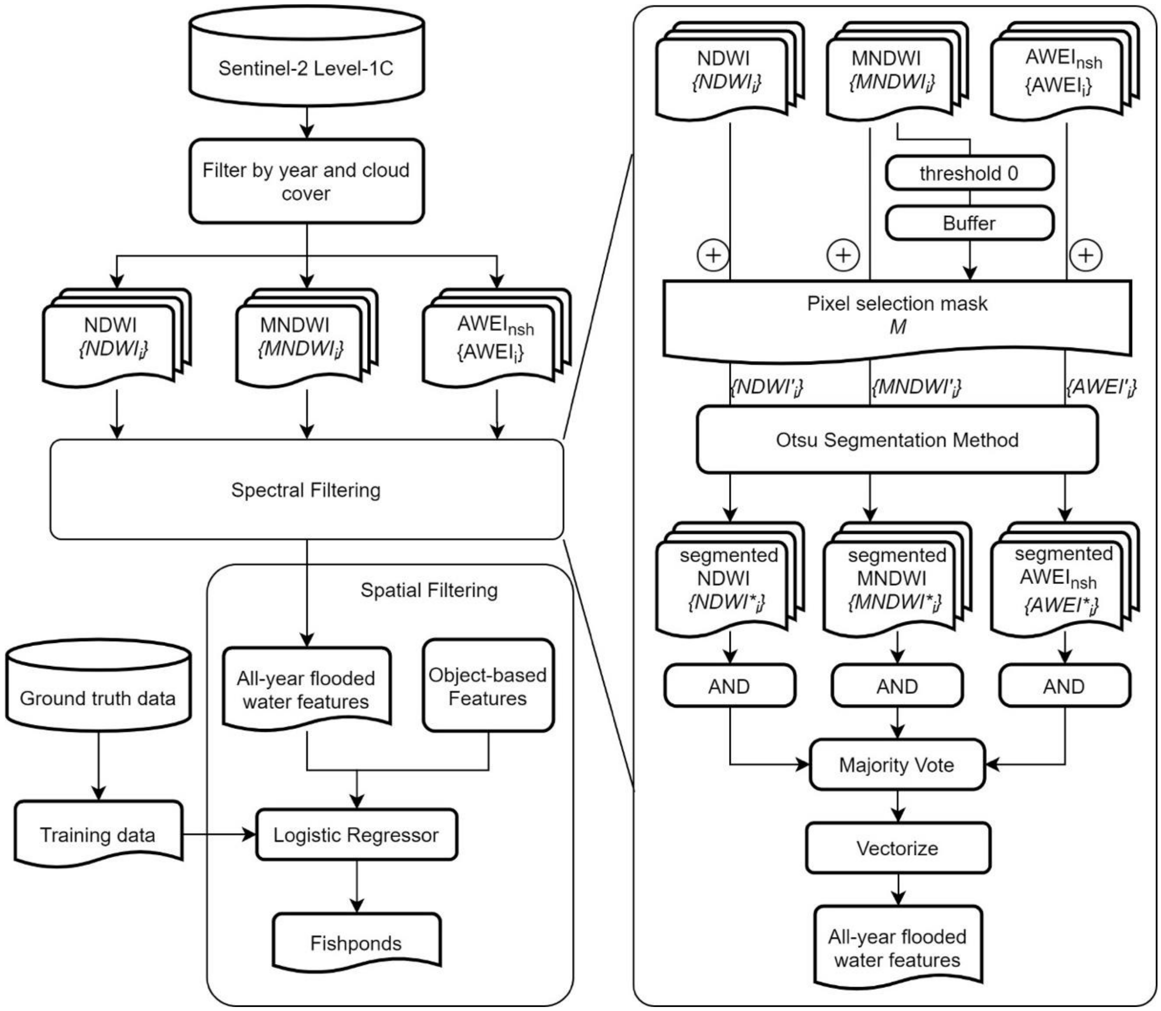

Figure 4. Proposed Workflow for fishpond mapping.

3.3.1. Data Preprocessing

Multi-temporal images are first prepared for the detection of all-year flooded water features rather than seasonal water features such as rice paddy and flooding (Ludwig et al., 2019b; Razu Ahmed et al., 2017; Xiao et al., 2005b). Specifically, all Sentinel-2 Level-1C images with less than 10% cloud cover in 2016 were collected. The images that satisfy the selection criteria are the four images in Jan 16th, Jan 31st, Apr 30th, and Oct 17th, 2016. Here we denote the image collection as $\{T_i\}, i = 1,2, \ldots, n$, where n is the total number of images. Note that due to extremely high cloud cover during monsoon seasons, no images are available between May and September.

Three WIs, i.e., NDWI, MNDWI, and $AWEI_{nsh}$ were calculated for each selected image T_i. We denote the three WI image collections as $\{NDWI_i\}, \{MNDWI_i\}, \{AWEI_i\}$. $AWEI_{sh}$ was not used because most fishponds are in rural areas where the noise from shadow is minimal. For the convenience of notation, the rest of the paper use AWEI to refer to the $AWEI_{nsh}$. Figure 5 shows the WI images for a selected area. As shown in the figure, fishponds show consistently high WI values while rice paddy and floods show seasonal variations.

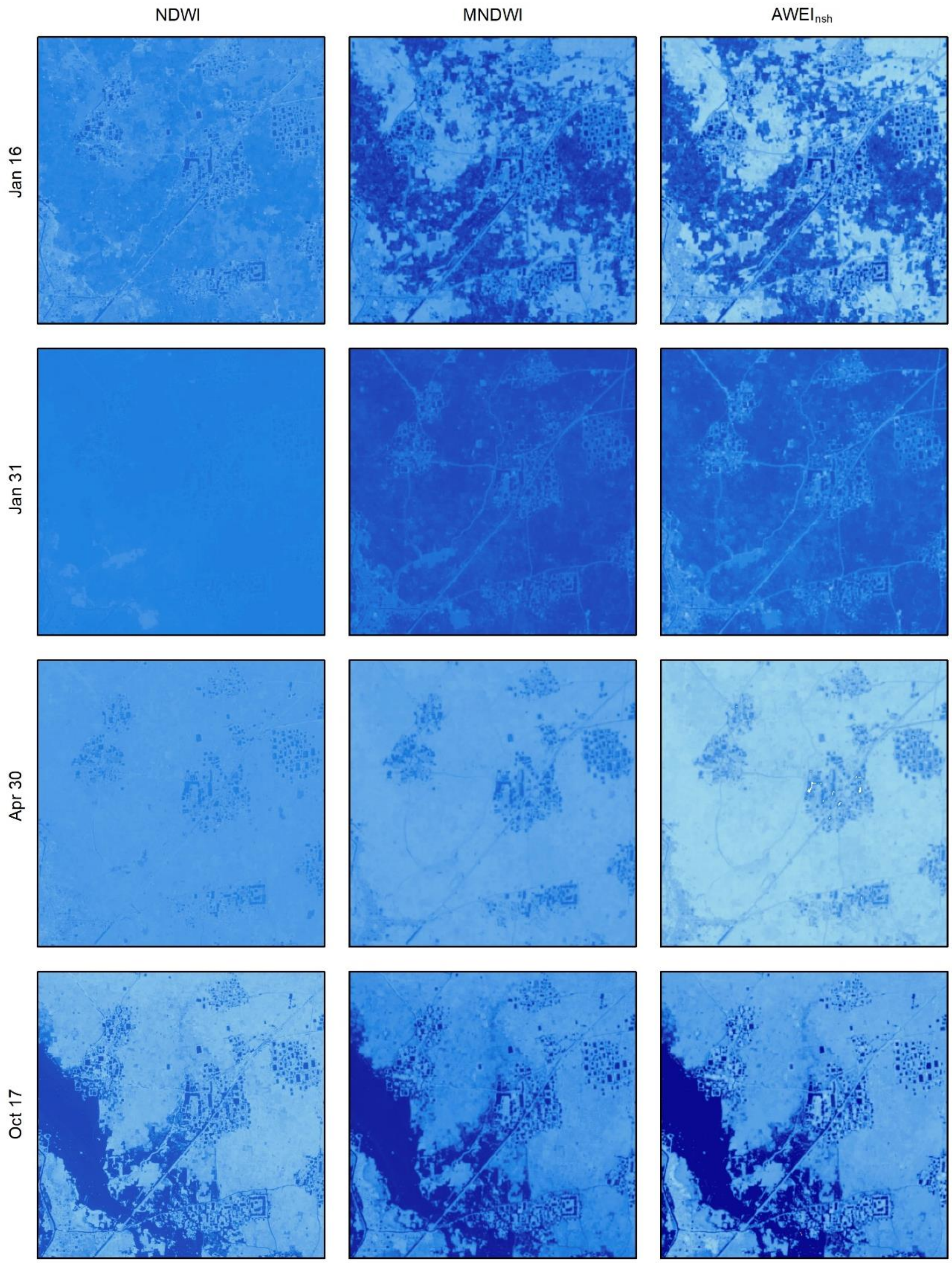

Figure 5. WI images of four dates in 2016 in an example area within the study area.
Value ranges for NDWI and MNDWI are -1 to 1, and -2 to 2 for $AWEI_{nsh}$. No color stretches are applied. Higher WI values are shown in darker colors.

3.3.2. Spectral Filtering

The threshold selection of WIs is the key factor of accurately mapping water on multispectral images (C. Huang et al., 2018; X. Yang et al., 2018). An empirical threshold 0 is chosen by default for many WIs (Ji et al., 2009b; McFeeters, 1996b; Sheng et al., 2016). However, due to mixed pixels of water and other land cover types, the optimal WI thresholds usually depend highly on the scene and locations (Feyisa et al., 2014a). Therefore, previous research uses dynamic thresholds to adapt to varying situations. Among many automatic thresholding algorithms, the Otsu method introduced by Otsu (2008), which is an automatic grey-level image segmentation algorithm that iteratively finds the optimal threshold that maximizes inter-class variance, is widely used for water body mapping (Calvario Sanchez et al., 2018; Donchyts et al., 2016; Du et al., 2016; Jakovljević et al., 2019; Kordelas et al., 2018; Ludwig et al., 2019b). In Yin et al. (2013), the Otsu method achieves the best performance among 8 other automatic thresholding methods, and its performance is on par with support vector machine (SVM) and optimal thresholds. The Otsu method is represented by Equation 1:

Equation 1. Otsu segmentation algorithm.

$$\sigma^2 = p_0(\mu_0 - \mu)^2 + p_1(\mu_1 - \mu)^2$$

$$p_0 = \frac{n_0}{N}, p_1 = \frac{n_1}{N}$$

$$t^* = argmax\sigma^2$$

where σ is the between-class variance, p_0 and p_1 are probabilities of two classes respectively, μ_0 and μ_1 are mean pixel values of class 0 and class 1 respectively, μ is mean pixel values of the whole data, n_0 and n_1 are numbers of instances of the two classes, N is the total number of instances, and t^* is the optimal threshold.

Many threshold selection methods favor bimodal histograms because thresholds can be easily found in the valley of two peaks without much uncertainty (H. Liu & Jezek, 2004; F. Zhang et al., 2018). Therefore, it is reasonable to do a pre-masking to reduce the number of non-water pixels in threshold selection for fishponds that are typically small and scarcely scattered in a large area. To achieve that, we adapted and modified a technique that was used in previous research (Donchyts et al., 2016; H. Liu & Jezek, 2004; F. Zhang et al., 2018). Specifically, a preliminary thresholding step was conducted using a forgiving threshold to loosely identify water features, and then buffers are generated around the water features to include some but not all non-water pixels. Detailed steps of this approach are described below:

a) An empirical threshold 0 was used for all multi-temporal MNDWI images, denoted as $\{MNDWI_i\}$, to loosely classify water features.
b) All classified MNDWI images were combined by inserting logical operator AND between images to get a single layer mask, denoted as M, where pixel value 1 represents all-year flooded water features.
c) The mask from b) was then vectorized by connecting neighboring same-value pixels.
d) Buffer polygons were generated from each water feature. The buffer distance was set to 5 pixels.

e) The buffered polygons were then rasterized as a binary mask image for pixel selection.

In the above steps, step a) and b) were to identify all-year flooded water features, step c) and d) aimed to generate a pixel selection mask that includes only a portion of all pixels, the masking operation is illustrated as follows:

$$\{WI_i \oplus M\} = \{WI_i'\}, \qquad WI \in [NDWI, MNDWI, AWEI]$$

Masked WI image collections $\{WI_i'\}$ were then used as input to the Otsu method, which produces thresholds for all images WI_i' within each collection $\{WI_i'\}$. The thresholds were then used to segment original WI images WI_i into binary classes, the segmented image collections are denoted as $\{WI_i^*\}$. Then, each segmented WI image collection, i.e., $\{NDWI_i^*\}, \{MNDWI_i^*\}, \{AWEI_i^*\}$ is self-combined by inserting logical operator AND between pairs of images, which produces single-layer consensus results where pixel value 1 represents all-year flooded water features. With all three single-layer results, the final all-year flooded water feature classification result was generated by conducting majority vote among all three layers, pixels that get more than 1 vote will be labeled as 1, the rest are labeled 0.

3.3.3. Spatial Filtering

The binary image generated from the spectral filtering part was firstly vectorized by connecting neighboring homogeneous pixels, which groups connecting pixels into objects. For each water feature vector object, several OBFs were computed using its perimeter, area, and the perimeter and area of its convex hull. The OBFs were then used to further classify all water features into fishponds and non-fishponds.

3.3.3.1. Object-based features

OBFs are representations of geometries which are usually used as auxiliary features in object detection (R. Chen et al., 2018; K. Liu et al., 2010). OBFs are effective in measuring the shape complexity of polygons (Jitkajornwanich et al., 2018; Moser et al., 2002). In this research, we mainly used OBFs that can be calculated with perimeters and the area of the target object and its convex hull because the workflow is implemented on GEE which has limited functionalities for object-based analysis. Table 4 summarized the OBFs that we used in this research.

Table 4. OBFs that were used in this research

OBF ID	Full Name	Formula
IPQ	Iso-Perimetric Quotient	$\frac{4\pi A}{P^2}$
SOLI	Solidity	$\frac{A}{A_c}$
PFD	Patch Fractal Dimensions	$\frac{2\ln\frac{P}{4}}{\ln A}$
CONV	Convexity	$\frac{P_c}{P}$
SqP	Square pixel metric	$1-\frac{4\sqrt{A}}{P}$

IPQ, also known as FORM (form factors), SI (shape index), is a widely used measurement of shape compactness (Jiao et al., 2012; W. Li et al., 2014; Moser et al., 2002; van der Werff & van der Meer, 2008; Q. Yu et al., 2006). The IPQ measures similarities between an object and the most compact shape, i.e., circles, and it is scale-invariant. The range of IPQ is 0 to 1 with 1 being full circles and 0 being infinitely complex shapes. SOLI (Solidity) measures the extent to which an object is convex or concave (Jiao et al., 2012). The range of solidity is between 0 and 1 with 1 being completely convex. PFD (patch fractal dimensions) or simply fractal dimension is another widely used measurement of shape complexity (Jiao et al., 2012; Moser et al., 2002). In the equation in Table 4, the perimeter of the geometry is divided by 4, which accounts for the raster bias in perimeters. PFD values are close to 1 when geometry shapes are simple, e.g., squares and rectangles. It approaches 2 when shapes become complex. CONV (convexity) is a measurement of the convexity of a geometry similar to SOLI. The value range for CONV is between 0 and 1 with 1 being convex shapes, and values less than 1 for objects with irregular boundaries (van der Werff & van der Meer, 2008). Lastly, SqP (Square pixel metric) is a very similar metric with IPQ, it measures the shape convexity of an object. SqP is 0 for a square and approaches 1 as the shape becomes more complex (Frohn, 2006).

3.3.3.2. Ground truth sample collection

To classify fishponds based on OBFs, we first manually digitized fishponds in randomly selected 7 of 13 unions that are within the Singra Upazila as ground truth data. Of the 7 unions, 3 randomly selected unions were then used to derive positive samples for training purposes, and the rest 4 unions were used to evaluate the method. Note that positive samples were simply a subset of water feature objects generated from the spectral filtering process that intersects with ground truth fishpond polygons. The reason why manually digitized ground truth polygons were not used directly for training purpose is that manually digitized polygons have over-simplified boundaries which cannot represent the true shapes of water feature polygons generated by segmenting remote sensing images.

In addition to positive samples, i.e., fishponds, negative samples of non-fishpond water features were collected using the JRC Yearly Water Classification dataset (Pekel et al., 2016). The JRC dataset provides 30-m resolution images of seasonal and permanent water features every year since 1984. Permanent water features from a region on Tibetan

Plateau were extracted as negative samples. The reasons to select a region on Tibetan Plateau rather than inside Bangladesh include:

1) Bangladesh does not include enough permanent water bodies for classification.
2) Tibetan Plateau has over 1200 lakes larger than 1 sq. km, and multiple river streams (G. Zhang et al., 2017).
3) Tibetan Plateau has over 4000 m average altitude, which significantly limited human activities such as fishery. Therefore, there are rarely any artificial water features in the area.

The JRC dataset is a 30-m resolution dataset, which is 9 times the resolution of Sentinel-2 MSI in terms of the pixel area. As a result, same-area objects on the JRC layer should have much simpler boundaries than on Sentinel-2 images. More specifically, same-shape objects on Landsat images should be 9 times as large as they are on Sentinel-2 images. According to Belton and Azad (2012), fishponds in Bangladesh are typically within a range of 0.02 ha and 100 ha. Therefore, to compensate for the simplification of shapes caused by the difference of spatial resolutions between the JRC dataset and Sentinel-2 images, water features that are 9 times the size of fishponds, i.e., water features that are within 0.18 ha to 900 ha in the region were selected. The geographic area used to select training samples is shown in Figure 6. In total 708 positive samples and 1086 negative samples were used in the training process.

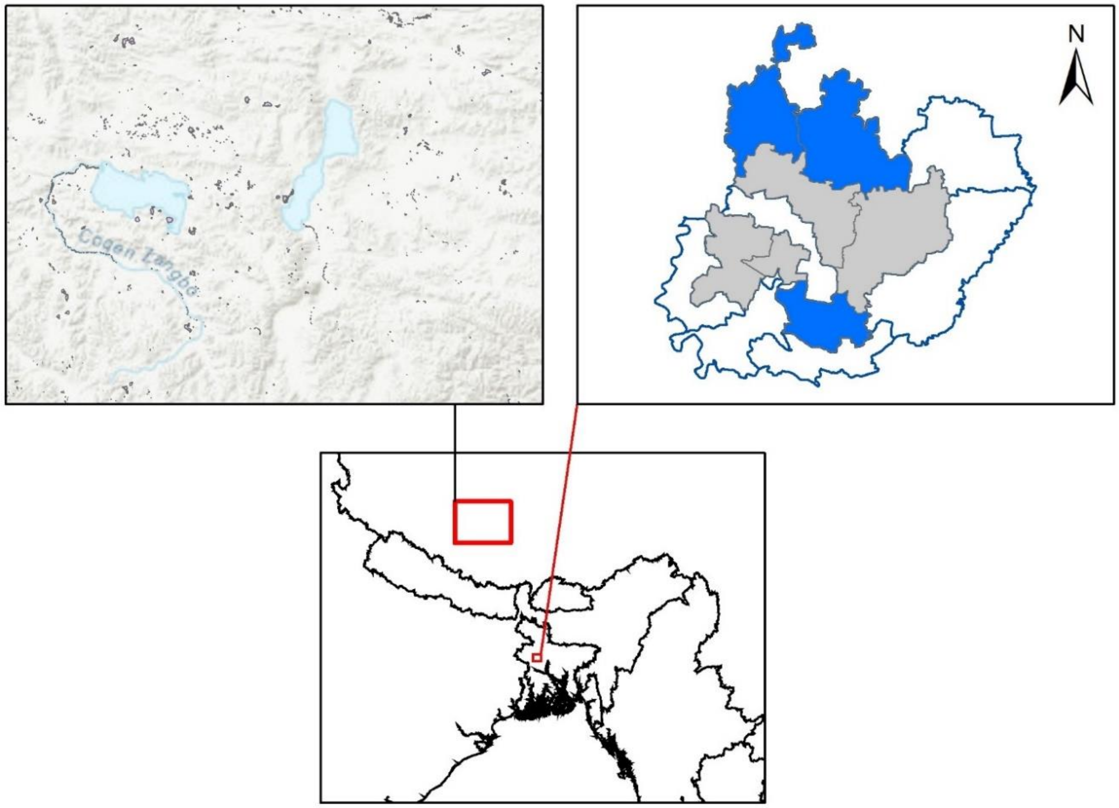

Figure 6. Locations of the region used to select training and test samples.
(Upper left: the region on Tibetan Plateau for selecting negative samples; upper right: blue unions are for training positive samples; grey unions are for testing samples).

3.3.3.3. Fishpond Classification

The last step of the workflow is to classify water feature polygons based on their OBF values. We compared two widely used classification models, i.e., the Logistic Regression (LR) model and Decision Tree (DT) model that are easy to implement on GEE and easy to interpret. The model with better performance was then selected and implemented as the classifier in the workflow.

DT is a widely used classifier that recursively partitions feature space to form purer small subspaces (Breiman et al., 1984). DTs are easy to interpret as decision rules are no more than a few chained thresholds on features. Moreover, DT provides feature importance score that can help with feature selection. LR is a widely used binary classifier. It has a solid theoretical background, and it is very fast to run due to its simplicity (Kleinbaum & Klein, 2010). It is also very simple to implement. A major reason of choosing LR and DT in this experiment is that it is trivial to transplant the fitted models to GEE because LR can be implemented as thresholding the weighted sum of all feature values, and DT can be implemented as a set of nested IF-ELSE statements.

3.3.4. Accuracy Assessment

As mentioned in the previous section, we manually digitized fishponds in our test site for 2016, which is the study year of this research, based on Google Earth historical satellite images. Among all digitized fishponds, a small portion was used for training purpose and the rest are used as testing samples. As we only have positive samples for testing, the evaluation was then based on the hit rate. Specifically, an identified fishpond is considered correctly identified if its centroid is within a ground truth polygon, hence a hit. A partial confusion matrix can be constructed with 1) TP (true positives), number of hits, 2) FP (false positive), number of all classified fishponds minus the number of hits, 3) FN (false negative), number of all ground truth polygons minus the number of hits. Precision, Recall, and the F1 score can then be calculated. The equations to calculate the evaluation metrics were shown in Equation 2:

Equation 2. Accuracy assessment metrics for fishpond classification.

$$Prec = \frac{TP}{TP + FP}$$

$$Rec = \frac{TP}{TP + FN}$$

$$F1 = 2 \times \frac{Prec \times Rec}{Prec + Rec}$$

3.4. Results

3.4.1. Fishpond Classification Results

An LR classifier and a DT classifier were built using training samples. The classifiers were built and validated using a 5-fold cross-validation scheme. Specifically, the training dataset was split into 5 parts, and for each iteration, 4 of them were used as training set and the last one was used as validation set. To avoid building an overcomplicated DT classifier such that it is inconvenient to transplant the model on GEE and also to reduce overfitting, we limited the max depth of the DT to 3. Moreover, to further reduce overfitting, the minimum samples in the leaf node is set to 50. Table 5 shows the cross-validation results for both LR and DT. From the table we can see that DT generally performs slightly better than LR as the average training and validation scores of DT are both around 3-4% higher than LR. The training score and validation scores are close, which means the models are not overfitting. The weights of the trained LR model are shown in Table 6. The tree structure of the trained DT model is shown in Figure 7. From the figure, we can see that the leaf nodes of the left branch of the tree are all fishpond class, thus, the tree can be simplified by representing all leaf nodes on the left branch as one node with splitting criteria $SqP \leq 0.134$, which simplified the transplantation of the model on GEE**.**

Table 5. 5-fold cross validation score of implemented LR and DT models.

Iterations	LR		DT	
	Training score	Validation score	Training score	Validation score
1	0.824	0.827	0.858	0.840
2	0.819	0.839	0.866	0.850
3	0.819	**0.842**	0.856	**0.880**
4	0.831	0.791	0.870	0.847
5	0.825	0.816	0.869	0.839
Average	0.824	0.823	0.864	0.851

Table 6. Coefficients of OBFs using the optimal LR model

Intercept	**IPQ**	**SOLI**	**PFD**	**CONV**	**SqP**
-10.216	4.667	2.454	2.102	4.816	-3.552

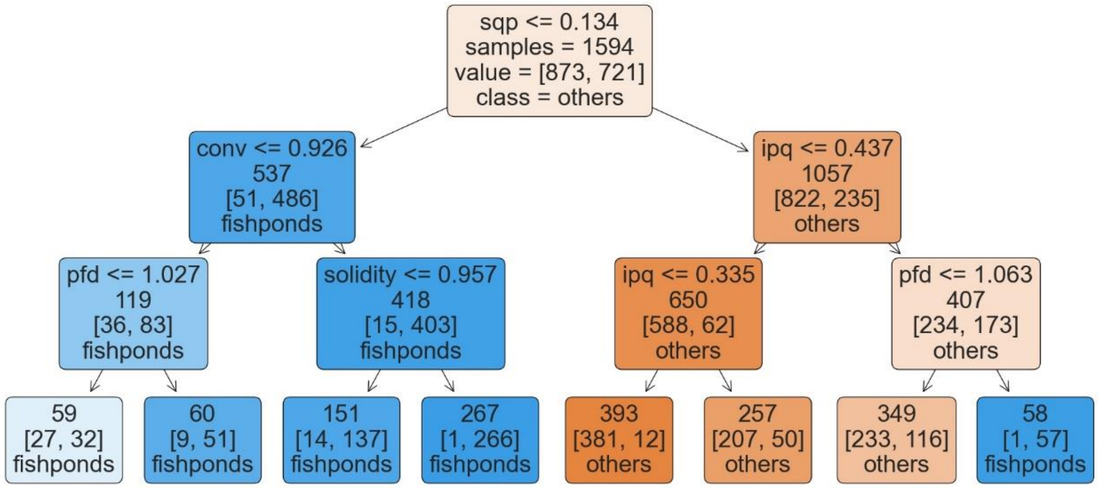

Figure 7. DT tree structure.
(In each node, from top to bottom, are the node-splitting criteria, the total number of samples in this node, the class distribution of the samples in this node, and the majority class of this node.)

Figure 8 shows fishpond classification results of three example subareas. The first subarea (left column) is a small village that contains densely located fishponds. By comparing the AWEI image in Figure 8(a) and the ground truth layer in Figure 8(d) we can see that the majority of fishpond boundaries are visually clear to identify while some fishponds are too close and small to identify individually. The second subarea (middle column) is a village with more scattered fishponds. Due to increased gaps between fishponds, their boundaries are easier to identify, and thus most of the fishponds are correctly identified. The third subarea (right column) is a village beside a river. As shown in Figure 8(i) and Figure 8(l), both LR and DT successfully rejected river body objects due to their elongated and concave shapes. For all three subareas, the results produced by LR (last row) is slightly better than DT (third row) because LR results have less false negatives such as the circled fishponds in Figure 8(g) – (l).

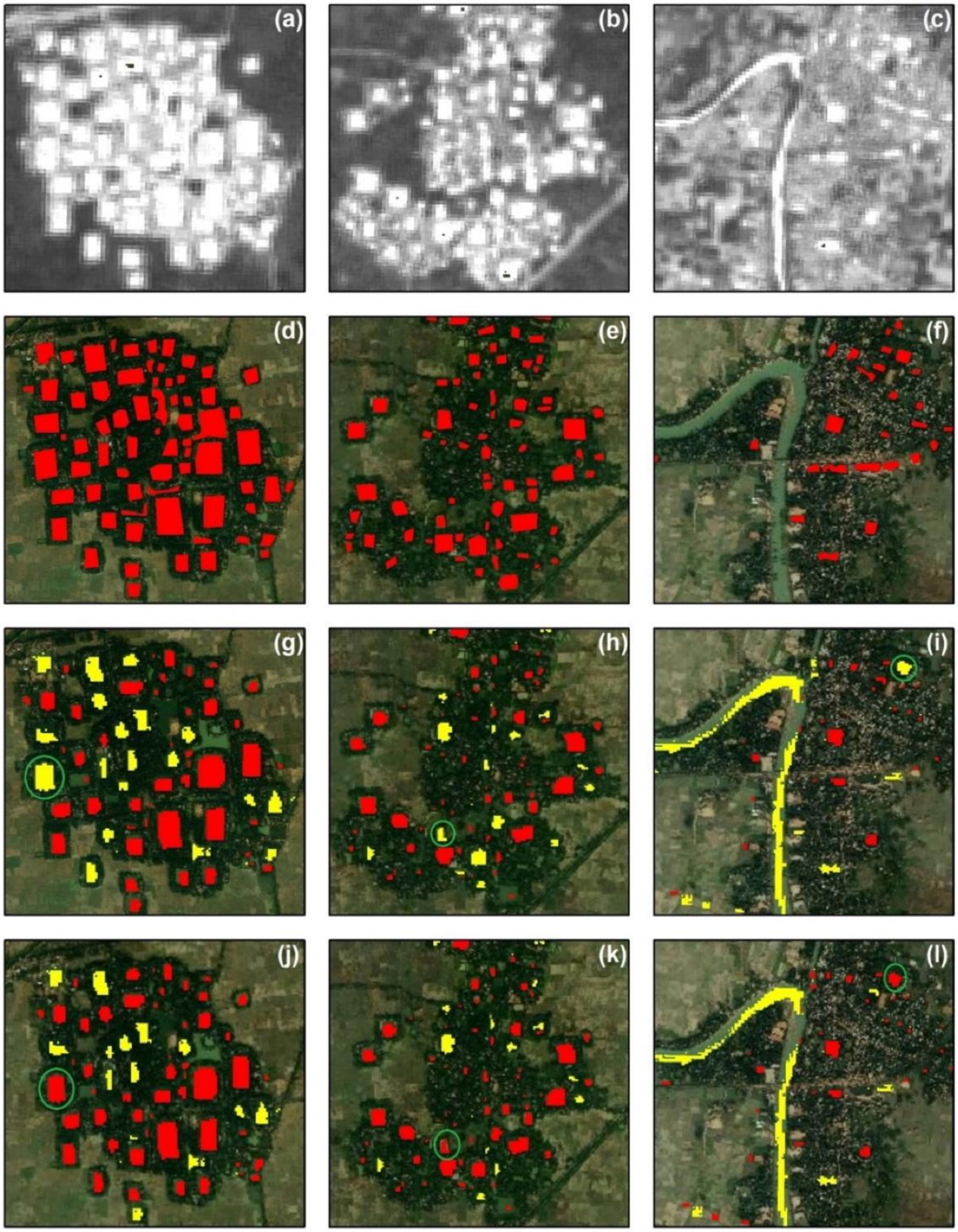

Figure 8. Fishpond classification results of three example subarea.
(Red polygons represent fishponds and yellow polygons represent water bodies identified by spectral filtering and rejected by spatial filtering. From top to bottom row: AWEI image on Apr 30th, ground truth data, classification results by DT, classification results by LR. Green circles in subfigure (g) – (l) highlights differences between results obtained from DT and LR.)

Figure 9 shows another village with a few irregular-shaped fishponds, e.g., the ‘L’ shaped fishpond on the left side of the region labeled as 1. Both LR and DT misclassified most of the fishponds in this region. Specifically, fishpond ‘1’ was misclassified because of its concave shape. As discussed in the methodology, OBFs are mostly designed to measure shape compactness and convexity, and the primary assumption of using OBFs to classify fishponds is that fishponds have relatively simpler shapes than other water objects. Fishpond ‘2’ is in fact a group of small fishponds according to the ground truth data shown in Figure 9(b). The overly small gaps between such small fishponds cannot be identified and thus they were recognized as one giant fishpond with complex shapes. Lastly, fishpond ‘3’ was misclassified due to its elongated shape. As a result, any small fluctuations on the longer side can significantly affect convex hull based OBFs such as SOLI and CONV. The misclassification of fishpond ‘2’ and ‘3’ indicate the huge influence of spatial resolution on the fishpond recognition. Fishponds are generally small, some of them are as small as 200 sq. meters, which is roughly 2 pixels on a Sentinel-2 image. The relatively coarse spatial resolution not only over-simplified boundaries of small fishponds but also amplifies the differences of OBFs caused by tiny changes to the shapes.

Figure 9. Examples of unsatisfactory classification results.
(Red polygons represent fishponds and yellow polygons represent water bodies identified by spectral filtering and rejected by spatial filtering. From left to right: AWEI image on Apr 30th, ground truth data, classification results by DT, classification results by LR.)

3.4.2. Evaluation

The proposed method was evaluated using the holdout testing dataset in 4 of the unions within the study area. The results are shown in Table 7. Specifically, the LR model identified in a total of 841 fishponds within the test unions, and the DT model identified 789 fishponds. Of all the classified fishponds, LR correctly classified 663 of the 841, the precision score is 0.788. DT correctly classified 610 of 789, the precision score is 0.773. As a comparison, the ground truth data contains in total 1232 fishponds within the test region. From the table, we can see that LR has dominantly better performance on the test dataset with all metric scores higher than DT even though DT performed better during training. The precision score of LR is 1.5% higher than DT, and the recall rate of LR is over 4% higher than DT. The overall F1 score of LR is 3.6% higher than DT. Therefore, LR is recommended to be implemented as the classifier for fishponds.

Table 7. Evaluation of LR and DT on the test dataset.

	LR	DT
# of 'hits' (TP)	663	610
# of classified fishponds	841	789
# of ground truth fishponds	1232	1232
Precision	**0.788**	0.773
Recall	**0.538**	0.495
F1 score	**0.640**	0.604

3.5. Discussion

3.5.1. Importance of the pixel selection technique

Figure 10 shows the comparison of histograms of WI values with and without pixel selection as well as optimal thresholds derived by the Otsu method. From the figure, we can see that most of the histograms show bimodal distributions. One peak on the high-value side indicates water types and the peak on the lower WI value side indicates other land cover types. Comparing thresholds derived using the Otsu method with and without pixel selection step, we can find that most threshold values are close such that whether to use pixel selection may not result in much difference. However, there are a few exceptions that the thresholds derived with pixel selection are quite different from that without. Specifically, thresholds derived with pixel selection on the NDWI image on Jan 1st and MNDWI and AWEI images on Apr 30th all fall out the valleys of the histograms, which significantly changes the class distributions of the segmented images. Figure 11 shows an example of such differences for the MNDWI image on Apr 30th. The figure clearly shows that the segmentation result with pixel selection is much better than without because the latter includes a lot of false positives, especially in the southwest region of the study area. Moreover, the boundaries of fishponds cannot be clearly identified due to the false positives as shown in the upper right subfigures. The pixel selection is especially effective when the target class is scarce that the difference between the target class and other classes is shadowed by variations within other classes. For example, the histograms of NDWI on Jan 1st and MNDWI on Apr 30th in Figure 10 show two peaks, and the Otsu method finds the threshold in the valley if no pixel selection is applied. However, such peaks just represent the internal variations of non-water types instead of between water class and non-water class. By applying the pixel selection technique, the number of non-water type pixels is significantly reduced to the same level as water features and thus produce better segmentation results. The thresholds derived using the Otsu method are shown in Table 8.

Table 8. Otsu method derived thresholds for WIs.
(Left column: with pixel selection; right column: without pixel selection. Threshold pairs that lead to significant differences in threshold results are highlighted.)

	NDWI		MNDWI		AWEI	
2016-01-01	**0.067**	**-0.141**	0.118	0.082	-0.148	-0.328
2016-01-31	-0.033	-0.052	0.235	0.243	0.100	0.132
2016-04-30	-0.165	-0.203	**-0.117**	**-0.269**	**-0.830**	**-1.172**
2016-10-17	-0.138	-0.078	0.162	0.242	0.216	0.520

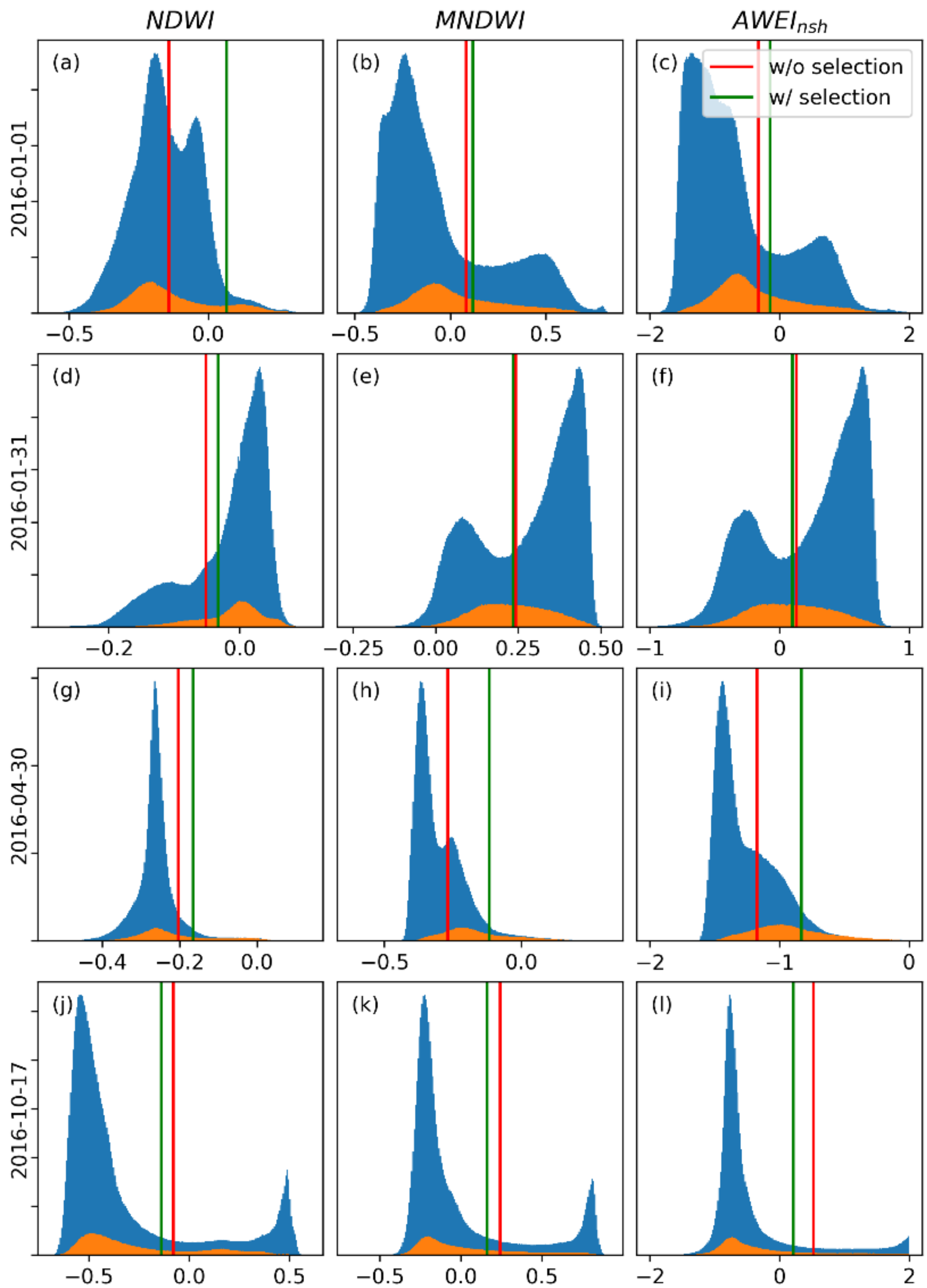

Figure 10. Histograms of WIs for four image dates within the study area.
(Blue histograms: without pixel selection technique; orange histograms: with pixel selection technique. Vertical lines represent thresholds found by the Otsu method for the two histograms.)

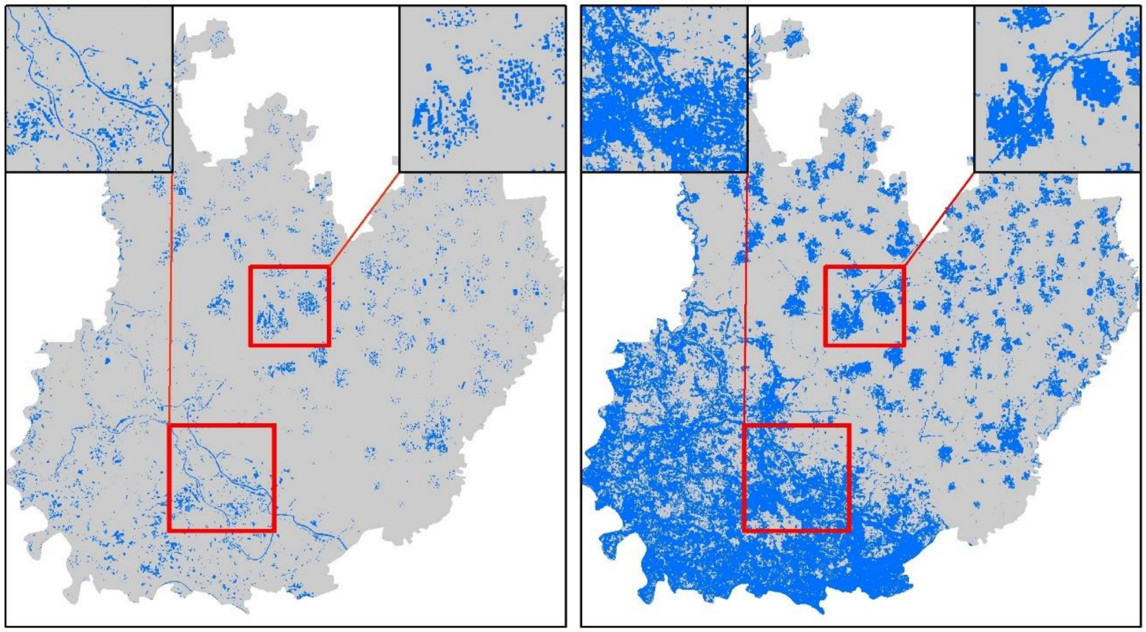

Figure 11. Comparison of water feature segmentation results for the MNDWI image on Apr 30th.
(Left side: with pixel selection technique; right side: without pixel selection technique.)

3.5.2. Object-Based Features

Five OBFs, i.e., IPQ, SOLI, PFD, CONV, and SqP were calculated for all vectorized all-year flooded water features. Figure 12 shows the paired scatter plot of OBF values of training data samples. Specifically, the diagonal subfigures show the distribution of each OBF values for fishponds and non-fishpond types, and the off-diagonal subfigures show the scattered points on the 2D space of the corresponding OBF features. From the diagonal subfigures, we can see that IPQ, CONV, and SqP provide good class separability because the peaks of distributions are well separated while the distributions of SOLI and PFD have a lot of overlap. From the most upper-right subplot, we can also see that SqP and IPQ show a near quadratic relationship as all points align on a simple curve. This can be proved using the formula of the two features. From all subfigures, the most likely feature pairs that may provide linear separability is the pair of PFD and SqP because the positive samples and negative samples roughly align along the opposite sides of the $y = x$ line visually. Other pairs of features do not show clear separability between the two classes.

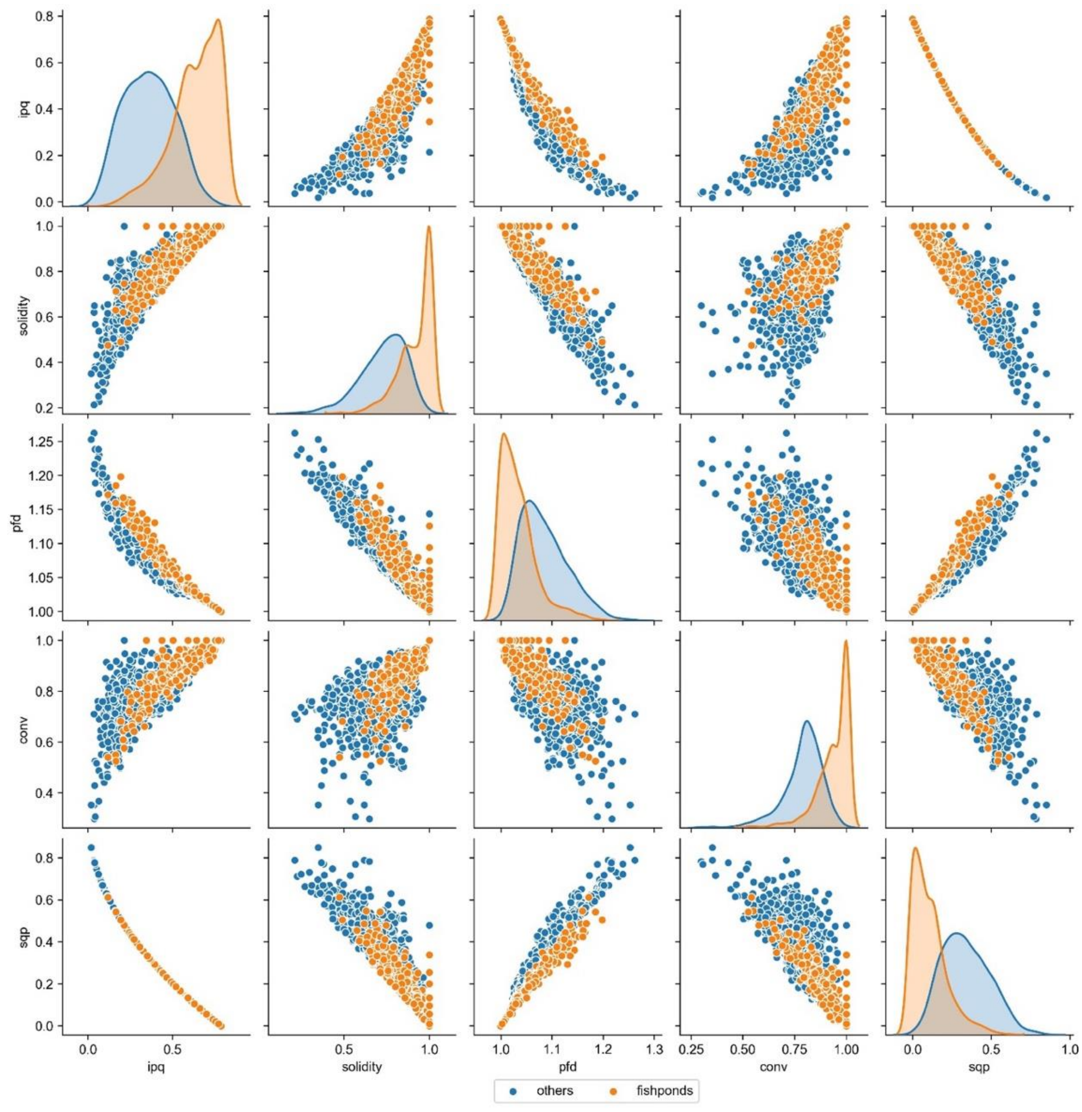

Figure 12. Paired scatter plots of OBFs.
(Diagonal plots are histograms of each OBF for fishpond and non-fishpond classes. Off-diagonal plots are scatter plots of corresponding feature pairs of fishponds and non-fishponds samples.)

3.5.3. Limitations and future work

The major limitation of the work is that the spatial resolution of Sentinel-2 images is not high enough to map extremely small-scale fishponds. A great portion of the inland fishponds are only a few pixels large, and the pixel outlines certainly cannot accurately represent the true shape of these fishponds. However, Sentinel-2 is currently the only operational optical satellite that provides continuous and high-resolution multi-spectral data free of charges. Thus, until new missions are launched, 10 m resolution is the best spatial resolution for long-term and continuous mapping of inland fishponds. Another limitation is that cloud covers in monsoon seasons limited the number of images that can be used. Thus, a few previous research works use Synthetic Aperture Radar (SAR) images instead of optical images for aquaculture pond mapping in SA (Ottinger et al., 2017; Prasad et al., 2019). As SAR uses microwave spectrum that can penetrate clouds, and it does not rely on the presence of sun, it can provide significantly better temporal coverage for regions with heavy cloud contaminations. Moreover, water features have very low backscatter comparing with other LULC types such that they stand out on SAR images. However, SAR images are generally contaminated with speckle noises that needs to be preprocessed by filtering, which will somewhat reduce the spatial resolution of the product, and edges may not be preserved. The reduced spatial resolution may not affect large objects mapping such as coastal aquaculture ponds, it may have a major impact on the performance of mapping small-scale inland fishponds. Recent research showed that the integrative usage of optical and SAR sensors, especially Sentinel-1 and Sentinel-2, has great potential in LULC mapping in monsoon area (Steinhausen et al., 2018), and this is a very promising direction of improving the current state of inland fishpond mapping.

3.6. Conclusion

Inland fishery is growing fast in Bangladesh and many other SA countries such as India. The underlying LULC change, especially the transition of agriculture land to aquaculture land may put pressure on already limited agriculture land for large populations. Mapping and monitoring inland fishponds are essential to understand such LULC change. While there are many research works focus on mapping coastal aquaculture ponds, there is little research effort that focus on mapping inland fishponds which are typically small and cluttered. Thus, this chapter presents a GEE-based workflow that uses multi-temporal Sentinel-2 images for fishpond mapping in the context of a case study in the Singra Upazila in Bangladesh. The workflow first applies a spectral-based filtering that automatically segments multi-temporal images using WIs and generates an all-year-flooded water feature mask. A key step in the spectral filtering is to apply a pixel selection technique that limit number of pixels used in image segmentation, which is essential to map small objects in a large area. Then a spatial-based filtering was applied to classify all-year-flooded water objects into fishponds and non-fishponds using OBFs. We used five OBFs to characterize water objects and trained a LR and a DT model using the five OBFs as features. The LR model achieved better results than DT, and the trained LR model was used in the workflow for final classification. In a case study in the Singra Upazila in Bangladesh, we manually digitized fishponds using Google Earth historical images and tested our method. The proposed workflow achieved around

79% precision and 54% recall rate. Lastly, the workflow was implemented on GEE and thus can be easily reapplied to new regions. This work demonstrated the use of GEE for general remote sensing research.

This chapter is a slightly modified version of Yu et al. (2020) and has been reproduced here with the permission of the publisher, i.e., MDPI, and the copyright holder, i.e., Zhiqi Yu.

4. CROP INTENSITY MAPPING WITH REMOTE SENSING DATA

4.1. Background

SA that mainly includes Bangladesh, India, Nepal, Bhutan, Pakistan, and Sri Lanka, is one of the most intensively farmed regions in the world (Gray et al., 2014). The entire region accounts for almost 40% of the world's harvested rice area, and Bangladesh specifically, is the fourth largest rice producing country in the world (Gumma, 2011). The ever-growing population and limited lands arable and available for farming all poses severe challenges to the global food security (HAO et al., 2019). According to Gray et al. (2014), nearly 95% of SA land suitable for rain-fed agriculture was under cultivation in 1992, which leaves it very little room for cropland expansion. Thus, to produce more food for the growing population, and accounts for the changing diet, the agriculture intensification, i.e., increasing the number of crop planting cycles within a year, is expected (Qiu et al., 2016). According to a projection, the world's agricultural production needs to increase 70% - 110% to account for the increasing population from 2010 to 2050. However, increasing cropping cycles within a year may bring environmental issues such as degraded soil quality, water pollution, forest degradation, and climate change (L. Liu et al., 2020b; Qiu et al., 2016). Thus, timely update of large-scale cropping intensity information is crucial for understanding food production and environmental monitoring (L. Liu et al., 2020b; Qiu et al., 2016).

Crop intensity is defined as the number of cropping cycles planted per year (Gray et al., 2014; Tatsumi, 2016; M. Zhang et al., 2021). Mapping crop intensity using remote sensing data is an extensively explored area. Satellite sensors can provide large-scale observations at mid to fine spatial resolution every few days, which is ideal for monitoring crops at national and continental scale. Numerous research works have explored using various datasets and different modelling methods for crop intensity mapping. Hao et al. (2019) used harmonized Landsat and Sentinel-2 dataset and modelled the time-series NDVI and EVI using sixth degree polynomial function. They identified cropping intensity from the modelled NDVI and EVI curves by counting the number of valid peaks in the curves, and they tested the method at four study sites located in North America, South Africa, SA, and East Asia (HAO et al., 2019). Qiu et al. (2016) used a modified Isolines of Wavelet Spectra method to automatically classify crop intensity using Moderate Resolution Imaging Spectroradiometer (MODIS) EVI time-series datasets in Hunan province in China. Their result was compared with in-situ data, and the overall accuracy is at 88.9%. Gray et al. (2014) also used a method based on the MODIS land cover product, which involves curve smoothing using a Loess filter and heuristic filtering. They also used the total number of valid peaks in the time-series as the representation of cropping intensity. Their method was applied to the entire Asia region and was compared with national inventory statistics. Zhang et al. (2021) produced the GCI30 global 30m cropping intensity dataset using mainly Landsat data. They derived NDVI, EVI, and LSWI and detected cropping intensity for non-rice croplands and flooded paddy rice separately. In a broader context, cropping intensity detection is a specific application of phenology modelling and detection using satellite images. There are many methods that have been applied to detecting crop phenology phases and seasonalities based on model-fitting with time-series data. Sakamoto et al. (2005) explored using wavelet and Fourier functions to fit time-series MODIS EVI data to detect crop phenology. Jönsson and Eklundh (2002) used an asymmetric Gaussian model to fit Advanded Very High-Resolution Radiometer (AVHRR) NDVI time series over Africa.

Despite that abundant research on crop intensity mapping and crop phenology detection using various dataset and method, a knowledge gap remains to be explored using harmonic regression model for crop intensity mapping in Bangladesh where cloud cover is persistent during monsoon seasons. Thus, this research aims to explore using Harmonic regression and MODIS surface reflectance product for crop intensity mapping.

4.2. Study Area

Bangladesh is one of the most populous and densely populated countries in the whole world. It is also one of the poorest countries in the world. Around 57% of its total land is arable, 45% of its population conduct agricultural activities for living, and agriculture takes up 16% of its GDP (Nasim et al., 2018). The climate system in Bangladesh is mainly in the sub-tropical monsoon climate system which is characterized by the uneven distribution of temperature and rainfall (Nasim et al., 2018). During monsoon seasons, temperatures are high, and precipitations are high. In the winter however, the temperature is low, and weather is dry but sunny. Adapting to this climate system, Bangladesh mainly has two crop planting seasons, namely Kharif season and Rabi season (Mohsenipour et al., 2018). The Kharif season extends from May to

November, which is humid and hot, and the Rabi season extends from December to April, which is dry and cold. Rainfed Aman rice is mainly grown in the Kharif season and irrigated Boro rice is grown in the Rabi season. The Kharif season may further divide into two smaller seasons, one from mid-March to mid-July, and the other from mid-July to mid-November.

4.3. Method

4.3.1. Datasets

The remote sensing data that is used in this research is the MODIS Terra/Aqua Surface Reflectance product 8-day Global 250m. The data products are hosted on the GEE cloud servers and are accessed through GEE JavaScript API using GEE online script editor. This research selected all available images between Jan 1st 2010 and Jan 1st 2011. Because the dataset has a temporal resolution of 8 days, there are in total 46 images available within one year. Thus, the total number of images that were used in this research is 92 with 46 from MODIS Terra Surface Reflectance product and the other 46 from MODIS Aqua Surface Reflectance product.

Aside from remote sensing data, this research also uses the administrative boundaries of Bangladesh at the country level and at district level. The country level is used to clip MODIS images to the extent of study area and the district level boundaries are used to calculate per-district crop intensity to compare with district-level cropping intensity data from Bangladesh Bureau of Statistics (BBS).

4.3.2. Preprocessing

The MODIS Surface Reflectance data is preprocessed before used for analysis. The preprocessing mainly includes four steps, first is to use the ‘State’ band from the MODIS surface reflectance product to mask cloud pixels, second is to clip the selected images using the boundary of our study area, and the third is to combine Terra and Aqua MODIS Surface Reflectance product as one dataset, lastly, we compute the NDVI for all the surface reflectance images.

The first two bits from the ‘State’ band of the MODIS surface reflectance images are dedicated to cloud state, thus, a bitwise ‘and’ operation was conducted on the ‘State’ band to extract the cloud mask. Each of the MODIS images derive a cloud mask individually. The boundary of the Bangladesh country was used to clip all to the extent of the study area. The MODIS Terra/Aqua Surface Reflectance data on the GEE is itself a composite dataset that covers the entire globe, which means that no mosaicking is needed. The third step uses a simple heuristic to combine Terra and Aqua MODIS Surface Reflectance product. As discussed before, Bangladesh has a sub-tropical monsoon climate system, and during the monsoon season, the persistent cloud cover prevents optical sensors like MODIS to observe the ground. The combination of Terra and Aqua may mitigate the problem. Specifically, the heuristic is that since Terra and Aqua passes the same location at same day in the morning and afternoon respectively, during this few hours’ time period, the crop condition can be treated as the same. Thus, we can assume that the only difference between Terra and Aqua MODIS Surface Reflectance for the same day is the cloud cover because the cloud may present in morning but not in the afternoon, and vice versa. The mathematical representation of this step is shown in Equation 3:

Equation 3. Simple combination of MODIS Terra and Aqua Surface Reflectance products.

$$\mathrm{V_{combined}} = \begin{cases} \mathrm{reduce}(V_{Terra}, V_{Aqua}), & if\ V_{Terra}, V_{Aqua} \neq NaN \\ V_{Terra} \mid V_{Aqua}, & if\ V_{Terra} \text{ or } V_{Aqua} = NaN \\ NaN, & if\ V_{Terra} \text{ and } V_{Aqua} = NaN \end{cases}$$

Where the V_{Terra} and V_{Aqua} are surface reflectance values for Terra and Aqua respectively, and NaN indicate that this pixel is masked because of clouds. The $reduce()$ function can be any function that combines the two values from Aqua and Terra, e.g., mean value, max value, etc. In this research, since we are computing NDVI, we used maximum function because most NDVI composite product uses maximum functions.

The last step is to compute NDVI from surface reflectance. The NDVI is calculated as Equation 4:

Equation 4. NDVI

$$NDVI = \frac{\rho_{NIR} - \rho_{Red}}{\rho_{NIR} + \rho_{Red}}$$

Where ρ_{NIR} is the surface reflectance in near infrared band, which is band 2 in MODIS, and ρ_{Red} is the surface reflectance in the red band, which is band 1 in MODIS.

4.3.3. Harmonic Regression

Similar to other cropping intensity mapping research, this research detects the cropping cycles based on crop phenology (Gray et al., 2014; HAO et al., 2019; Jain et al., 2013; L. Li et al., 2014; L. Liu et al., 2020b; Tatsumi, 2016; M. Zhang et al., 2021). At the beginning of a crop season, there are little vegetation cover, which associates with low NDVI values. If the crop is rice, the fields will be filled with water during the transplanting phase, which also yields low NDVI values (Dong et al., 2016). As crop grows, the greenness and biomass increases, which can attribute to the increase of NDVI during this period. After the greenness of crops reach the maximum and become mature, the harvesting will happen, which decreases the biomass and expose more bare soil, thus the NDVI values decreases during this time (Huang et al., 2019). Thus, the NDVI values of one cropping cycle should show a ‘bell’ shape. There are many research works that identify the start-of-season (SOS) and end-of-season (EOS) to detect a crop season (Huang et al., 2019; Whitcraft et al., 2015). One simple method to detect such ‘bell’ shape is using thresholds on the NDVI curves. The SOS and EOS happens when the NDVI curve crosses the threshold lines (Huang et al., 2019). This research uses a variation of this method, which is simpler and easy to implement on GEE. Specifically, a single threshold that is between the valleys of the NDVI curve, which signals SOS and EOS, and the peak of NDVI curve, was set. The number of cropping cycles were calculated by counting how many times the NDVI curve crosses the threshold line. As a valid cropping season should start and end lower than the threshold, and the peak should be higher than the threshold, a cropping season should cross the threshold line exactly twice. Thus, the number of times that crosses the threshold line divide by 2 should be the number of cropping cycles.

Harmonic Regression, also called Harmonic Analysis of Time Series (HANTS) (Roerink et al., 2000; J. Zhou et al., 2012, 2015), is a technique that uses Fourier series, i.e., sine and cosine series of different frequencies as base to model the input signal. It is a very popular method in curve smoothing and gap filling for time series remote sensing data analysis. Many research works use HANTS to reconstruct NDVI time series with missing data (Malamiri et al., 2020; Roerink et al., 2000; J. Zhou et al., 2015). The mathematical representation of the harmonic regression is shown in Equation 5:

Equation 5. Harmonic Regression

$$V(t) = a_0 + \sum_{i=1}^{n}\left(a_i cos(2\pi it) + b_i sin(2\pi it)\right), t = \frac{DoY}{\#days}$$

Where t is the ratio between the DoY (day of year) and the number of days in the given year, thus it is between 0 and 1. n is the number of Fourier series that is chosen for the model, the higher the n, the more variations in the original data can be captured in the fitted model. In this study, n is chosen to be 3.

For each pixel, the 46 values corresponding to each time stamp in the year 2010 were used to fit the model. Then we used 0.5 as the threshold to find the number of crossings between the threshold and the fitted curve. The 0.5 is used according to Hao et al. (2019).

4.4. Results

Figure 13 shows the crop intensity map derived from this research. The map shows four classes, single cropped land, double cropped land, triple cropped land, and other land cover land use classes shown as background color. we can see that the dominant crop intensity in Bangladesh is two seasons, followed by one season. Three seasons are relatively rare. As we can see from the result, the main area that conduct single season cropping is the northern east part of Bangladesh, some coastal area, and small areas in the west. The northern east part of Bangladesh that is at around 91-degree east, 24 to 25 degree north is the Haor region, which is a wetland ecosystem that is completely flooded by the runoff water from rivers and canals during monsoon seasons. After the monsoon season and the surface water dry up, a season of rice is generally grown in the Rabi season utilizing the remaining moisture in the soil and the help from irrigation (Alam et al., 2010). Our method successfully identified the Haor region as single cropped land. Most of the cropland in Bangladesh is conducting double season cropping as expected. It is the most common cropping system in Bangladesh with one Kharif season for rainfed rice, and a Rabi season for irrigated rice or wheat. Triple cropped area is mainly distributed in the central region and some small area in the northern western part of Bangladesh.

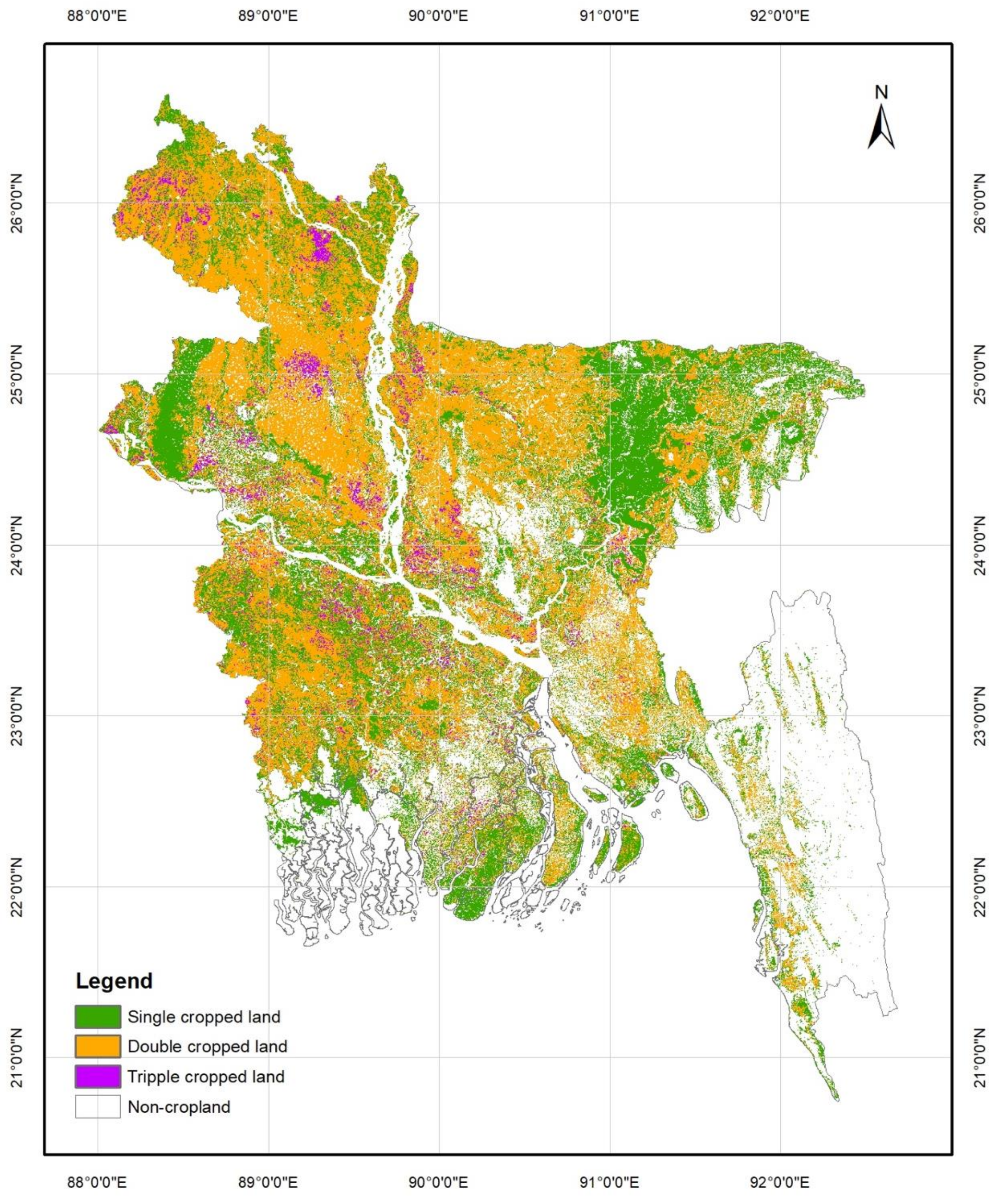

Figure 13. The crop intensity results derived by our method.

Table 9 shows the comparison between the statistics derived from remote sensing-based method and the statistics published by BBS for 2010. BBS publishes national statistics that cover many aspects including forestry, agriculture, land use and land cover, etc. every a few years. From the table we can see that the remote sensing-derived crop intensity is generally lower than the statistics. For example, the Khagrachhari district shows 1.45 cropping intensity from our method while the official statistic shows 2.12, which means the overall cropping pattern for this district is double cropping while our result shows less than double cropping. The underestimation can also be seen in the national summary, where our method shows the overall cropping intensity for Bangladesh is 1.655 while the official statistics show 1.91.

Table 9. District and region-wise crop intensity summary from our result and statistics from BBS

Region Name	District Name	Crop Intensity by our method	Crop Intensity from BBS
Bandarban	Bandarban	1.157534	1.38
Barisal	Barisal	1.72627	1.76
	Bhola	1.543641	
	Jhalokathi	1.680704	
	Pirojpur	1.617375	
Bogra	Bogra	1.980268	2.35
	Joypurhat	1.301246	
Chittagong	Chittagong	1.599386	1.99
	Cox's Bazar	1.702732	
Khagrachhari	Khagrachhari	1.456341	2.12
Rangamati	Rangamati	1.276831	1.44
Comilla	Brahmanbaria	1.560693	1.82
	Chandpur	1.719748	
	Comilla	1.490053	
Dhaka	Dhaka	1.874435	1.72
	Gazipur	1.712432	
	Manikganj	1.345053	
	Munshiganj	1.831956	
	Narayanganj	1.436767	

	Narsingdi	1.765473	
Dinajpur	Dinajpur	1.661731	2.11
	Panchogarh	1.598903	
	Thakurgaon	1.997417	
Faridpur	Faridpur	1.618574	1.92
	Gopalganj	1.458369	
	Madaripur	1.725696	
	Rajbari	1.693322	
	Shariatpur	1.624316	
Jamalpur	Jamalpur	1.772047	2.29
	Sherpur	1.847076	
Jessore	Jessore	1.653473	2.28
	Jhenaidah	1.937731	
	Magura	1.845971	
	Narail	1.637942	
Khulna	Bagerhat	1.49646	1.34
	Khulna	1.267695	
	Satkhira	1.572612	
Kushtia	Chuadanga	1.855318	2.56
	Kushtia	1.60264	
	Meherpur	1.842816	
Mymensingh	Kishoreganj	1.579946	2.15
	Mymensingh	1.642374	
	Netrokona	1.600508	
Noakhali	Feni	1.823093	2.11
	Lakshmipur	1.681078	
	Noakhali	1.538954	
Pabna	Pabna	1.573781	2.03
	Sirajganj	1.912778	
Patuakhali	Barguna	1.399497	1.49
	Patuakhali	1.346188	
Rajshahi	Chapai Nawabganj	1.529636	1.80
	Naogaon	1.64282	
	Natore	1.461503	
	Rajshahi	1.602412	
Rangpur	Gaibandha	1.613909	2.02
	Kurigram	1.706694	
	Lalmonirhat	1.697256	
	Nilphamari	1.723727	
	Rangpur	1.854516	
Sylhet	Habiganj	1.920637	1.54
	Maulvibazar	1.667063	
	Sunamganj	1.290713	
	Sylhet	1.308794	
Tangail	Tangail	1.848917	1.92
Summary		**1.655**	**1.91**

4.5. Discussion

We believe the main reason why our method is underestimating cropping intensity is because we used only first 3 Fourier series in the harmonic regression, which caused the fitted model to be underfitting. Figure 14 shows examples of NDVI time-series for single cropped land, double cropped land, and triple cropped land, and the fitted curve using harmonic regression with first 3 Fourier series. As we can see, for single cropping cycle and double cropping cycles, the model fits well with the original data. However, the fitted curve for triple cropping cycle shows some underfitting, especially at the end of the second season at around 210 DoY where the curve should be expected to drop lower but instead, it only drops a little and climbs back up for the third season. Because of that, the detected cropping cycles may not include the second one simply because the valley point is higher than the threshold. Thus, a future direction to improve this work is to use more than 3 Fourier series for model fitting.

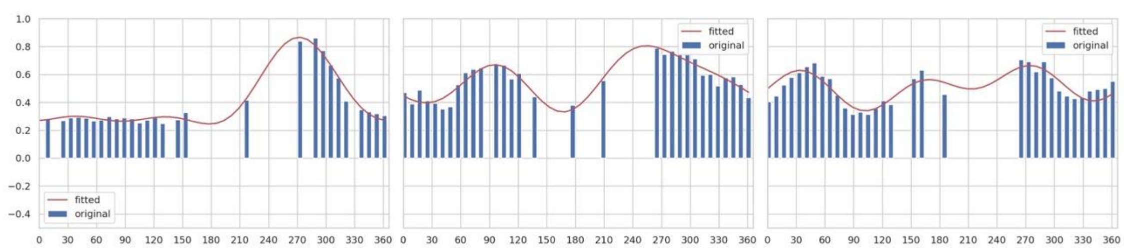

Figure 14. Example NDVI time-series and fitted curves for single cropping cycle (left), double cropping cycle (middle), and triple cropping cycle (right).

Another reason for the underestimation is that the majority of the time-series have large portion of missing values due to cloud cover in the monsoon season. Gray et al. (2014) reported that they also experienced difficulties detecting more than two cropping cycles in a year due to missing value problems.

Another issue with the current method is that the threshold 0.5 is chosen empirically. If ground truth data are available, the threshold can be derived statistically to maximize the performance on the ground truth data, and then apply it for the mapping, which should be more robust than applying thresholds empirically.

4.6. Conclusion

This chapter explored using MODIS Surface Reflectance product on GEE for crop intensity mapping in Bangladesh for 2010. To overcome the missing value problem caused by the persistent cloud cover during the monsoon season, we first did a combination of MODIS Terra and Aqua Surface Reflectance products, and then we applied the harmonic regression to reconstruct smooth and gap filled NDVI curves. Lastly, an empirical threshold 0.5 was used for crop intensity detection. The result showed that the spatial distribution of cropping intensity generally matches with the expected cropping intensity in Bangladesh. The average cropping intensity derived using this method is underestimating the actual average cropping intensity according to the statistics from BBS. Our method indicates the overall cropping intensity is 1.655 while the official statistics shows 1.91. The main reason for this underestimation is still the missing value problem. When the majority of a cropping season is under the influence of cloud cover, it is very hard to reconstruct.

5. RICE MAPPING WITH GEE-BASED WEB APPLICATION

5.1. Introduction

Rice is one of the most important food sources that feed more than half of the global population (Ni et al., 2021b). Paddy rice area accounts for nearly 11% of overall cropland area globally (Xiao et al., 2006). Rice cultivation is especially popular in SA and Southeast Asia (SEA) due to ample rainfall and warm temperatures. It is the dominant crop type in many agrarian SA and SEA countries such as Bangladesh, Nepal, and Vietnam. According to International Rice Research Institute, paddy rice fields in SEA along accounts for almost 30% of the world rice harvest. Thus, rice farming in SA and SEA is important to the regional and global food security, which is a pivotal theme in United Nation’s 17 Sustainable Development Goals (SDG). Decision makers and planners depend on timely reported information on paddy rice area and vegetation growth to estimate rice yields and plan resource allocations and contingency plans accordingly. Thus, timely producing accurate rice extent maps is crucial for helping the formulation of strategic agricultural plans that ensures food security, especially for densely populated countries like Bangladesh, India, and Vietnam (Rimal et al., 2018).

Remote sensing datasets including both optical multi-spectral sensors, e.g., Moderate Resolution Imaging Spectro-radiometer (MODIS), Landsat, and Sentinel-2, and radar sensors, e.g., RADARSAT and Sentinel-1 have long been used in rice mapping (Dong et al., 2016; Inoue et al., 2020; Onojeghuo et al., 2018). Dong et al. (2016) summarized three categories of methods that are generally used by previous research in mapping rice using remote sensing images. The first category is to use statistical approaches like supervised learning and unsupervised classification on images from certain stages of rice planting. For example, Onojeghuo et al. (2018) combined NDVI time-series during the rice growing period derived using Landsat images and polarization bands, i.e., VV and VH from Sentinel-1A images, and used supervised classification models including Support Vector Machine (SVM) and Random Forest (RF) to classify paddy rice fields in northeastern China. Their best results were from using time-series VH and NDVI with RF, which yields a 96.7% accuracy. Chen et al. (2020) trained multiple RF models using combinations of all polarization bands from Sentinel-1 and NDVI, LSWI, and EVI derived from Sentinel-2 for paddy rice classification. Their results showed that best accuracy is achieved with the combination of VV, VH, and EVI. The second category is to use time-series data and threshold-based segmentation methods, and the last category is by detecting the transplanting phase, during which the fields are flooded. Vegetation index like NDVI or water indices like Land Surface Water Index (LSWI) or Modified Normalized Difference Water Index (MNDWI) can be used during this phase to detect water in the fields. This distinct phase of paddy rice phenology is widely used in previous research. Xiao et al. (2005b) classified paddy rice in southern China by comparing LSWI and NDVI during the transplanting phase till the full canopy exists. Their assumption was that during the transplanting phase, LSWI will be greater than NDVI (Xiao et al., 2005b). They further revised the algorithm by adding EVI into the comparison and relaxed the decision margin from LSWI greater than NDVI to LSWI + 0.05 greater than NDVI or EVI (Xiao et al., 2006).

Previous research has demonstrated that paddy rice classification by detecting the transplanting phase or by supervised classification with time-series remote sensing data can yield satisfactory results. Web-based applications that uses GEE APIs can effectively reduce the barrier of JavaScript programming and offer remote sensing data processing workflows to a wider range of people. While there are web applications like O-LCMapping and REMAP that allow general land cover classification, which may be used for rice mapping, there are certain challenges that need to be addressed for rice mapping. Specifically, collecting ground truth samples for rice just by inspecting high resolution true color images like Google Earth Satellite layers is not adequate because different crop types cannot be differentiated on true color images. Thus, this research aims to address this issue by developing a web application, which we named RiceMapEngine, that allows users to refine ground truth samples based on their phenology information. The RiceMapEngine will utilize the computing power and data catalog of GEE for fast paddy rice mapping by supervised classification or phenology-based approach.

5.2. Methods

5.2.1. Software Design

The RiceMapEngine is designed as a modern single-page web application (SPA). A SPA is an application that loads entirely when it opens. It differs from a traditional server-rendering web application, e.g., a Tethys-based web application, which dynamically renders webpages at the server-side throughout the entire life cycle of the web application. We believe SPA suits the design of RiceMapEngine better because of several reasons:

1) SPA is more suitable for complex interactions between users and the application, such as uploading/modifying ground truth samples, and going back and forth between each stage of crop mapping, etc.
2) GEE requests can take seconds or even minutes to respond, which is not user friendly. Thus, RiceMapEngine tries to reduce the number of calls to the backend GEE APIs as much as possible. A powerful SPA frontend can alleviate the load of backend.
3) SPA develops UI as reusable components, which is more suitable for open source.

The overall software architecture is illustrated in Figure 15. The frontend shows the map component and controls for user input, and the backend essentially serves as a proxy that translate requests from frontend into GEE Python API calls. The entire application is organized as 3 different apps, namely, phenology explorer, empirical thresholding, and supervised classification. Each of these apps represents a stage of the crop mapping process.

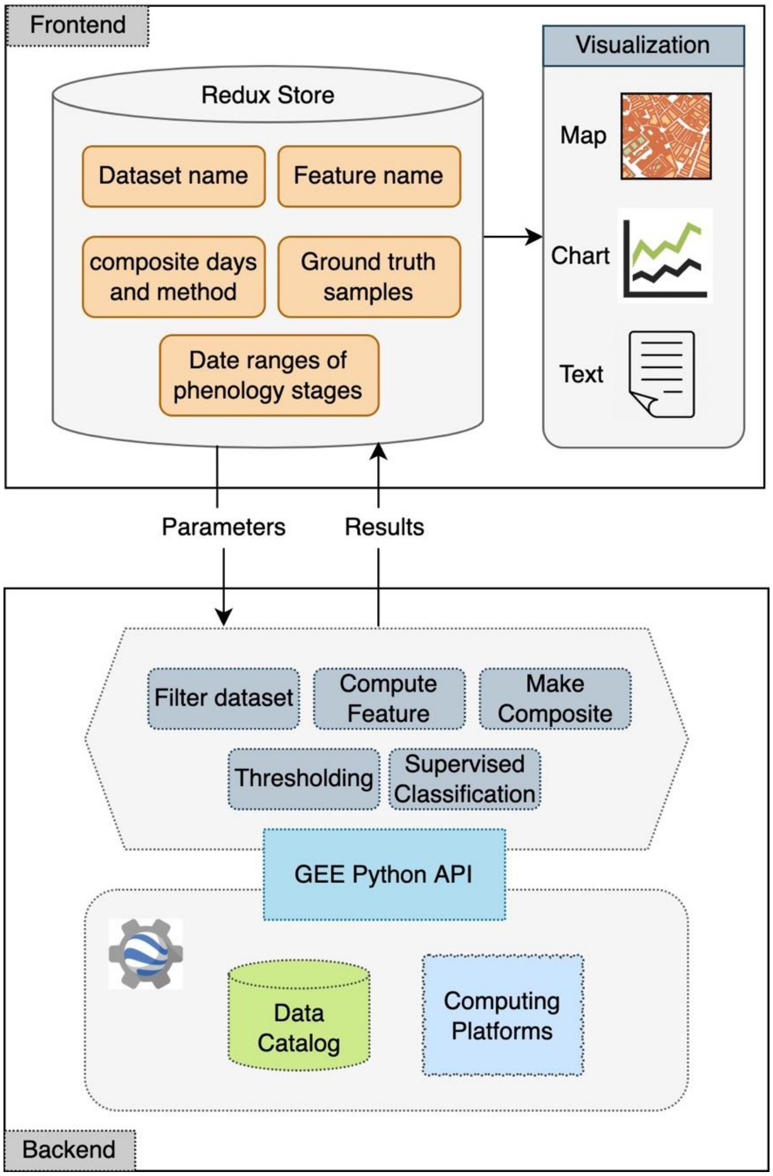

Figure 15. Overall architecture of RiceMapEngine.

On the frontend side, the three apps are organized behind client-side routing. SPA and client-side routing enables these apps to share commonly used components like header, map, and footer, and only reload necessary parts of the pages depending on the current URL, which is extremely helpful when the web map component needs to be shared across all apps. A redux store is used to hold states and data of current user session, e.g., user-selected dataset name, image date range, user-uploaded ground truth samples, etc. This model-view-like structure is very friendly to open-source because a new application can be easily added to the entire application by adding a client-side-route and a new redux store slice.

To facilitate the use of SPA for frontend design, the backend of the application is developed as an API server using Django framework in Python. The backend uses a Google Service Account to authenticate all GEE requests for the application as the application starts up. The Google Service Account associates GEE requests to the account itself, rather than an end user, which is recommended for developing applications or RESTful APIs. As the heart of the backend, a suite of frequently used functions for data processing, such as selecting and filtering datasets on GEE, and computing features, is implemented using GEE Python APIs. These functions are implemented to be as generic as possible in order to handle a range of possible inputs. For example, the compute_feature function dynamically selects the formula and bands for computation according to the input satellite name and the feature name as the function arguments.

5.2.2. Core Functions

5.2.2.1. Dataset Filtering

As satellite datasets on GEE are organized as *ee.ImageCollection* objects, the first step of using remote sensing datasets from GEE is often applying filters to select the relevant portion of the dataset. Apart from filtering datasets by the date range and the study area, additional filters can be applied to different datasets, e.g., maximum cloud cover, descending and/or ascending orbit, etc. RiceMapEngine allows users to select a range of publicly available satellite datasets including both passive optical sensors and active radar sensors. Table 10 lists all the datasets that are included in the RiceMapEngine application. For optical datasets, the application allows users to specify the maximum percentage of cloud cover for the image without looking up the specific property from the metadata of the dataset. For radar dataset, i.e., Sentinel-1 SAR dataset, a default interferometric wide (IW) swath mode filter is applied, and users can select to include images in descending and/or ascending orbit.

Table 10. GEE datasets that are available in RiceMapEngine.

Dataset Name	**GEE Asset ID**	**Features**
Sentinel-1 SAR GRD: C-band	COPERNICUS/S1_GRD	VH, VV, CR, RVI
MOD13Q1.006 Terra Vegetation Indices 16-Day Global 250m	MODIS/006/MOD13Q1	NDVI, EVI
USGS Landsat 5 TM Collection 1 Tier 1 TOA Reflectance	LANDSAT/LT05/C01/T1_TOA	NDVI, EVI, NDWI, MNDWI
USGS Landsat 8 Collection 1 Tier 1 TOA Reflectance	LANDSAT/LC08/C01/T1_TOA	NDVI, EVI, NDWI, MNDWI
Sentinel-2 MSI: MultiSpectral Instrument, Level-1C	COPERNICUS/S2	NDVI, EVI, NDWI, MNDWI

5.2.2.2. Preprocessing

The preprocessing module mainly include three functions, computing an index-like feature, make composite, and speckle filtering for SAR data.

The RiceMapEngine uses the concept of ‘feature’ to denote a single indicator for time-series analysis, and classification. The feature can be either a single band, such as the VH polarization band from Sentinel-1, or a computed value using multiple bands, such as NDVI. For optical sensors, the RiceMapEngine provides two most popular vegetation indices, NDVI and EVI, and two commonly used water indices, namely Normalized Difference Water Index (NDWI), and Modified Normalized Difference Water Index (MNDWI). NDVI is the most popular vegetation index for measuring biomass. Enhanced Vegetation Index (EVI) is a more advanced vegetation index because it addressed some atmospheric conditions and canopy background noise problems with NDVI. NDWI is one of the most popular indices for mapping surface water. MNDWI is a modification to the NDWI, and it mainly addressed the problem of the false positives with built-up area using NDWI. For radar sensors, the VV band, VH band, cross ratio, and radar vegetation index (RVI) is provided by default. The VV band and VH band are original polarization bands from Sentinel-1 data, and they have been used for rice mapping in previous research (N. Chen et al., 2020; Onojeghuo et al., 2018). Table 10 lists all the features that can be selected or computed for each of the included datasets in the RiceMapEngine.

The next main preprocessing step is making composites. This step is very important because the study area may sit across swaths, which lead to inconsistent time-series for area located on different swaths. The composite can also help reduce cloud cover problem. The main parameters in making composites are 1) how many days of composite is needed, and 2) what composite type to use, i.e., which aggregation method to use for observations within a composite date range. RiceMapEngine allows user to enter the days of composite they need, and a default 15-day composite is provided. The composite type can be selected from mean, maximum, minimum, median, and mode, which are most common aggregation methods for making composites. For example, maximum composite is constantly used for making NDVI or EVI composite.

Lastly, the speckle filtering preprocessing step is very important for SAR image processing. Speckles are unique to SAR images. They are made from constructively or destructively compounding signals of neighboring pixels, which deteriorate the quality of SAR images and makes it hard to interpret SAR images (Z. Yu, Wang, et al., 2018). There are many speckle filtering methods. Spatial multi-looking is probably the simplest form of speckle filtering (Z. Yu, Wang, et al., 2018). Although such speckle filters often reduce spatial resolution of the original images, the fast computation and convenience make them extremely popular. A boxcar filter is one of such filters that does spatial average for each pixel. The filter can be easily implemented on GEE with a square kernel function. Another slightly more advanced multi-look speckle filter is Lee filter (Lee et al., 2015). In addition to the average intensity within the window, the Lee filter also takes local variance into computation (Rubel et al., 2021). Later, a modification based on Lee filter was introduced by Yommy et al. (2015), and it was named Refined Lee filter. We implemented these 3 speckle filters in the system, however, due to the limited computation resources allocated to GEE users, the refined Lee filter and the Lee filter fails to consistently run through all processing steps due to their increased computation intensity. Thus, the boxcar speckle filter of window size 5 is used as default for speckle filtering in the system.

5.2.2.3. Phenology Inspection

One important feature of RiceMapEngine is that it allows inspecting phenology of ground truth samples. Ground truth samples for rice mapping may include samples from different crop types, which are indifferentiable from single-look high resolution images like Google Earth. Phenology-based indicators like start-of-season, peak-of-season, end-of-season, and season length can help effectively differentiate different crop types (Tian et al., 2019). The transplanting phase of rice phenology uniquely differentiate it from other crop types(Motohka et al., 2009). Thus, ground truth samples of rice can be verified if the transplanting phase can be identified from its phenology.

RiceMapEngine implements this function by combining the dataset filtering function and the preprocessing function. Specifically, users need to specify which satellite dataset and the time frame of the images to be used. Then the preprocessing steps are applied on the selected satellite dataset to produce a consistent composite. The composite is then sampled at each ground truth sample location to get the time-series values. Then, the ground truth samples with time-series values appended to their property list are returned to the front end for visualizations. A time-series line chart will be plotted for a selected ground truth sample such that users can inspect the time-series to identify phenology-based indicators. In addition to time-series phenology curve selected by users, RiceMapEngine also loads month-by-month false color composite for each month within the selected time frame. The false color composite is made using an optical remote sensing dataset. The dataset is dynamically selected depending on the selected frame. For example, Sentinel-2 TOA reflectance dataset will be used if the time frame starts after June 2015 because the first image of Sentinel-2 was captured in June 2015. The month-by-month false color composites serve as visual clues aside the time-series phenology curve to assist inspecting the selected ground truth sample.

5.2.2.4. Classification

The last core function is paddy rice classification. RiceMapEngine provides two methods of rice mapping, one based on empirical statistics and the other based on ground truth samples. Both methods produce binary-class classifications, i.e., rice and non-rice.

The first method implements a simple threshold-based classification. After specifying the parameters for dataset filtering and preprocessing, users can specify time frames of satellite image data to be used and the thresholds for the feature values during such time frames. Pixels that satisfy the conditions will be classified as rice while others are classified as non-rice crop types. The mathematical representation of this method is shown in Equation 6.

Equation 6. Phenology-based thresholding method for rice classification.

$$Rice = (a_1 \leq X_1 \leq b_1\ )\ AND\ (a_2 \leq X_2 \leq b_2)\ AND\ ...AND\ (a_n \leq X_n \leq b_n)$$

Where X_i are observations within time frame i, and a_i, b_i are thresholds for time frame i. The rice mapping results take the logical and operation of thresholding results from all time frames.

The second method is supervised classification. This method requires users to upload ground truth samples as zipped shapefiles. After applying the dataset filtering and preprocessing steps, which are standard procedures for many tasks in RiceMapEngine, users can specify classification-specific parameters like the time frame of images to be used, which model to use, training details, etc. Table 11 shows the supported classification models and their GEE APIs. Internally, the selected image datasets will be filtered and preprocessed into composites, and the uploaded ground truth samples will be used to sample from the composites to attach image data to the samples. Then the selected model will be trained using the training set of the ground truth samples. The trained model will be used to produce the rice map. Lastly, the accuracy assessment step is conducted using the testing set. The confusion matrix, overall accuracy (OA), and Kappa coefficient will be reported.

Table 11. Supported classification models in RiceMapEngine

Model name	**GEE API**	**Reference**
Random Forest	ee.Classifier.smileRandomForest	(Breiman, 2001)
Gradient Boosting	ee.Classifier.smileGradientTreeBoost	(Friedman, 2001)
CART	ee.Classifier.smileCart	(Breiman et al., 1984)
Support Vector Machine	ee.Classifier.libsvm	(Noble, 2006)

5.3. Results

5.3.1. Main Workflows

5.3.1.1. Phenology Explorer

The first major function of RiceMapEngine is called phenology explorer. It aims to allow users to fine tune the ground truth samples using time-series satellite data as evidence and derive empirical thresholds for different phenological stages. It enables an interactive experience for users to examine ground truth samples collected from the field. The steps to use this function are as follows:

1) Upload ground truth samples to the app, the supported formats for the ground truth data are zipped shapefile and GeoJSON. The ground truth samples are then converted to JSON objects and stored in the frontend redux store. Samples are then showed in a list as well as on the map.
2) Choose the property and the property value that is the target class, e.g., ‘rice’ value in the property ‘cereal’. The samples that match the selection are highlighted both in the list and on the map, which helps differentiate samples that belong to the positive class and the negative class.
3) Specify the dataset name, filtering criteria, and preprocessing methods.
4) Select the date range of interest. The date range of interest defines the time frame that the images will be loaded. It also initializes mini zoomed-in maps corresponding to each month within the time frame for sample inspection at finer resolution later.

5) Send a request to the backend and fetch time series feature values for all samples. Also load monthly false color composite for each of the mini zoomed-in maps.
6) Show the time-series feature values as a chart when a feature is selected either from the list of samples or the map. The sample should also be highlighted in each of the mini zoomed-in maps such that the whereabouts at the sample location can be examined for each of the month within the selected time frame.
7) Examine a sample according to the chart of the time series curve and the zoomed-in mini maps to identify if the sample is valid, otherwise, delete the sample or edit the sample location on the map and go back to step 5 for another iteration.

If satisfied with the quality of samples, users can enter the date ranges of the sowing, peak, and/or harvesting phase, and get the minimum and maximum values for that phase. The minimum and maximum are derived using all values within the time frame of the phase from all samples that belong to the positive class. Outliers are eliminated using the 'interquartile' rule. The interquartile is defined as the third quartile minus first quartile, and the outliers are identified as any values that are outside the range between ($\mathrm{quartile}_{1\mathrm{st}} - 1.5 * \mathrm{interquartile}$) and ($quartile_{3rd} + 1.5 * interquartile$). After removing outliers, the minimum and maximum thresholds are defined as the ($mean - std$) and ($mean + std$).

5.3.1.2. Empirical Thresholding

The empirical thresholding function aims to allow users to classify the target crop type using known threshold values or empirical threshold values derived from the phenology explorer. This function can be used independently but is recommended to be used after phenology explorer. Crop type mapping often times rely on domain knowledge such as phenology and crop calendar. Such information is very helpful for choosing a specific time frame that can best differentiate the target crop type with other crop types. This function provides a simple method for unsupervised classification using domain knowledge. The steps to use this function is rather simple:

1) Specify the dataset name, filtering criteria, and preprocessing methods.
2) Specify the auxiliary datasets including the boundary for classification, which can be a predefined Nepal district boundary, or an uploaded zipped shapefile, and a crop mask, which should be a public asset on GEE. The crop mask for Nepal is used as default.
3) Switch on sowing, peak, and/or harvesting phases and specify the time frame and threshold values for each phase that is turned on.
4) Run the classification on the backend, and when completed, show the classification result for each of the turned-on phases and a combined result from all phases. The estimated area of the target crop type will also be calculated.
5) Export classification results as single-band GeoTIFF images where the target crop is of value 1 and other classes are of value 0.

5.3.1.3. Supervised Classification

Supervised classification function provides another method for rice mapping along with empirical thresholding. This function allows users to upload ground truth samples or use the ground truth samples uploaded from the phenology explorer, for supervised classification. The steps to use this function are as follows:

1) Specify the dataset name, filtering criteria, and preprocessing methods.
2) Upload ground truth samples or reuse ground truth samples uploaded from phenology explorer and specify the property and property value as the target class label.
3) Specify the classification-related parameters, including the date range of images to be used in classification, the ratio of data to be used in model training, the GEE classification model to be used and the corresponding model parameters.
4) Run the supervised classification and return the result as XYZ tiles to be visualized on the map.

5.3.2. User Interface Design

Figure 16 shows the main UI of the RiceMapEngine. There are 6 different panels along with the map component, and each panel serves for different purposes:

Panel (1) shows GUIs of data filters and preprocessing setup. The options of features dynamically change along with the selection of dataset.

Panel (2) shows the date range selectors for the sowing, peak and harvesting phenology stages and the threshold values for the corresponding season. Each season can be switched on or off to include or exclude it in the workflow.

Panel (3) shows GUI controls for classification parameters, including the date range of images to be used, the model to be used, and the model parameters for the selected model.

Panel (4) shows the zoomed-in false color monthly composites for selected date range. Each month within the date range is shown as a small map. When a ground truth sample is highlighted, all maps will center at the sample such that the whereabouts at the sample location during the selected time period can be clearly observed.

Panel (5) shows the container of ground truth samples, Users can upload ground truth samples as zipped files and the samples will be shown in the container as a list. In order to differentiate rice class with other classes, the class field and class value need to be selected from the properties of the samples. For example, the ‘Rice’ value from a property named ‘Crop type’ need to be selected to differentiate rice samples and other samples.

Panel (6) is a panel that shows the time-series of selected satellite data for the selected ground truth sample.

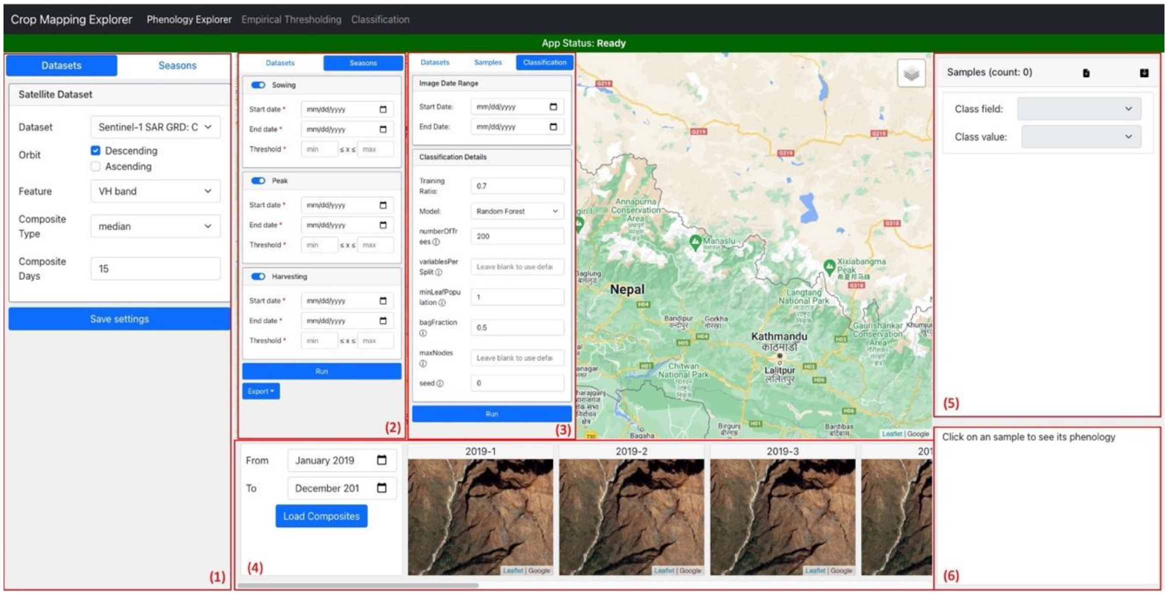

Figure 16. UI panels implemented in the RiceMapEngine.

In addition to the panels, the main component that occupies the screen is the map. The map was implemented using Leaflet web mapping library. The map stays stationary across different workflows and the UI panels change according to the current selected workflow. For phenology explorer, panel (1), (4), (5), and (6) will show up. For empirical thresholding, only panel (2) will show up, and lastly, panel (3) will show up for the supervised classification workflow.

5.3.3. Case Study

The RiceMapEngine was used for rice mapping operations in Nepal 2021, and it will be used for rice mapping operations in 2022 and onwards. This case study shows how RiceMapEngine was used for the Chitwan districts in the Terai belt region of Nepal. In short, the phenology explorer workflow was used to inspect the phenology of ground truth samples collected in 2020 to identify stale samples, transplanting time frame, and the empirical thresholds for Sentinel-1 SAR data in the transplanting time frame. Next, the empirical thresholding workflow was used to produce the early-season rice map for 2021 using thresholds derived from the last step. Lastly, the supervised classification workflow was used to produce post-season rice maps for 2021 using ground truth samples collected during the main season 2021.

Figure 17 shows the location of Chitwan district within the Terai belt region, and the cropland mask is applied. The ground truth samples that are used in this case study, including 356 samples collected in 2020 and 294 samples in 2021 are also showed on the figure. Field trips were conducted by local authorities during the main seasons in 2020 and 2021 to collect the ground truth samples. Both sets of ground truth samples include samples of multiple crop types in addition to rice, and the non-rice crop types are grouped as one class in the subsequent classifications.

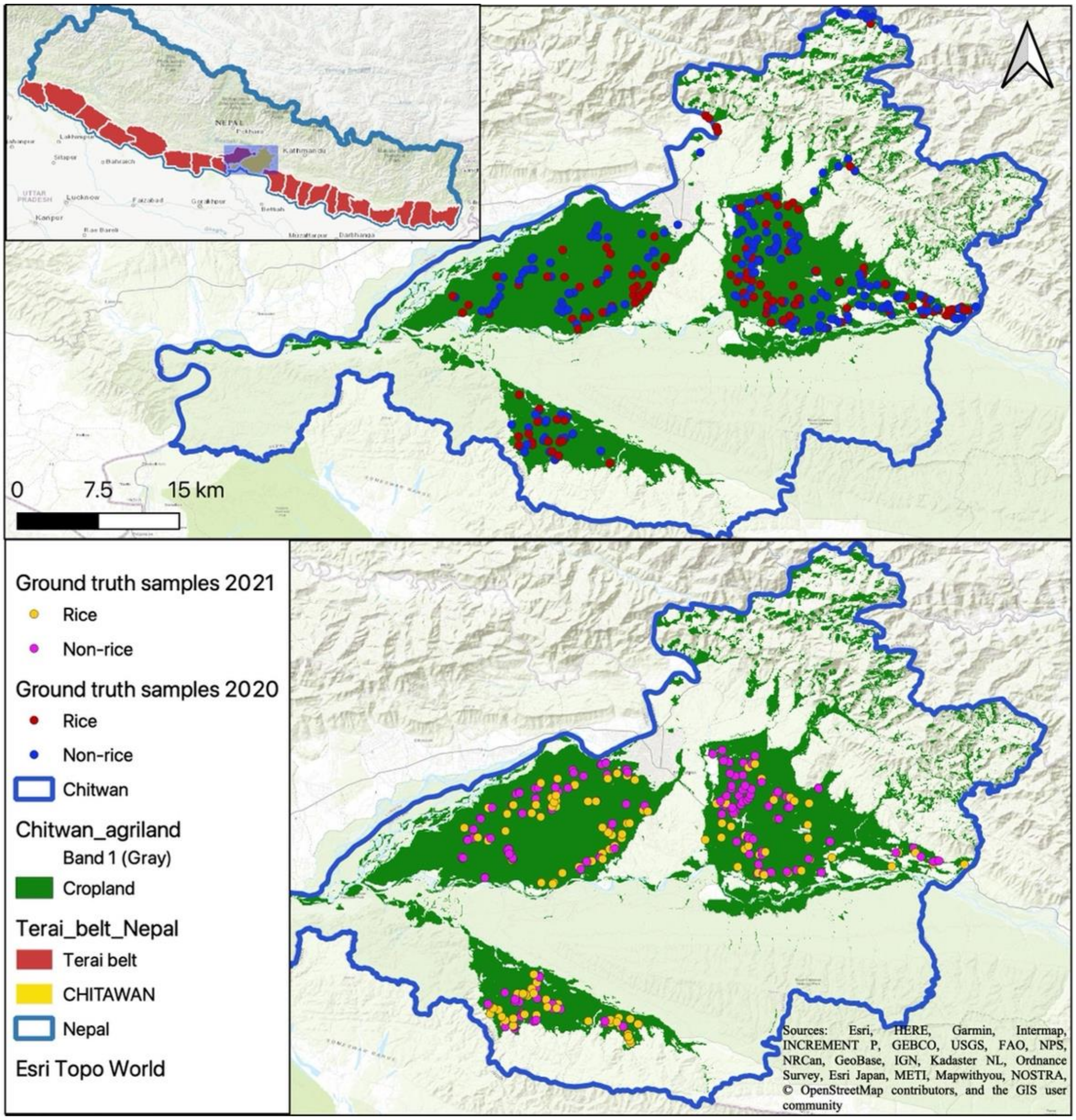

Figure 17. Chitwan district overlayed with crop mask and ground truth samples from 2020 and 2021.

5.3.3.1. Early-season rice mapping in 2021

One key feature of RiceMapEngine is to support rice mapping with simple thresholding. This allows early-season mapping if empirical thresholds can be known in front. In this case study, the early-season rice map of Chitwan in 2021 was produced using ground truth samples from 2020. Specifically, the ground truth samples from 2020 was uploaded to the phenology explorer, and the time period of phenology data was set to Jan 1st to Dec 31st, 2020. Figure 18 shows the zoomed-in maps for one of the rice samples. From the false color composite images for each of the month, we can see that cloud cover completely blocks view from May to September, and the images in October show signs of bare soil around the sample location, which indicate the harvesting phase.

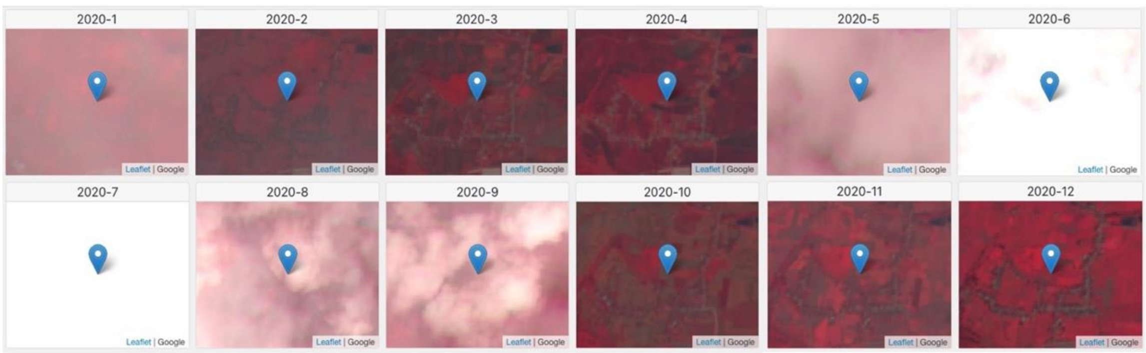

Figure 18. Zoomed-in maps showing month-by-month false-color composites at a rice sample location.

As we can see, the optical images are blocked by cloud cover during the critical transplanting and growing season of rice. Thus, the Sentinel-1 SAR data was chosen for phenology inspection. The VH band from Sentinel-1 SAR data was chosen as the feature to plot. A 15-day median composite processing is included in the preprocessing pipeline. Figure 19 shows the time-series of VH band for the same rice sample as shown in Figure 18. As Sentinel-1 SAR data is not interfered by cloud cover, the time series is thus continuous. From the time-series we can clearly match the curve with the month-by-month false color composites because the VH curve shows low values for October, which means the biomass is low. From the curve we can also see the peak is sometime in September, and the transplant phase should have happened mid-July. By using both the optical sensor readings and the sensor readings from radar sensors, the phenology stages of rice can be clearly identified. Based on the observed phenology, necessary corrections or deletion can be done to samples if the classes of the samples do not match with their observed phenology.

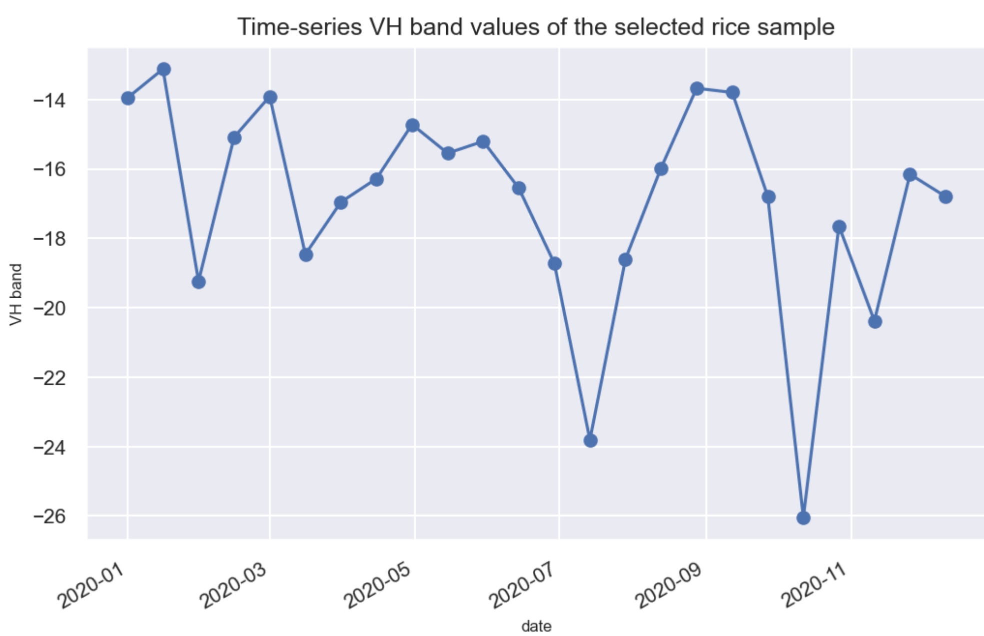

Figure 19. Time-series VH band values of the selected rice sample.

Based on the phenology of the rice samples, the transplanting time frame can be roughly estimated. In this case study, the transplanting phase was set from June 15th to July 31st, and the derived VH band value ranges during this period is from -23.67 to -

16.89. This range is then used in the empirical thresholding workflow to make early-season rice map for 2021. The early-season map for 2021 can be produced right after the transplanting phase using Sentinel-1 SAR images during the selected time frame for the transplanting phase. Figure 20 shows the produced early-season rice map. The reported area of the paddy rice fields according to this early-season rice map is 27958.251 ha. The ground truth samples collected during the main season 2021 were used to validate the early-season rice map 2021. Table 12 shows the confusion matrix of the early-season rice mapping result. As we can see from the matrix, most samples are correctly classified. There are only 5 false negative samples that were incorrectly classified as non-rice, and there are 44 false positive samples that were incorrectly classified as rice. As suggested by the number of false positive samples, the early-season classification result should be over estimating paddy rice area.

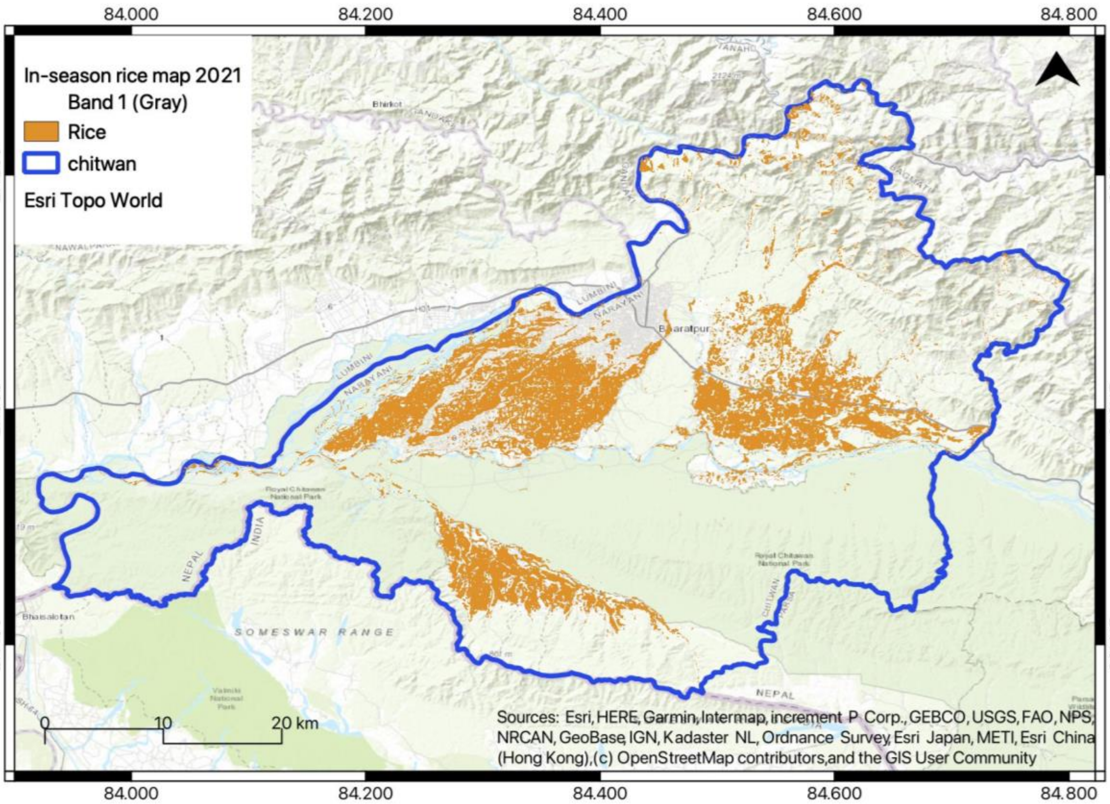

Figure 20. Early-season rice map for Chitwan district 2021.

Table 12. Confusion matrix of early-season rice map for 2021.

	Rice	**Non-rice**
Rice	127	44
Non-rice	5	118

Table 13. Accuracy assessment of post-season rice map for 2021.

Metrics	**Value**
Overall Accuracy	0.833
Kappa	0.670

The ground truth samples from 2020 was used to derive an early-season rice map for 2021 based on the assumption that the transplanting phase happens at roughly the same time across years, and the satellite recordings are stable across years. These assumptions need to be true such that the VH band value range derived using ground truth samples from 2020 can extrapolate to 2021. However, if such assumptions are not valid, especially when the transplanting phase windows are different across years, the uncertainty level of the early-season rice map may be high. Nonetheless, the early-season rice map can still be very useful for planning purpose as it can be produced quickly, and more importantly, the map is produced without requirement of ground truth samples from the current year.

5.3.3.2. Post-season rice mapping in 2021

As discussed in the previous section, the early-season rice map can be derived purely from empirical thresholds without the need of ground truth samples. When the main season is over, the post-season rice map can be derived using newly acquired ground truth samples during the growing season. ICIMOD conducted field trips in the entire Terai belt region during the main growing season of rice in 2021 and collected over 8000 ground truth samples. There are 294 samples located in Chitwan district. A straightforward supervised classification can be conducted using satellite images. In this case study, we again used Sentinel-1 SAR images as it is not affected by cloud covers. The same 15-day median composite is applied to produce consistent and continuous time-series. The image date range is chosen from June 1st, 2021, to Nov 1st, 2021, to roughly include the main season of rice with some margin on both sides. The model we used was

RF model with 200 estimators, and the rest parameters are set with default values. To validate classification results, a random 70% of the 294 samples were used in model training and the rest were used for accuracy assessment.

Figure 21 shows the result of the post-season classification. The reported area of paddy rice fields according to the post-season rice map is 21220.913 ha. The confusion matrix created using the 30% testing samples is shown in Table 14 and the OA and Kappa scores are shown in Table 15. From the result, we can see that the classification result is satisfactory as both the OA and Kappa scores are higher than 0.9 which means the classification result agrees well with the ground truth data.

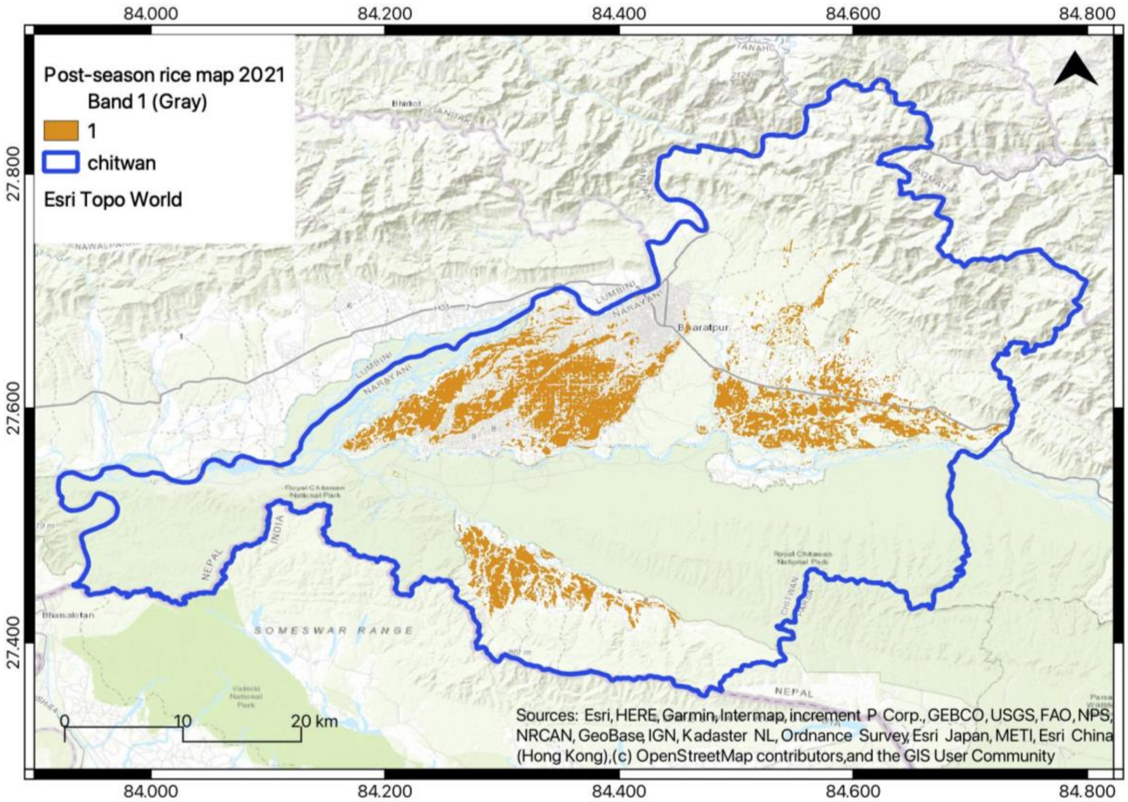

Figure 21. Post-season rice map for Chitwan district 2021.

Table 14. Confusion matrix of the post-season rice map 2021.

	Rice	**Non-rice**
Rice	53	2
Non-rice	1	36

Table 15. Accuracy assessment of post-season rice map 2021.

Metrics	**Value**
Overall Accuracy	0.967
Kappa	0.932

Comparing the post-season rice map and the early-season rice map, we can see that the post-season rice map shows less paddy rice area than the early-season map, which means the early-season rice map has a lot of overestimations. The actual area reported by RiceMapEngine for early-season rice map is 27958.251 ha and the reported area for post-season rice map is 21220.913 ha. Thus, around 25% of the area shown on the early-season map is false positives.

5.4. Conclusion

This chapter presents a rice mapping application, named RiceMapEngine, that uses GEE Python APIs to provide advanced rice mapping workflows to remote sensing researchers and decision makers. The most desirable feature of RiceMapEngine is that it allows user to use GEE services without possessing programming skills, which can bridge the gap between many researchers and the GEE. The software design and architecture of RiceMapEngine are discussed in detail. Three main workflows, namely phenology explorer, empirical thresholding, and supervised classification are introduced., and a case study for rice mapping in the Chitwan district of Nepal using the workflows is demonstrated and discussed. In this case study, the phenology explorer workflow was used to identify transplanting time frame and identify low-quality ground truth samples. Then in the empirical thresholding workflow, the thresholds for the VH band of Sentinel-1 SAR data within the transplanting phase were calculated and were used in the threshold-based classification, which yields the early-season rice maps for 2021. After the season was over and ground truth samples for 2021 were collected, the RiceMapEngine was used to conduct post-season rice mapping using models trained with the ground truth samples for 2021. This case study shows that RiceMapEngine can be used for year-to-year continuous rice mapping operations with the early-season maps that provides in-time estimates of paddy rice area and extents, and the post-season maps that provide most accurate estimates of main season paddy rice area and extents.

6. SUMMARY AND CONCLUSIONS

SA region is home to more than a quarter of the world's undernourished people, and the region is also one of the poorest regions in the world (FAO, 2009). Agriculture is the very important to SA region because it is one of the major economic sources for this region and the food production is crucial for global food security. According to FAO, around 57% of the land in SA is dedicated to agriculture, and for countries like Bangladesh, the number can go up to 70% (FAO, 2009). To feed the growing populations, the agriculture lands in SA are experiencing several changes including transitions from agriculture to more-profitable fishery and crop intensification. These changes not only have impact on the food security, but it also has profound impact on the environment and climate change. As climate variability accounts for nearly one third of the crop yield variability, the climate change will impact the crop yield significantly, which pose great challenges to the global food security (Ray et al., 2015). Thus, it is very important to monitor the extent and health of agriculture timely to detect changes of existing agriculture lands. This dissertation aims to design novel algorithms and tools using remote sensing dataset for agriculture mapping and monitoring in SA region. This overarching goal is fulfilled by achieving the three research objectives as introduced in section 1.3. Each research objective is discussed in detail in a single chapter. Here we summarize the major findings for each of the objectives and the theoretical and methodological contributions respectively.

Objective 1: Develop a novel GEE-based workflow to map inland fishponds.

Chapter 3 presents a GEE-based workflow that uses spectral and spatial information derived from remote sensing images for inland fishpond mapping. The workflow first derives multi-temporal WI series to identify persistent water features, and then it derives OBFs from the shapes of these water features to classify them into fishponds and non-fishponds. A major finding is that to accurately classify fishponds which are small and grouped as scattered clusters, applying the pixel selection technique will significantly help reduce false positives. A case study in Singra Upazila was conducted. We manually digitized fishponds in this Upazila and validated the performance of the workflow. The result showed that the presented workflow achieved a precision score of 0.788 and the recall score is 0.538, and the F1 score is 0.640. The main limitation is that the 10 m spatial resolution of the remote sensing images we used is not high enough to identify extremely small fishponds, especially when they are close together. The entire workflow was implemented on GEE such that the results can be easily reproduced, and the method can be applied to a different area conveniently.

Objective 2: Investigate crop intensity mapping using remote sensing data and GEE.

Chapter 4 presented a GEE-based workflow that uses MODIS Terra and Aqua surface reflectance data for crop intensity mapping in Bangladesh. Facing the challenge of severe missing data problem caused by persistent cloud cover during monsoon season, this research first combines Terra and Aqua data to mitigate cloud issues, and then we adopt Harmonic Regression to reconstruct NDVI curves because it is well-suited to periodic signals just like the repeating seasons year after years and that it produces a continuous and smooth function regardless of the presence of missing data. A simple heuristic was applied on the reconstructed NDVI time-series to obtain the number of cropping cycles. Specifically, the heuristic uses a threshold of 0.5 to detect the peaks of the reconstructed NDVI curves in a growing season. A valid crop cycle should cross the threshold line twice. The crop intensity map of Bangladesh 2010 was produced using this method. The spatial distribution of different crop systems roughly matches with the geo-physical characteristics of Bangladesh. The crop intensity map was aggregated to district level and the average crop intensity in each district was compared with statistics from BBS. The comparison showed that the map result underestimated the crop intensity. The national average crop intensity was 1.91 for 2010 according to the statistics and our result showed 1.66. The main reason behind the difference is the persistent cloud cover during monsoon seasons. The clouds may block the view of an entire crop season in between the winter and main season such that it cannot be reconstructed from the NDVI time-series.

Objective 3: Design a GEE-based software for ground truth sample validation and fast paddy rice mapping.

These research questions should be answered: How to efficiently use GEE in the software? How to validate ground truth samples using their phenology? How to use the software to produce paddy rice maps with or without ground truth samples? A case study needs to be conducted to showcase how to use the software and the accuracies of the rice maps need to be assessed.

Chapter 5 presented a GEE-enabled web application named RiceMapEngine. The web application encapsulates several reusable modules to simplify data processing workflow. Users of this application interact with the application through GUIs that are more intuitive and convenient to use than writing code. The GUI will help higher level officials and decision makers to use GEE-based rice mapping workflows with ease. Three main workflows, i.e., phenology explorer, empirical thresholding, and supervised classification were designed and implemented in the RiceMapEngine. The phenology explorer handles ground truth sample validation by showing users with time-series satellite data in the form of charts and images. Empirical thresholding can be used to produce paddy rice maps using only empirically derived thresholds. Supervised classification can be used as another method to produce paddy rice maps using ground truth samples validated from phenology explorer. A case study for rice mapping operation in Chitwan district of Nepal was carried out. The case study used phenology explorer workflow to validate ground truth samples from 2020 and derived the time frame and empirical thresholds for the transplanting phase. The thresholds and time frame were then used in the empirical thresholding workflow for early-season rice mapping in 2021. After the 2021 main season ends and ground truth samples were collected in the season, the post-season rice map was produced using the supervised classification workflow. Using phenology explorer, we successfully identified the transplanting phase inspecting the time-series Sentinel-1 images. The early-season rice map achieved an OA of 0.833 and the Kappa score of 0.67. The post-season rice map achieved an OA of 0.967 and the Kappa score of 0.932. Despite that early-season rice map is less accurate than post-season rice map, mostly because of the overestimation, early-season rice maps require no ground truth samples, and it can be produced right after the transplanting phase of rice, which can be extremely helpful for early planning and resource allocations.

In summary, this dissertation has several main contributions: 1) presented a solution to integrate spectral, temporal and spatial information for inland fishpond identification, which can help monitor the ongoing transitions from agriculture to aquaculture in SA; 2) Presented a workflow on GEE that combines MODIS Terra and Aqua surface reflectance data and applies Harmonic Regression for crop intensity mapping, which can help monitor the spatial distribution of crop intensity in addition to traditional statistical data; 3) Designed a GEE-enabled web application that allows one-stop experience of refining ground truth samples and producing paddy rice maps, which will make it far more convenient to monitor paddy rice extent.

REFERENCES

Abburu, S., & Babu Golla, S. (2015). Satellite Image Classification Methods and Techniques: A Review. *International Journal of Computer Applications*, *119*(8), 20–25. https://doi.org/10.5120/21088-3779

Agriculture and Climate Change: Towards Sustainable, Productive and Climate-Friendly Agricultural Systems. (2016). https://doi.org/10.1787/5jxrclljnbxq-en

Alam, M. S., Quayum, M., & Islam, M. (2010). Crop Production in the Haor Areas of Bangladesh: Insights from Farm Level Survey. *The Agriculturists*, *8*(2), 88–97. https://doi.org/10.3329/agric.v8i2.7582

Amani, M., Ghorbanian, A., Ahmadi, S. A., Kakooei, M., Moghimi, A., Mirmazloumi, S. M., Moghaddam, S. H. A., Mahdavi, S., Ghahremanloo, M., Parsian, S., Wu, Q., & Brisco, B. (2020). Google Earth Engine Cloud Computing Platform for Remote Sensing Big Data Applications: A Comprehensive Review. *IEEE Journal of Selected Topics in Applied Earth Observations and Remote Sensing*, *13*, 5326–5350. https://doi.org/10.1109/JSTARS.2020.3021052

Belton, B., & Azad, A. (2012). The characteristics and status of pond aquaculture in Bangladesh. *Aquaculture*, *358–359*, 196–204. https://doi.org/10.1016/j.aquaculture.2012.07.002

Biradar, C. M., & Xiao, X. (2011). Quantifying the area and spatial distribution of double- and triple-cropping croplands in India with multi-temporal MODIS imagery in 2005. *International Journal of Remote Sensing*, *32*(2), 367–386. https://doi.org/10.1080/01431160903464179

Blaes, X., Vanhalle, L., & Defourny, P. (2005). Efficiency of crop identification based on optical and SAR image time series. *Remote Sensing of Environment*, *96*(3–4), 352–365. https://doi.org/10.1016/j.rse.2005.03.010

Breiman, L. (2001). Random forests. *Machine Learning*, *45*(1), 5–32. https://doi.org/10.1023/A:1010933404324

Breiman, L., Jerome, F., Charles, J. S., & Richard, A. O. (1984). *Classification and regression trees*. CRC Press. https://scholar.google.com/scholar_lookup?hl=en&publication_year=1984&author=

L.+Breiman&author=J. H.+Friedman&author=R. A.+Olshen&author=C. J.+Stone&title=Classification+and+Regression+Trees

Brinkhoff, J., Vardanega, J., & Robson, A. J. (2020). Land cover classification of nine perennial crops using sentinel-1 and -2 data. *Remote Sensing*, *12*(1), 1–26. https://doi.org/10.3390/rs12010096

Cai, Y., Guan, K., Peng, J., Wang, S., Seifert, C., Wardlow, B., & Li, Z. (2018). A high-performance and in-season classification system of field-level crop types using time-series Landsat data and a machine learning approach. *Remote Sensing of Environment*, *210*, 35–47. https://doi.org/10.1016/j.rse.2018.02.045

Calvario Sanchez, G., Dalmau, O., Alarcon, T. E., Sierra, B., & Hernandez, C. (2018). Selection and fusion of spectral indices to improve water body discrimination. *IEEE Access*, *6*, 72952–72961. https://doi.org/10.1109/ACCESS.2018.2881430

Chakhar, A., Hernández-López, D., Ballesteros, R., & Moreno, M. A. (2021). Improving the accuracy of multiple algorithms for crop classification by integrating sentinel-1 observations with sentinel-2 data. *Remote Sensing*, *13*(2), 1–21. https://doi.org/10.3390/rs13020243

Chakhar, A., Ortega-Terol, D., Hernández-López, D., Ballesteros, R., Ortega, J. F., & Moreno, M. A. (2020). Assessing the accuracy of multiple classification algorithms for crop classification using landsat-8 and sentinel-2 data. *Remote Sensing*, *12*(11), 1735. https://doi.org/10.3390/rs12111735

Chen, N., Yu, L., Zhang, X., Shen, Y., Zeng, L., Hu, Q., & Niyogi, D. (2020). Mapping paddy rice fields by combining multi-temporal vegetation index and synthetic aperture radar remote sensing data using Google Earth Engine machine learning platform. *Remote Sensing*, *12*(18), 2992. https://doi.org/10.3390/RS12182992

Chen, R., Li, X., & Li, J. (2018). Object-based features for house detection from RGB high-resolution images. *Remote Sensing*, *10*(3), 451. https://doi.org/10.3390/rs10030451

Chen, S., Useya, J., & Mugiyo, H. (2020). Decision-level fusion of Sentinel-1 SAR and Landsat 8 OLI texture features for crop discrimination and classification: case of Masvingo, Zimbabwe. *Heliyon*, *6*(11), e05358. https://doi.org/10.1016/j.heliyon.2020.e05358

Cui, J., Zhang, X., Wang, W., & Wang, L. (2020). Integration of optical and sar remote sensing images for crop-type mapping based on a novel object-oriented feature selection method. *International Journal of Agricultural and Biological Engineering*, *13*(1), 178–190. https://doi.org/10.25165/j.ijabe.20201301.5285

Denize, J., Hubert-Moy, L., Betbeder, J., Corgne, S., Baudry, J., & Pottier, E. (2019). Evaluation of using sentinel-1 and -2 time-series to identifywinter land use in agricultural landscapes. *Remote Sensing*, *11*(1), 37. https://doi.org/10.3390/rs11010037

Donchyts, G., Schellekens, J., Winsemius, H., Eisemann, E., & van de Giesen, N. (2016). A 30 m resolution surfacewater mask including estimation of positional and thematic differences using landsat 8, SRTM and OPenStreetMap: A case study in the Murray-Darling basin, Australia. *Remote Sensing*, *8*(5), 386. https://doi.org/10.3390/rs8050386

Dong, J., Xiao, X., Menarguez, M. A., Zhang, G., Qin, Y., Thau, D., Biradar, C., & Moore, B. (2016). Mapping paddy rice planting area in northeastern Asia with Landsat 8 images, phenology-based algorithm and Google Earth Engine. *Remote Sensing of Environment*, *185*, 142–154. https://doi.org/10.1016/j.rse.2016.02.016

Du, Y., Zhang, Y., Ling, F., Wang, Q., Li, W., & Li, X. (2016). Water bodies' mapping from Sentinel-2 imagery with Modified Normalized Difference Water Index at 10-m spatial resolution produced by sharpening the swir band. *Remote Sensing*, *8*(4). https://doi.org/10.3390/rs8040354

El-Deen Taha, L. G., & Elbeih, S. F. (2010). Investigation of fusion of SAR and Landsat data for shoreline super resolution mapping: The northeastern mediterranean sea coast in Egypt. *Applied Geomatics*, *2*(4), 177–186. https://doi.org/10.1007/s12518-010-0033-x

FAO. (2009). How to Feed the World in 2050. *Insights from an Expert Meeting at FAO*, *2050*(1), 1–35. http://scholar.google.com/scholar?hl=en&btnG=Search&q=intitle:How+to+Feed+the+World+in+2050#3%5Cnhttp://www.fao.org/fileadmin/templates/wsfs/docs/expert_paper/How_to_Feed_the_World_in_2050.pdf

FAO, IFAD, UNICEF, WFP, & WHO. (2021). The State of Food Security and Nutrition in the World 2021. In *Transforming food systems for food security, improved nutrition and affordable healthy diets for all*. FAO. https://doi.org/10.4060/cb4474en

Faridatul, M. I., & Wu, B. (2018). Automatic Classification of Major Urban Land Covers Based on Novel Spectral Indices. *ISPRS International Journal of Geo-Information*, *7*(12), 453. https://doi.org/10.3390/ijgi7120453

Feng, S., Zhao, J., Liu, T., Zhang, H., Zhang, Z., & Guo, X. (2019). Crop Type Identification and Mapping Using Machine Learning Algorithms and Sentinel-2 Time Series Data. *IEEE Journal of Selected Topics in Applied Earth Observations* *and Remote Sensing*, *12*(9), 3295–3306. https://doi.org/10.1109/JSTARS.2019.2922469

Feyisa, G. L., Meilby, H., Fensholt, R., & Proud, S. R. (2014a). Automated Water Extraction Index: A new technique for surface water mapping using Landsat imagery. *Remote Sensing of Environment*, *140*, 23–35. https://doi.org/10.1016/j.rse.2013.08.029

Feyisa, G. L., Meilby, H., Fensholt, R., & Proud, S. R. (2014b). Automated Water Extraction Index: A new technique for surface water mapping using Landsat imagery. *Remote Sensing of Environment*, *140*, 23–35. https://doi.org/10.1016/j.rse.2013.08.029

Fisher, A., Flood, N., & Danaher, T. (2016). Comparing Landsat water index methods for automated water classification in eastern Australia. *Remote Sensing of Environment*, *175*, 167–182. https://doi.org/10.1016/j.rse.2015.12.055

Foley, J. A., DeFries, R., Asner, G. P., Barford, C., Bonan, G., Carpenter, S. R., Chapin, F. S., Coe, M. T., Daily, G. C., Gibbs, H. K., Helkowski, J. H., Holloway, T., Howard, E. A., Kucharik, C. J., Monfreda, C., Patz, J. A., Prentice, I. C., Ramankutty, N., & Snyder, P. K. (2005). Global consequences of land use. *Science*, *309*(5734), 570–574. https://doi.org/10.1126/SCIENCE.1111772/SUPPL_FILE/FOLEY_SOM.PDF

Friedl, M. A., & Brodley, C. E. (1997). Decision tree classification of land cover from remotely sensed data. *Remote Sensing Environ.*, *61*, 399–409.

Friedman, J. H. (2001). Greedy function approximation: A gradient boosting machine. *Annals of Statistics*, *29*(5), 1189–1232. https://doi.org/10.1214/aos/1013203451

Frohn, R. C. (2006). The use of landscape pattern metrics in remote sensing image classification. *International Journal of Remote Sensing*, *27*(10), 2025–2032. https://doi.org/10.1080/01431160500212229

Gao, B. C. (1996). NDWI - A normalized difference water index for remote sensing of vegetation liquid water from space. *Remote Sensing of Environment*, *58*(3), 257–266. https://doi.org/10.1016/S0034-4257(96)00067-3

Ghassemian, H. (2016). A review of remote sensing image fusion methods. In *Information Fusion* (Vol. 32, pp. 75–89). https://doi.org/10.1016/j.inffus.2016.03.003

Ghazaryan, G., Dubovyk, O., Löw, F., Lavreniuk, M., Kolotii, A., Schellberg, J., & Kussul, N. (2018). A rule-based approach for crop identification using multi-temporal and multi-sensor phenological metrics. *European Journal of Remote Sensing*, *51*(1), 511–524. https://doi.org/10.1080/22797254.2018.1455540

Gorelick, N., Hancher, M., Dixon, M., Ilyushchenko, S., Thau, D., & Moore, R. (2017). Google Earth Engine: Planetary-scale geospatial analysis for everyone. *Remote Sensing of Environment*, *202*, 18–27. https://doi.org/10/gddm6z

Gray, J., Friedl, M., Frolking, S., Ramankutty, N., Nelson, A., & Gumma, M. K. (2014). Mapping Asian cropping intensity with MODIS. *IEEE Journal of Selected Topics in Applied Earth Observations and Remote Sensing*, *7*(8), 3373–3379. https://doi.org/10.1109/JSTARS.2014.2344630

Guan, X., Huang, C., Liu, G., Meng, X., & Liu, Q. (2016). Mapping rice cropping systems in Vietnam using an NDVI-based time-series similarity measurement based on DTW distance. *Remote Sensing*, *8*(1). https://doi.org/10.3390/rs8010019

Gumma, M. K. (2011). Mapping rice areas of South Asia using MODIS multitemporal data. *Journal of Applied Remote Sensing*, *5*(1), 053547. https://doi.org/10.1117/1.3619838

Guo, Q., Pu, R., Li, J., & Cheng, J. (2017). A weighted normalized difference water index for water extraction using landsat imagery. *International Journal of Remote Sensing*, *38*(19), 5430–5445. https://doi.org/10.1080/01431161.2017.1341667

Haack, B. N., Herold, N. D., & Bechdol, M. A. (2000). Radar and optical data integration for land-use/land-cover mapping. In *Photogrammetric Engineering and Remote Sensing* (Vol. 66, Issue 6).

Han, H., Ma, M., Wang, X., & Ma, S. (2014). Classifying cropping area of middle Heihe River Basin in China using multitemporal Normalized Difference Vegetation Index data. *Journal of Applied Remote Sensing*, *8*(1), 083654. https://doi.org/10.1117/1.jrs.8.083654

Hänsch, R., Schulz, K., & Sörgel, U. (2018). Machine learning methods for remote sensing applications: an overview. *PROCEEDINGS OF SPIE*, *1079002*(October 2018), 1. https://doi.org/10.1117/12.2503653

HAO, P. yu, TANG, H. jun, CHEN, Z. xin, MENG, Q. yan, & KANG, Y. peng. (2020). Early-season crop type mapping using 30-m reference time series. *Journal of Integrative Agriculture*, *19*(7), 1897–1911. https://doi.org/10.1016/S2095-3119(19)62812-1

HAO, P. yu, TANG, H. jun, CHEN, Z. xin, YU, L., & WU, M. quan. (2019). High resolution crop intensity mapping using harmonized Landsat-8 and Sentinel-2 data.

Journal of Integrative Agriculture, *18*(12), 2883–2897. https://doi.org/10.1016/S2095-3119(19)62599-2

Hashem, S., Akter, T., Salam, M. A., Tawheed Hasan, M., & Hasan, M. T. (2014). Aquaculture planning through Remote Sensing Image analysis and GIS tools in North east region, Bangladesh. *International Journal of Fisheries and Aquatic Studies IJFAS*, *1*(5), 127–136.

Herold, N. D., & Haack, B. N. (2002). Fusion of radar and optical data for land cover mapping. *Geocarto International*, *17*(2), 21–30. https://doi.org/10.1080/10106040208542232

Huang, C., Chen, Y., Zhang, S., & Wu, J. (2018). Detecting, Extracting, and Monitoring Surface Water From Space Using Optical Sensors: A Review. *Reviews of Geophysics*, *56*(2), 333–360. https://doi.org/10.1029/2018RG000598

Huang, X., Liu, J., Zhu, W., Atzberger, C., & Liu, Q. (2019). The optimal threshold and vegetation index time series for retrieving crop phenology based on a modified dynamic threshold method. *Remote Sensing*, *11*(23), 2725. https://doi.org/10.3390/rs11232725

Huete, A. R. (1988). A soil-adjusted vegetation index (SAVI). *Remote Sensing of Environment*, *25*(3), 295–309. https://doi.org/10.1016/0034-4257(88)90106-X

Huntington, J. L., Hegewisch, K. C., Daudert, B., Morton, C. G., Abatzoglou, J. T., McEvoy, D. J., & Erickson, T. (2017). Climate engine: Cloud computing and visualization of climate and remote sensing data for advanced natural resource monitoring and process understanding. *Bulletin of the American Meteorological Society*, *98*(11), 2397–2409. https://doi.org/10.1175/BAMS-D-15-00324.1

Inoue, S., Ito, A., & Yonezawa, C. (2020). Mapping Paddy fields in Japan by using a Sentinel-1 SAR time series supplemented by Sentinel-2 images on Google Earth Engine. *Remote Sensing*, *12*(10). https://doi.org/10.3390/rs12101622

Jain, M., Mondal, P., DeFries, R. S., Small, C., & Galford, G. L. (2013). Mapping cropping intensity of smallholder farms: A comparison of methods using multiple sensors. *Remote Sensing of Environment*, *134*, 210–223. https://doi.org/10.1016/j.rse.2013.02.029

Jakovljević, G., Govedarica, M., & Álvarez-Taboada, F. (2019). Waterbody mapping: a comparison of remotely sensed and GIS open data sources. *International Journal of Remote Sensing*, *40*(8), 2936–2964. https://doi.org/10.1080/01431161.2018.1538584

Ji, L., Zhang, L., & Wylie, B. (2009a). Analysis of dynamic thresholds for the normalized difference water index. *Photogrammetric Engineering and Remote Sensing*, *75*(11), 1307–1317. https://doi.org/10.14358/PERS.75.11.1307

Ji, L., Zhang, L., & Wylie, B. (2009b). Analysis of dynamic thresholds for the normalized difference water index. *Photogrammetric Engineering and Remote Sensing*, *75*(11), 1307–1317. https://doi.org/10.14358/PERS.75.11.1307

Jia, K., Jiang, W., Li, J., & Tang, Z. (2018). Spectral matching based on discrete particle swarm optimization: A new method for terrestrial water body extraction using multi-temporal Landsat 8 images. *Remote Sensing of Environment*, *209*, 1–18. https://doi.org/10.1016/j.rse.2018.02.012

Jiang, H., Feng, M., Zhu, Y., Lu, N., Huang, J., & Xiao, T. (2014). An automated method for extracting rivers and lakes from Landsat imagery. *Remote Sensing*, *6*(6), 5067–5089. https://doi.org/10.3390/rs6065067

Jiang, Y., Lu, Z., Li, S., Lei, Y., Chu, Q., Yin, X., & Chen, F. (2020). Large-scale and high-resolution crop mapping in china using sentinel-2 satellite imagery. *Agriculture (Switzerland)*, *10*(10), 1–17. https://doi.org/10.3390/agriculture10100433

Jiao, L., Liu, Y., & Li, H. (2012). Characterizing land-use classes in remote sensing imagery by shape metrics. *ISPRS Journal of Photogrammetry and Remote Sensing*, *72*, 46–55. https://doi.org/10/f4b3q8

Jitkajornwanich, K., Vateekul, P., Panboonyuen, T., Lawawirojwong, S., & Srisonphan, S. (2018). Road map extraction from satellite imagery using connected component analysis and landscape metrics. *Proceedings - 2017 IEEE International Conference on Big Data, Big Data 2017*, *2018-Janua*, 3435–3442. https://doi.org/10.1109/BigData.2017.8258330

Jönsson, P., & Eklundh, L. (2002). Seasonality extraction by function fitting to time-series of satellite sensor data. *IEEE Transactions on Geoscience and Remote Sensing*, *40*(8), 1824–1832. https://doi.org/10.1109/TGRS.2002.802519

Jordan, C. F. (1969). Derivation of Leaf-Area Index from Quality of Light on the Forest Floor. *Ecology*, *50*(4), 663–666. https://doi.org/10.2307/1936256

Kauth, R. J. (1976). TASSELLED CAP - A GRAPHIC DESCRIPTION OF THE SPECTRAL-TEMPORAL DEVELOPMENT OF AGRICULTURAL CROPS AS SEEN BY LANDSAT. *Docs.Lib.Purdue.Edu*, 41–51. http://docs.lib.purdue.edu/lars_symphttp://docs.lib.purdue.edu/lars_symp/159

Kenduiywo, B. K., Bargiel, D., & Soergel, U. (2018). Crop-type mapping from a sequence of Sentinel 1 images. *International Journal of Remote Sensing*, *39*(19), 6383–6404. https://doi.org/10.1080/01431161.2018.1460503

Kleinbaum, D. G., & Klein, M. (2010). *Logistic Regression*. Springer New York. http://link.springer.com/10.1007/978-1-4419-1742-3

Kordelas, G. A., Manakos, I., Aragonés, D., Díaz-Delgado, R., & Bustamante, J. (2018). Fast and automatic data-driven thresholding for inundation mapping with Sentinel-2 data. *Remote Sensing*, *10*(6), 910. https://doi.org/10.3390/rs10060910

Kulkarni, S. C., & Rege, P. P. (2020). Pixel level fusion techniques for SAR and optical images: A review. *Information Fusion*, *59*, 13–29. https://doi.org/10.1016/j.inffus.2020.01.003

Lee, J. sen, Ainsworth, T. L., Wang, Y., & Chen, K. S. (2015). Polarimetric SAR speckle filtering and the extended sigma filter. *IEEE Transactions on Geoscience and Remote Sensing*, *53*(3), 1150–1160. https://doi.org/10.1109/TGRS.2014.2335114

Li, D. W., Yang, F. B., & Wang, X. X. (2015). Crop region extraction of remote sensing images based on fuzzy ARTMAP and adaptive boost. *Journal of Intelligent and Fuzzy Systems*, *29*(6), 2787–2794. https://doi.org/10.3233/IFS-151983

Li, L., Friedl, M. A., Xin, Q., Gray, J., Pan, Y., & Frolking, S. (2014). Mapping crop cycles in China using MODIS-EVI time series. *Remote Sensing*, *6*(3), 2473–2493. https://doi.org/10.3390/rs6032473

Li, W., Chen, T., Wentz, E. A., & Fan, C. (2014). NMMI: A Mass Compactness Measure for Spatial Pattern Analysis of Areal Features. *Annals of the Association of American Geographers*, *104*(6), 1116–1133. https://doi.org/10.1080/00045608.2014.941732

LIU, C. an, CHEN, Z. xin, SHAO, Y., CHEN, J. song, Hasi, T., & PAN, H. zhu. (2019). Research advances of SAR remote sensing for agriculture applications: A review. *Journal of Integrative Agriculture*, *18*(3), 506–525. https://doi.org/10.1016/S2095-3119(18)62016-7

Liu, H., & Jezek, K. C. (2004). Automated extraction of coastline from satellite imagery by integrating Canny edge detection and locally adaptive thresholding methods. *International Journal of Remote Sensing*, *25*(5), 937–958. https://doi.org/10.1080/0143116031000139890

Liu, H. Q., & Huete, A. (1995). Feedback based modification of the NDVI to minimize canopy background and atmospheric noise. *IEEE Transactions on Geoscience and Remote Sensing*, *33*(2), 457–465. https://doi.org/10.1109/36.377946

Liu, K., Ai, B., & Wang, S. (2010). Fish-pond change detection based on short term time series of RADARSAT images and object-oriented method. *Proceedings - 2010 3rd International Congress on Image and Signal Processing, CISP 2010*, *5*, 2175–2179. https://doi.org/10/cg2df9

Liu, L., Xiao, X., Qin, Y., Wang, J., Xu, X., Hu, Y., & Qiao, Z. (2020a). Mapping cropping intensity in China using time series Landsat and Sentinel-2 images and Google Earth Engine. *Remote Sensing of Environment*, *239*, 111624. https://doi.org/10.1016/j.rse.2019.111624

Liu, L., Xiao, X., Qin, Y., Wang, J., Xu, X., Hu, Y., & Qiao, Z. (2020b). Mapping cropping intensity in China using time series Landsat and Sentinel-2 images and Google Earth Engine. *Remote Sensing of Environment*, *239*, 111624. https://doi.org/10.1016/j.rse.2019.111624

Lu, D., & Weng, Q. (2007). A survey of image classification methods and techniques for improving classification performance. In *International Journal of Remote Sensing* (Vol. 28, Issue 5, pp. 823–870). Taylor and Francis Ltd. https://doi.org/10.1080/01431160600746456

Ludwig, C., Walli, A., Schleicher, C., Weichselbaum, J., & Riffler, M. (2019a). A highly automated algorithm for wetland detection using multi-temporal optical satellite data. *Remote Sensing of Environment*, *224*, 333–351. https://doi.org/10.1016/j.rse.2019.01.017

Ludwig, C., Walli, A., Schleicher, C., Weichselbaum, J., & Riffler, M. (2019b). A highly automated algorithm for wetland detection using multi-temporal optical satellite data. *Remote Sensing of Environment*, *224*, 333–351. https://doi.org/10.1016/j.rse.2019.01.017

Ma, Z., Liu, Z., Zhao, Y., Zhang, L., Liu, D., Ren, T., Zhang, X., & Li, S. (2020). An Unsupervised Crop Classification Method Based on Principal Components Isometric Binning. *ISPRS International Journal of Geo-Information*, *9*(11), 648. https://doi.org/10.3390/ijgi9110648

Malamiri, H. R. G., Zare, H., Rousta, I., Olafsson, H., Verdiguier, E. I., Zhang, H., & Mushore, T. D. (2020). Comparison of Harmonic Analysis of Time Series (HANTS) and Multi-Singular Spectrum Analysis (M-SSA) in Reconstruction of Long-Gap Missing Data in NDVI Time Series. *Remote Sensing 2020, Vol. 12, Page 2747*, *12*(17), 2747. https://doi.org/10.3390/RS12172747

Mandal, D., Kumar, V., Ratha, D., Dey, S., Bhattacharya, A., Lopez-Sanchez, J. M., McNairn, H., & Rao, Y. S. (2020). Dual polarimetric radar vegetation index for crop growth monitoring using sentinel-1 SAR data. *Remote Sensing of Environment*, *247*, 111954. https://doi.org/10.1016/j.rse.2020.111954

Manjunath, K. R., More, R. S., Jain, N. K., Panigrahy, S., & Parihar, J. S. (2015). Mapping of rice-cropping pattern and cultural type using remote-sensing and ancillary data: a case study for South and Southeast Asian countries. *International Journal of Remote Sensing*, *36*(24), 6008–6030. https://doi.org/10.1080/01431161.2015.1110259

Maurer, T. (n.d.). *HOW TO PAN-SHARPEN IMAGES USING THE GRAM-SCHMIDT PAN-SHARPEN METHOD-A RECIPE*.

Maxwell, A. E., Warner, T. A., & Fang, F. (2018). Implementation of machine-learning classification in remote sensing: an applied review. *International Journal of Remote Sensing*, *39*(9), 2784–2817. https://doi.org/10.1080/01431161.2018.1433343

McFeeters, S. K. (1996a). The use of the Normalized Difference Water Index (NDWI) in the delineation of open water features. *International Journal of Remote Sensing*, *17*(7), 1425–1432. https://doi.org/10.1080/01431169608948714

McFeeters, S. K. (1996b). The use of the Normalized Difference Water Index (NDWI) in the delineation of open water features. *International Journal of Remote Sensing*, *17*(7), 1425–1432. https://doi.org/10.1080/01431169608948714

Mira, N. M. C., Catalão Fernandes, J., & Nico, G. (2019). Multitemporal crop classification with machine learning techniques. *PROCEEDINGS OF SPIE*, *October 2019*, 28. https://doi.org/10.1117/12.2532132

Mohsenipour, M., Shahid, S., Chung, E. sung, & Wang, X. jun. (2018). Changing Pattern of Droughts during Cropping Seasons of Bangladesh. *Water Resources Management*, *32*(5), 1555–1568. https://doi.org/10.1007/s11269-017-1890-4

Moreira, A., Prats-Iraola, P., Younis, M., Krieger, G., Hajnsek, I., & Papathanassiou, K. P. (2013). A tutorial on synthetic aperture radar. *IEEE Geoscience and Remote Sensing Magazine*, *1*(1), 6–43. https://doi.org/10.1109/MGRS.2013.2248301

Moser, D., Zechmeister, H. G., Plutzar, C., Sauberer, N., Wrbka, T., & Grabherr, G. (2002). Landscape patch shape complexity as an effective measure for plant species richness in rural landscapes. *Landscape Ecology*, *17*(7), 657–669. https://doi.org/10.1023/A:1021513729205

Motohka, T., Nasahara, K. N., Miyata, A., Mano, M., & Tsuchida, S. (2009). Evaluation of optical satellite remote sensing for rice paddy phenology in monsoon Asia using a continuous in situ dataset. *International Journal of Remote Sensing*, *30*(17), 4343–4357. https://doi.org/10.1080/01431160802549369

Murray, N. J., Keith, D. A., Simpson, D., Wilshire, J. H., & Lucas, R. M. (2018). Remap: An online remote sensing application for land cover classification and monitoring.

Methods in Ecology and Evolution, *9*(9), 2019–2027. https://doi.org/10.1111/2041-210X.13043

Nasim, M., Shahidullah, S., Saha, A., Muttaleb, M., Aditya, T., Ali, M., & Kabir, M. (2018). Distribution of Crops and Cropping Patterns in Bangladesh. *Bangladesh Rice Journal*, *21*(2), 1–55. https://doi.org/10.3329/brj.v21i2.38195

Ni, R., Tian, J., Li, X., Yin, D., Li, J., Gong, H., Zhang, J., Zhu, L., & Wu, D. (2021a). An enhanced pixel-based phenological feature for accurate paddy rice mapping with Sentinel-2 imagery in Google Earth Engine. *ISPRS Journal of Photogrammetry and Remote Sensing*, *178*, 282–296. https://doi.org/10.1016/J.ISPRSJPRS.2021.06.018

Ni, R., Tian, J., Li, X., Yin, D., Li, J., Gong, H., Zhang, J., Zhu, L., & Wu, D. (2021b). An enhanced pixel-based phenological feature for accurate paddy rice mapping with Sentinel-2 imagery in Google Earth Engine. *ISPRS Journal of Photogrammetry and Remote Sensing*, *178*, 282–296. https://doi.org/10.1016/J.ISPRSJPRS.2021.06.018

Noble, W. S. (2006). What is a support vector machine? In *Nature Biotechnology* (Vol. 24, Issue 12, pp. 1565–1567). https://doi.org/10.1038/nbt1206-1565

Onojeghuo, A. O., Blackburn, G. A., Wang, Q., Atkinson, P. M., Kindred, D., & Miao, Y. (2018). Mapping paddy rice fields by applying machine learning algorithms to multi-temporal sentinel-1A and landsat data. *International Journal of Remote Sensing*, *39*(4), 1042–1067. https://doi.org/10.1080/01431161.2017.1395969

Orynbaikyzy, A., Gessner, U., & Conrad, C. (2019). Crop type classification using a combination of optical and radar remote sensing data: a review. In *International Journal of Remote Sensing* (Vol. 40, Issue 17, pp. 6553–6595). Taylor and Francis Ltd. https://doi.org/10.1080/01431161.2019.1569791

Orynbaikyzy, A., Gessner, U., Mack, B., & Conrad, C. (2020). Crop type classification using fusion of sentinel-1 and sentinel-2 data: Assessing the impact of feature selection, optical data availability, and parcel sizes on the accuracies. *Remote Sensing*, *12*(17), 2779. https://doi.org/10.3390/RS12172779

Otsu, N. (2008). A Threshold Selection Method from Gray-Level Histograms. *IEEE Transactions on Systems, Man, and Cybernetics*, *9*(1), 62–66. https://doi.org/10.1109/tsmc.1979.4310076

Ottinger, M., Clauss, K., & Kuenzer, C. (2017). Large-Scale Assessment of Coastal Aquaculture Ponds with Sentinel-1 Time Series Data. *Remote Sensing*, *9*(5), 440. https://doi.org/10/gg36zp

Pal, M. (2005). Random forest classifier for remote sensing classification. *International Journal of Remote Sensing*, *26*(1), 217–222. https://doi.org/10.1080/01431160412331269698

Pekel, J.-F. F., Cottam, A., Gorelick, N., & Belward, A. S. (2016). High-resolution mapping of global surface water and its long-term changes. *Nature*, *540*(7633), 418–422. https://doi.org/10.1038/nature20584

Pohl, C., & van Genderen, J. L. (1998). Multisensor image fusion in remote sensing: Concepts, methods and applications. In *International Journal of Remote Sensing* (Vol. 19, Issue 5, pp. 823–854). https://doi.org/10.1080/014311698215748

Prasad, K., Ottinger, M., Wei, C., & Leinenkugel, P. (2019). Assessment of Coastal Aquaculture for India from Sentinel-1 SAR Time Series. *Remote Sensing*, *11*(3), 357. https://doi.org/10/gg36zq

Qiu, B., Wang, Z., Tang, Z., Chen, C., Fan, Z., & Li, W. (2016). Automated cropping intensity extraction from isolines of wavelet spectra. *Computers and Electronics in Agriculture*, *125*, 1–11. https://doi.org/10.1016/j.compag.2016.04.015

Rahman, M. S., Di, L., Yu, E., Zhang, C., & Mohiuddin, H. (2019). In-season major crop-type identification for us cropland from landsat images using crop-rotation pattern and progressive data classification. *Agriculture (Switzerland)*, *9*(1). https://doi.org/10.3390/agriculture9010017

Rajah, P., Odindi, J., & Mutanga, O. (2018). Feature level image fusion of optical imagery and Synthetic Aperture Radar (SAR) for invasive alien plant species detection and mapping. *Remote Sensing Applications: Society and Environment*, *10*, 198–208. https://doi.org/10.1016/j.rsase.2018.04.007

Ray, D. K., Gerber, J. S., Macdonald, G. K., & West, P. C. (2015). Climate variation explains a third of global crop yield variability. *Nature Communications*, *6*(1), 1–9. https://doi.org/10.1038/ncomms6989

Razu Ahmed, M., Rahaman, K. R., Kok, A., & Hassan, Q. K. (2017). Remote sensing-based quantification of the impact of flash flooding on the rice production: A case study over Northeastern Bangladesh. *Sensors (Switzerland)*, *17*(10). https://doi.org/10.3390/s17102347

Richardson, A. J., & Wiegand, C. L. (1977). Distinguishing Vegetation from Soil Background Information* A gray mapping technique allows delineation of any Landsat scene into vegetative cover stages, degrees of soil brightness, and water. *Photogammetric Engineering and Remote Sensing*, *43*(12), 1541–1552. https://www.asprs.org/wp-content/uploads/pers/1977journal/dec/1977_dec_1541-1552.pdf

Rimal, B., Zhang, L., & Rijal, S. (2018). Crop Cycles and Crop Land Classification in Nepal Using MODIS NDVI. *Remote Sensing in Earth Systems Sciences*, *1*(1–2), 14–28. https://doi.org/10.1007/s41976-018-0002-4

Roerink, G. J., Menenti, M., & Verhoef, W. (2000). Reconstructing cloudfree NDVI composites using Fourier analysis of time series. *International Journal of Remote Sensing*, *21*(9), 1911–1917. https://doi.org/10.1080/014311600209814

Rouse, J., Hass, R. H., Schell, J. A., & Deering, D. W. (1973). Monitoring vegetation systems in the Great Plains with ERTS. *Nasa ERTS Symposium*, 309–313. https://books.google.com/books?hl=en&lr=&id=bn_xAAAAMAAJ&oi=fnd&pg=PA309&dq=Monitoring+vegetation+systems+in+the+Great+Plains+with+ERTS&ots=YTLuNAyTLL&sig=vybwcfIaXo-SE_CWiMjSkeMvZGY

Rubel, O., Lukin, V., Rubel, A., & Egiazarian, K. (2021). Selection of Lee Filter Window Size Based on Despeckling Efficiency Prediction for Sentinel SAR Images. *Remote Sensing 2021, Vol. 13, Page 1887*, *13*(10), 1887. https://doi.org/10.3390/RS13101887

Sakamoto, T., Yokozawa, M., Toritani, H., Shibayama, M., Ishitsuka, N., & Ohno, H. (2005). A crop phenology detection method using time-series MODIS data. *Remote Sensing of Environment*, *96*(3–4), 366–374. https://doi.org/10.1016/j.rse.2005.03.008

Schultz, B., Immitzer, M., Formaggio, A. R., Sanches, I. D. A., Luiz, A. J. B., & Atzberger, C. (2015). Self-guided segmentation and classification of multi-temporal Landsat 8 images for crop type mapping in Southeastern Brazil. *Remote Sensing*, *7*(11), 14482–14508. https://doi.org/10.3390/rs71114482

Shahin, J., Fatema, M. K., Fatema, J., Mondal, M. N., & Rahman, M. M. (2015). Potentialities of pond fish farming in Kaliakair upazila under Gazipur district, Bangladesh. *Research in Agriculture Livestock and Fisheries*, *2*(3), 517–528. https://doi.org/10/ggnshh

She, B., Yang, Y. Y., Zhao, Z. G., Huang, L. S., Liang, D., & Zhang, D. Y. (2020). Identification and mapping of soybean and maize crops based on Sentinel-2 data. *International Journal of Agricultural and Biological Engineering*, *13*(6), 171–182. https://doi.org/10.25165/j.ijabe.20201306.6183

Shelestov, A., Lavreniuk, M., Kussul, N., Novikov, A., & Skakun, S. (2017). Exploring Google earth engine platform for big data processing: Classification of multi-temporal satellite imagery for crop mapping. *Frontiers in Earth Science*, *5*, 1–10. https://doi.org/10.3389/feart.2017.00017

Sheng, Y., Song, C., Wang, J., Lyons, E. A., Knox, B. R., Cox, J. S., & Gao, F. (2016). Representative lake water extent mapping at continental scales using multi-temporal Landsat-8 imagery. *Remote Sensing of Environment*, *185*, 129–141. https://doi.org/10.1016/j.rse.2015.12.041

Sheykhmousa, M., Mahdianpari, M., Ghanbari, H., Mohammadimanesh, F., Ghamisi, P., & Homayouni, S. (2020). Support Vector Machine Versus Random Forest for Remote Sensing Image Classification: A Meta-Analysis and Systematic Review. *IEEE Journal of Selected Topics in Applied Earth Observations and Remote Sensing*, *13*, 6308–6325. https://doi.org/10.1109/JSTARS.2020.3026724

Singha, M., Dong, J., Zhang, G., & Xiao, X. (2019). High resolution paddy rice maps in cloud-prone Bangladesh and Northeast India using Sentinel-1 data. *Scientific Data*, *6*(1), 1–10. https://doi.org/10.1038/s41597-019-0036-3

Sonobe, R., Yamaya, Y., Tani, H., Wang, X., Kobayashi, N., & Mochizuki, K. (2018). Crop classification from Sentinel-2-derived vegetation indices using ensemble learning. *Journal of Applied Remote Sensing*, *12*(02), 1. https://doi.org/10.1117/1.jrs.12.026019

Steinhausen, M. J., Wagner, P. D., Narasimhan, B., & Waske, B. (2018). Combining Sentinel-1 and Sentinel-2 data for improved land use and land cover mapping of monsoon regions. *International Journal of Applied Earth Observation and Geoinformation*, *73*, 595–604. https://doi.org/10/gg37m8

Sun, C., Bian, Y., Zhou, T., & Pan, J. (2019). Using of multi-source and multi-temporal remote sensing data improves crop-type mapping in the subtropical agriculture region. *Sensors (Switzerland)*, *19*(10), 2401. https://doi.org/10.3390/s19102401

Taona Mazarire, T., Eugene Ratshiedana, P., Nyamugama, A., Adam, E., & Chirima, G. (2020). Exploring machine learning algorithms for mapping crop types in a heterogeneous agriculture landscape using Sentinel-2 data. A case study of Free State Province, South Africa. 2. *South African Journal of Geomatics*, *9*(2). https://doi.org/10.4314/sajg.v9i2.22

Tatsumi, K. (2016). Cropping intensity and seasonality parameters across asia extracted by multitemporal SPOT vegetation data. *Journal of Agricultural Meteorology*, *72*(3–4), 142–150. https://doi.org/10.2480/agrmet.D-16-00003

Thenkabail, P. S., Schull, M., & Turral, H. (2005). Ganges and Indus river basin land use/land cover (LULC) and irrigated area mapping using continuous streams of MODIS data. *Remote Sensing of Environment*, *95*(3), 317–341. https://doi.org/10.1016/j.rse.2004.12.018

Thilsted, S. H. (2012). The potential of nutrient-rich small fish species in aquaculture to improve human nutrition and health. *Farming the Waters for People and Food. Proceedings of the Global Conference on Aquaculture 2010*, 57–73.

Tian, H., Huang, N., Niu, Z., Qin, Y., Pei, J., & Wang, J. (2019). Mapping winter crops in China with multi-source satellite imagery and phenology-based algorithm. *Remote Sensing*, *11*(7), 1–23. https://doi.org/10.3390/rs11070820

United Nations. (2018). *The 2030 Agenda and the Sustainable Development Goals An opportunity for Latin America and the Caribbean*. www.cepal.org/en/suscripciones

Valcarce-Diñeiro, R., Arias-Pérez, B., Lopez-Sanchez, J. M., & Sánchez, N. (2019). Multi-temporal dual- and quad-polarimetric synthetic aperture radar data for crop-type mapping. *Remote Sensing*, *11*(13). https://doi.org/10.3390/rs11131518

van der Werff, H. M. A., & van der Meer, F. D. (2008). Shape-based classification of spectrally identical objects. *ISPRS Journal of Photogrammetry and Remote Sensing*, *63*(2), 251–258. https://doi.org/10.1016/j.isprsjprs.2007.09.007

Villa, P., Stroppiana, D., Fontanelli, G., Azar, R., & Brivio, P. A. (2015). In-season mapping of crop type with optical and X-band SAR data: A classification tree approach using synoptic seasonal features. *Remote Sensing*, *7*(10), 12859–12886. https://doi.org/10.3390/rs71012859

Virdis, S. G. P. (2014). An object-based image analysis approach for aquaculture ponds precise mapping and monitoring: a case study of Tam Giang-Cau Hai Lagoon, Vietnam. *Environmental Monitoring and Assessment*, *186*(1), 117–133. https://doi.org/10/f5kcws

Virnodkar, S. S., Pachghare, V. K., Patil, V. C., & Jha, S. K. (2020). Application of Machine Learning on Remote Sensing Data for Sugarcane Crop Classification: A Review. In *Lecture Notes in Networks and Systems* (Vol. 93, pp. 539–555). https://doi.org/10.1007/978-981-15-0630-7_55

Wang, S., Azzari, G., & Lobell, D. B. (2019). Crop type mapping without field-level labels: Random forest transfer and unsupervised clustering techniques. *Remote Sensing of Environment*, *222*, 303–317. https://doi.org/10.1016/j.rse.2018.12.026

Wang, Z., Liu, J., Li, J., & Zhang, D. D. (2018a). Multi-SpectralWater Index (MuWI): A Native 10-m Multi-Spectral Water Index for Accurate Water mapping on sentinel-2. *Remote Sensing*, *10*(10), 1643. https://doi.org/10.3390/rs10101643

Wang, Z., Liu, J., Li, J., & Zhang, D. D. (2018b). Multi-SpectralWater Index (MuWI): A Native 10-m Multi-Spectral Water Index for Accurate Water mapping on sentinel-2. *Remote Sensing*, *10*(10), 1643. https://doi.org/10.3390/rs10101643

Wang, Z., Ziou, D., Armenakis, C., Li, D., & Li, Q. (2005). A comparative analysis of image fusion methods. *IEEE Transactions on Geoscience and Remote Sensing*, *43*(6), 1391–1402. https://doi.org/10.1109/TGRS.2005.846874

Weiss, M., Jacob, F., & Duveiller, G. (2020). Remote sensing for agricultural applications: A meta-review. *Remote Sensing of Environment*, *236*, 111402. https://doi.org/10.1016/j.rse.2019.111402

Whitcraft, A. K., Vermote, E. F., Becker-Reshef, I., & Justice, C. O. (2015). Cloud cover throughout the agricultural growing season: Impacts on passive optical earth observations. *Remote Sensing of Environment*, *156*, 438–447. https://doi.org/10.1016/j.rse.2014.10.009

Wójtowicz, M., Wójtowicz, A., & Piekarczyk, J. (2016). Application of remote sensing methods in agriculture. *Communications in Biometry and Crop Science*, *11*, 31–50.

World Bank. (2018). The Poverty Puzzle Overview. Poverty and Shared Prosperity 2018. In *The World Bank Group*. http://documents.worldbank.org/curated/en/104451542202552048/pdf/132029-REVISED-PUB-PUBLIC.pdf

Xiao, X., Boles, S., Frolking, S., Li, C., Babu, J. Y., Salas, W., & Moore, B. (2006). Mapping paddy rice agriculture in South and Southeast Asia using multi-temporal MODIS images. *Remote Sensing of Environment*, *100*(1), 95–113. https://doi.org/10.1016/J.RSE.2005.10.004

Xiao, X., Boles, S., Liu, J., Zhuang, D., Frolking, S., Li, C., Salas, W., & Moore, B. (2005a). Mapping paddy rice agriculture in southern China using multi-temporal MODIS images. *Remote Sensing of Environment*, *95*(4), 480–492. https://doi.org/10.1016/j.rse.2004.12.009

Xiao, X., Boles, S., Liu, J., Zhuang, D., Frolking, S., Li, C., Salas, W., & Moore, B. (2005b). Mapping paddy rice agriculture in southern China using multi-temporal MODIS images. *Remote Sensing of Environment*, *95*(4), 480–492. https://doi.org/10.1016/j.rse.2004.12.009

Xiao, X., Lu, Y., Huang, X., & Chen, T. (2021). Temporal Series Crop Classification Study in Rural China Based on Sentinel-1 SAR Data. *IEEE Journal of Selected Topics in Applied Earth Observations and Remote Sensing*, *14*, 2769–2780. https://doi.org/10.1109/JSTARS.2021.3057903

Xing, H., Hou, D., Wang, S., Yu, M., & Meng, F. (2021). O-LCMapping: a Google Earth Engine-based web toolkit for supporting online land cover classification. *Earth Science Informatics*, *14*(1), 529–541. https://doi.org/10.1007/s12145-020-00562-6

Xu, H. (2006a). Modification of normalised difference water index (NDWI) to enhance open water features in remotely sensed imagery. *International Journal of Remote Sensing*, *27*(14), 3025–3033. https://doi.org/10.1080/01431160600589179

Xu, H. (2006b). Modification of normalised difference water index (NDWI) to enhance open water features in remotely sensed imagery. *International Journal of Remote Sensing*, *27*(14), 3025–3033. https://doi.org/10.1080/01431160600589179

Yalew, S. G., van Griensven, A., & van der Zaag, P. (2016). AgriSuit: A web-based GIS-MCDA framework for agricultural land suitability assessment. *Computers and Electronics in Agriculture*, *128*, 1–8. https://doi.org/10.1016/j.compag.2016.08.008

Yang, J., Ren, G., Ma, Y., & Fan, Y. (2016). Coastal wetland classification based on high resolution SAR and optical image fusion. *International Geoscience and Remote Sensing Symposium (IGARSS)*, *2016-Novem*, 886–889. https://doi.org/10.1109/IGARSS.2016.7729224

Yang, X., Qin, Q., Grussenmeyer, P., & Koehl, M. (2018). Urban surface water body detection with suppressed built-up noise based on water indices from Sentinel-2 MSI imagery. *Remote Sensing of Environment*, *219*, 259–270. https://doi.org/10.1016/j.rse.2018.09.016

Yin, D., Cao, X., Chen, X., Shao, Y., & Chen, J. (2013). Comparison of automatic thresholding methods for snow-cover mapping using Landsat TM imagery. *International Journal of Remote Sensing*, *34*(19), 6529–6538. https://doi.org/10.1080/01431161.2013.803631

Yommy, A. S., Liu, R., & Wu, A. S. (2015). SAR image despeckling using refined lee filter. *Proceedings - 2015 7th International Conference on Intelligent Human-Machine Systems and Cybernetics, IHMSC 2015*, *2*, 260–265. https://doi.org/10.1109/IHMSC.2015.236

Yu, J., & Wu, J. (2018). The Sustainability of Agricultural Development in China: The Agriculture–Environment Nexus. *Sustainability 2018, Vol. 10, Page 1776*, *10*(6), 1776. https://doi.org/10.3390/SU10061776

Yu, Q., Gong, P., Clinton, N., Biging, G., Kelly, M., & Schirokauer, D. (2006). Object-based detailed vegetation classification with airborne high spatial resolution remote sensing imagery. *Photogrammetric Engineering & Remote Sensing*, *72*(7), 799–811. https://doi.org/10/gdnfwp

Yu, Z., Di, L., Rahman, Md. S., Tang, J., R, S., & Tang, J. (2020). Fishpond Mapping by Spectral and Spatial-Based Filtering on Google Earth Engine: A Case Study in Singra Upazila of Bangladesh. *Remote Sensing*. https://doi.org/10.3390/rs12172692

Yu, Z., Di, L., Tang, J., Zhang, C., Lin, L., Yu, E. G., Rahman, M. S., Gaigalas, J., & Sun, Z. (2018). Land use and land cover classification for Bangladesh 2005 on google earth engine. *2018 7th International Conference on Agro-Geoinformatics, Agro-Geoinformatics 2018*, 2–6. https://doi.org/10.1109/Agro-Geoinformatics.2018.8475976

Yu, Z., Wang, W., Li, C., Liu, W., & Yang, J. (2018). Speckle Noise Suppression in SAR Images Using a Three-Step Algorithm. *Sensors (Basel, Switzerland)*, *18*(11). https://doi.org/10.3390/S18113643

Zeng, Y., Zhang, Y. X., & van Genderen, J. L. (2006). Comparison and Analysis of Remote Sensing Data Fusion Techniques. *Proceedings of the ISPRS Commission VII Symposium 'Remote Sensing: From Pixels to Processes*, *36*, 5. http://www.isprs.org/proceedings/XXXVI/part7/PDF/014.pdf

Zeyada, H. H., Ezz, M. M., Nasr, A. H., Shokr, M., & Harb, H. M. (2016). Evaluation of the discrimination capability of full polarimetric SAR data for crop classification. *International Journal of Remote Sensing*, *37*(11), 2585–2603. https://doi.org/10.1080/01431161.2016.1182663

Zhang, C., Di, L., Hao, P., Yang, Z., Lin, L., Zhao, H., & Guo, L. (2021). Rapid in-season mapping of corn and soybeans using machine-learned trusted pixels from Cropland Data Layer. *International Journal of Applied Earth Observation and Geoinformation*, *102*, 102374. https://doi.org/10.1016/j.jag.2021.102374

Zhang, C., Di, L., Yang, Z., Lin, L., & Hao, P. (2020). AgKit4EE: A toolkit for agricultural land use modeling of the conterminous United States based on Google Earth Engine. *Environmental Modelling and Software*, *129*, 104694. https://doi.org/10.1016/j.envsoft.2020.104694

Zhang, F., Li, J., Zhang, B., Shen, Q., Ye, H., Wang, S., & Lu, Z. (2018). A simple automated dynamic threshold extraction method for the classification of large water bodies from landsat-8 OLI water index images. *International Journal of Remote Sensing*, *39*(11), 3429–3451. https://doi.org/10/ggnshj

Zhang, G., Zheng, G., Gao, Y., Xiang, Y., Lei, Y., & Li, J. (2017). Automated water classification in the Tibetan plateau using Chinese GF-1 WFV data. *Photogrammetric Engineering & Remote Sensing*, *83*(7), 509–519. https://doi.org/10/gbz4tp

Zhang, H., Kang, J., Xu, X., & Zhang, L. (2020a). Accessing the temporal and spectral features in crop type mapping using multi-temporal Sentinel-2 imagery: A case study of Yi'an County, Heilongjiang province, China. *Computers and Electronics in Agriculture*, *176*, 105618. https://doi.org/10.1016/j.compag.2020.105618

Zhang, H., Kang, J., Xu, X., & Zhang, L. (2020b). Accessing the temporal and spectral features in crop type mapping using multi-temporal Sentinel-2 imagery: A case study of Yi'an County, Heilongjiang province, China. *Computers and Electronics in Agriculture*, *176*, 105618. https://doi.org/10.1016/j.compag.2020.105618

Zhang, M., Wu, B., Zeng, H., He, G., Liu, C., Tao, S., Zhang, Q., Nabil, M., Tian, F., Bofana, J., Beyene, A. N., Elnashar, A., Yan, N., Wang, Z., & Liu, Y. (2021). GCI30: A global dataset of 30m cropping intensity using multisource remote sensing imagery. *Earth System Science Data*, *13*(10), 4799–4817. https://doi.org/10.5194/essd-13-4799-2021

Zhang, R. H., Rao, N. X., & Liao, K. N. (1996). Approach for a vegetation index resistant to atmospheric effect. *Acta Botanica Sinica*, *38*(1), 53–62. http://www.jipb.net/EN/abstract/abstract23925.shtml

Zhang, W., & Yu, L. (2010). SAR and Landsat ETM+ image fusion using variational model. *CCTAE 2010 - 2010 International Conference on Computer and Communication Technologies in Agriculture Engineering*, *3*, 205–207. https://doi.org/10.1109/CCTAE.2010.5544210

Zhou, J., Jia, L., Hu, G., & Menenti, M. (2012). Evaluation of Harmonic Analysis of Time Series (HANTS): Impact of gaps on time series reconstruction. *Proceedings of the 2nd International Workshop on Earth Observation and Remote Sensing Applications, EORSA 2012*, 31–35. https://doi.org/10.1109/EORSA.2012.6261129

Zhou, J., Jia, L., & Menenti, M. (2015). Reconstruction of global MODIS NDVI time series: Performance of Harmonic ANalysis of Time Series (HANTS). *Remote Sensing of Environment*, *163*, 217–228. https://doi.org/10.1016/j.rse.2015.03.018

Zhou, Y., Dong, J., Xiao, X., Xiao, T., Yang, Z., Zhao, G., Zou, Z., & Qin, Y. (2017a). Open surface water mapping algorithms: A comparison of water-related spectral indices and sensors. *Water (Switzerland)*, *9*(4), 256. https://doi.org/10.3390/w9040256

Zhou, Y., Dong, J., Xiao, X., Xiao, T., Yang, Z., Zhao, G., Zou, Z., & Qin, Y. (2017b). Open surface water mapping algorithms: A comparison of water-related spectral indices and sensors. *Water (Switzerland)*, *9*(4), 256. https://doi.org/10.3390/w9040256

Zhou, Z., Huang, J., Wang, J., Zhang, K., Kuang, Z., Zhong, S., & Song, X. (2015). Object-oriented classification of sugarcane using time-series middle-resolution remote sensing data based on AdaBoost. *PLoS ONE*, *10*(11). https://doi.org/10.1371/journal.pone.0142069

BIOGRAPHY

Zhiqi Yu graduated from Wuhan University with a Bachelor of Engineering degree in Remote Sensing Science and Technology in 2015. In August 2017, he received his Master of Art degree in Geography from The Ohio State University, Columbus, Ohio. Later, he came to George Mason University to pursue his Ph.D. in Earth Systems and Geoinformation Sciences in 2017.